University of Windsor
Scholarship at UWindsor

Electronic Theses and Dissertations | Theses, Dissertations, and Major Papers

10-19-2015

Exhaust Pressure Waves in Diesel Engines and the Impacts on Aftertreatment Sprays

Zhenyi Yang
University of Windsor

Follow this and additional works at: https://scholar.uwindsor.ca/etd

Recommended Citation

Yang, Zhenyi, "Exhaust Pressure Waves in Diesel Engines and the Impacts on Aftertreatment Sprays" (2015). *Electronic Theses and Dissertations*. 5481.
https://scholar.uwindsor.ca/etd/5481

This online database contains the full-text of PhD dissertations and Masters' theses of University of Windsor students from 1954 forward. These documents are made available for personal study and research purposes only, in accordance with the Canadian Copyright Act and the Creative Commons license—CC BY-NC-ND (Attribution, Non-Commercial, No Derivative Works). Under this license, works must always be attributed to the copyright holder (original author), cannot be used for any commercial purposes, and may not be altered. Any other use would require the permission of the copyright holder. Students may inquire about withdrawing their dissertation and/or thesis from this database. For additional inquiries, please contact the repository administrator via email (scholarship@uwindsor.ca) or by telephone at 519-253-3000ext. 3208.

Exhaust Pressure Waves in Diesel Engines and the Impacts on Aftertreatment Sprays

By

Zhenyi Yang

A Thesis
Submitted to the Faculty of Graduate Studies
through the Department of Mechanical, Automotive and Materials Engineering
in Partial Fulfillment of the Requirements for
the Degree of Masters of Applied Science at the
University of Windsor

Windsor, Ontario, Canada

2015

© 2015 Zhenyi Yang

Exhaust Pressure Waves in Diesel Engines and the Impacts on Aftertreatment Sprays

By

Zhenyi Yang

APPROVED BY:

_____

Dr. Paul Henshaw, Outside Reader
Department of Civil and Environmental Engineering

_____

Dr. Gary Rankin, Program Reader
Department of Mechanical, Automotive and Materials Engineering

_____

Dr. Ming Zheng, Advisor
Department of Mechanical, Automotive and Materials Engineering

_____

Dr. David S-K Ting, Advisor
Department of Mechanical, Automotive and Materials Engineering

15 September 2015

DECLARATION OF ORIGINALITY

I hereby certify that I am the sole author of this thesis and that no part of this thesis has been published or submitted for publication.

I certify that, to the best of my knowledge, my thesis does not infringe upon anyone's copyright nor violate any proprietary rights and that any ideas, techniques, quotations, or any other material from the work of other people included in my thesis, published or otherwise, are fully acknowledged in accordance with the standard referencing practices. Furthermore, to the extent that I have included copyrighted material that surpasses the bounds of fair dealing within the meaning of the Canada Copyright Act, I certify that I have obtained a written permission from the copyright owner(s) to include such material(s) in my thesis and have included copies of such copyright clearances to my appendix.

I declare that this is a true copy of my thesis, including any final revisions, as approved by my thesis committee and the Graduate Studies office, and that this thesis has not been submitted for a higher degree to any other University or Institution.

ABSTRACT

Aftertreatment devices are commonly used in diesel engine systems for emission control. To ensure the proper function of the aftertreatment devices, it is often necessary to inject additional fuel or a reducing agent into the exhaust flow. The conditions in the exhaust flow are affected by the exhaust pressure wave, caused by the reciprocating movement of the piston and valves. Therefore, this research investigates the factors that affect the exhaust pressure wave and the consequent impacts of this wave on a liquid spray.

First, the exhaust pressure wave action was studied experimentally on a single cylinder diesel engine at various engine operating conditions such as different load, EGR, and exhaust backpressure levels. Then, the gas flow velocity in the exhaust system was estimated with the simulation tool AVL BOOST.

A stand-alone shock tube was used to create a condition comparable to the exhaust flow. The impacts of the pressure wave and the gas flow on the aftertreatment spray distribution and the droplet breakup were studied via optical methods.

DEDICATION

This thesis is dedicated to my family: my father, my mother, my sister and my husband.

ACKNOWLEDGEMENTS

I want to express my sincere gratitude to my supervisors – Dr. Ming Zheng and Dr. David S-K. Ting without whom I would not have got the opportunity to join this wonderful research group. Their guidance and support have been a consistent encouragement for this thesis work. I would also like to thank them for all the other help they have provided in my academic life and beyond.

I am deeply grateful to my committee members – Dr. Gary Rankin and Dr. Paul Henshaw for their invaluable assistance and feedback.

I wish to extend my acknowledgement to everyone in the Clean Diesel Engine research group and the Turbulence Energy research group at the University of Windsor. I want to thank all my colleagues – Dr. Meiping Wang, Dr. Shui Yu, Dr. Tadanori Yanai, Dr. Xiaoye Han, Dr. Xiao Yu, Marko Jeftic, Prasad Divekar, Kelvin Xie, Tongyang Gao, Shouvik Dev, Qingyuan Tan, Geraint Bryden, Mark Ives and Christopher Aversa for their support in my research and every other aspect of my life. I am very grateful to Dr. Shui Yu, Dr. Xiaoye Han and Marko Jeftic for the many enlightening discussions during the course of this research. I would like to thank Shouvik Dev and Kelvin Xie for all the effort and time they put in for the shock tube experiments. I also want to express my gratitude to Prasad Divekar and Qingyuan Tan for their support in designing the control program. Tongyang Gao, Geraint Bryden, Mark Ives, and Christopher Aversa helped a lot in preparing the experimental set up, and I would like to acknowledge their contribution.

My sincere thanks to Mr. Bruce Durfy, who helped me build the shock tube, and who gave me valuable assistance on the fabrication of various hardware components used in this research.

I am thankful for the support from the University of Windsor, AUTO21, Canada Research Chair Program, Canada Foundation of Innovation (CFI), BioFuelNet, Natural Sciences and Engineering Research Council of Canada (NSERC), Ford Motor Company, Canada and other automotive OEMs. I am grateful to AVL LIST GmbH for the use of the AVL BOOST simulation software.

Last but not the least, I want to thank my family for their continuous love and support.

TABLE OF CONTENTS

LIST OF TABLES

LIST OF FIGURES

LIST OF SYMBOLS AND ABBREVIATIONS

Symbols

α	crank angle	[°CA]
ζ	friction loss coefficient	[-]
σ	surface tension	[N/m]
μ	dynamic viscosity	[Pa·s]
$\mu\sigma$	flow coefficient of the port	[-]
ρ	density	[kg·m^{-3}]
$\delta\rho$	small perturbation of density	[kg·m^{-3}]
a	speed of sound	[m·s^{-1}]
c_v	constant volume specific heat capacity	[J·K^{-1}]
d	diameter	[m]
e	energy	[J]
F_R	friction term	[J]
h	enthalpy	[J]
k	ratio of specific heats	[-]
m	mass	[kg]
Ma	Mach number	[-]
Oh	Ohnesorge number	[-]
p	pressure	[Pa], [bar]
δp	small perturbation of pressure	[Pa]
Q	heat	[J]
R_o	gas constant	[J·kg^{-1}·K^{-1}]
A	area	[m^2]
t	time	[s]
T	temperature	[K], [°C]
u	velocity	[m·s^{-1}]
δu	small perturbation of velocity	[m·s^{-1}]
U	specific internal energy	[J]
U_p	shock wave gas flow velocity	[m·s^{-1}]

V	volume	[m^3]
W	shock wave speed	[$m \cdot s^{-1}$]
We	Weber number	[-]
x	distance	[m]

Subscript

BB	blow by
c	in-cylinder condition
c_EVO	in-cylinder condition at the time when the exhaust valves open
e	exhaust condition
e_max	maximum exhaust condition
eff	effective
eq	equilibrium state
ev	evaporation
F	fuel
g	gas
i	inflow
l	liquid
$o1$	upstream stagnation condition
$o2$	downstream static condition
out	outflow
pl	condition in plenum
r	relative
$reac$	reaction
vi	valve inner condition
w	wall

Abbreviations

BDC	Bottom dead center
CA50	Crank angle of 50% heat release
CI	Compression ignition
CO	Carbon monoxide
DOC	Diesel oxidation catalyst
DPF	Diesel particulate filter
DSLR	Digital single lens reflex
EGR	Exhaust gas recirculation
ENO	Essentially non-oscillatory
EPA	Environmental Protection Agency
EVC	Exhaust valve close
EVO	Exhaust valve open
FPGA	Field-programmable gate array
fps	Frames per second
FSO	Full scale output
HC	Hydrocarbons
HCCI	Homogeneous charge compression ignition
IMEP	Indicated mean effective pressure
IVC	Intake valve close
IVO	Intake valve open
LED	Light emitting diode
LNT	Lean NOx trap
N_2	Nitrogen
NOx	Nitrogen oxides
PM	Particulate matter
RT	Real time
SCR	Selective catalytic reduction
TDC	Top dead center

CHAPTER 1 INTRODUCTION

1.1 Research background

Diesel engines have traditionally had the advantages of better fuel efficiency and high load capability compared to gasoline engines. They are used in a variety of on-road applications from small cars to large trucks. However, one of the most critical challenges facing modern diesel engines is the stringent emission standard [1]. The regulated emissions include carbon monoxide (CO), unburned hydrocarbons (HC), nitrogen oxides (NOx), as well as particulate matter (PM). Unlike gasoline engines that mostly operate at near stoichiometric conditions, diesel engines usually operate at lean conditions with excess oxygen. The latter mode is beneficial for oxidation of HC and CO in an exhaust aftertreatment system; however the control of NOx emissions is extremely difficult [2]. The three-way catalyst which can effectively reduce all the above major pollutants in gasoline engines is not applicable at lean conditions because the presence of oxygen prevents the reduction of NOx. Also, in diesel engines, the fuel is usually injected into the combustion chamber at the end of the compression stroke, and there is a limited time for the fuel to mix with the air. The predominantly diffusion type of combustion in a diesel engine makes PM control a major concern.

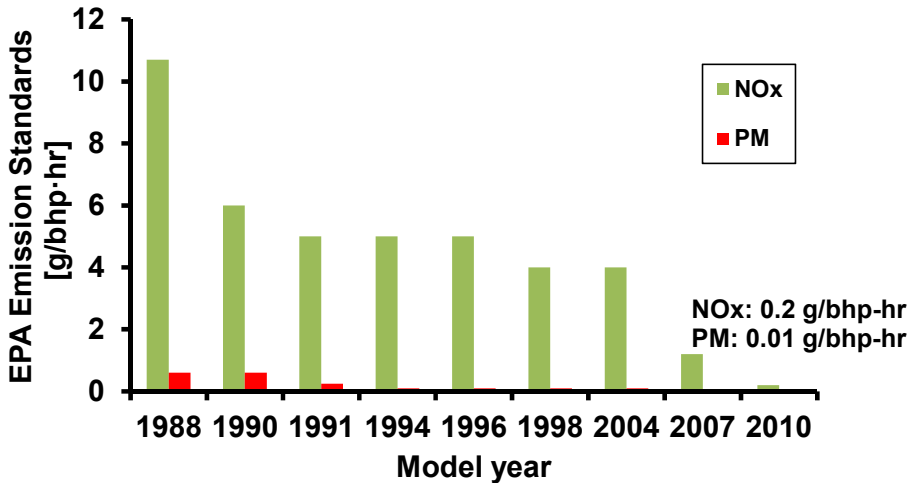

Figure 1-1. US EPA & California emission standards for heavy-duty CI engines [1]

Though it is difficult to deal with these emissions, the emission regulations have progressively become more stringent over the years. For instance, the US Environmental Protection Agency (EPA) standard value for NOx and PM emissions for heavy duty

compression ignition (CI) engines has tightened by more than 95% in the past twenty years (Figure 1-1). Tremendous effort has been put into achieving these targets by using sophisticated emission control technologies. Generally, these technologies can be classified into two categories: in-cylinder and aftertreatment.

The in-cylinder emission control strategies aim to reduce the production of emissions inside the cylinder. It is usually realized by proper management of the air and fuel supply. Many of the in-cylinder techniques are used jointly to get the optimum results. For instance, in order to reduce the generation of PM, a higher fuel injection pressure can be used to improve the mixing of the fuel with the air. The fuel rich pockets where the PM emissions are most likely to form can be reduced with the better mixing. Meanwhile an elevated boost pressure is preferred to enhance the oxidization of PM emissions. For NOx reduction, as NOx emissions are generated by oxidization of nitrogen (N_2) under high temperature conditions, the in-cylinder NOx control strategies are focused on either lowering the combustion temperature or reducing the background oxygen concentration. A practical technique of exhaust gas recirculation (EGR) has been deployed as a promising method in NOx reduction [3]. By recirculating a portion of the exhaust gas into the cylinder, the in-cylinder oxygen concentration is reduced. Meanwhile, the heat capacity of the in-cylinder charge is increased by the recirculated exhaust gas so that the in-cylinder temperature is reduced. Both of these are beneficial for NOx suppression. However, the depletion of oxygen by EGR often causes a significant increase of PM, especially during high load operations. In order to alleviate this trade-off effect, other techniques are often adopted concurrently with EGR, such as the fuel injection adjustment, boost pressure control, and so forth. It is hard to find a single in-cylinder technology that can effectively reduce all the emissions simultaneously. The effective in-cylinder control strategies rely on the elaborate collaboration of all these systems. The control strategies should be flexible enough to accommodate different engine running conditions as well.

Alternatively, various after-treatment devices can be adopted to deal with emissions. Some sample layout configurations of aftertreatment systems are shown in Figure 1-2.

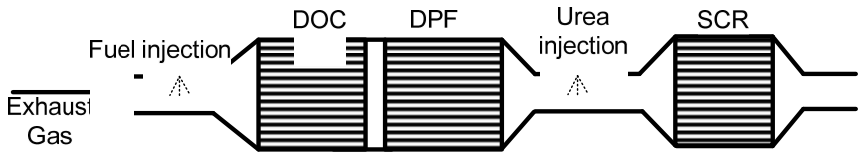

(a) DOC, DPF and SCR

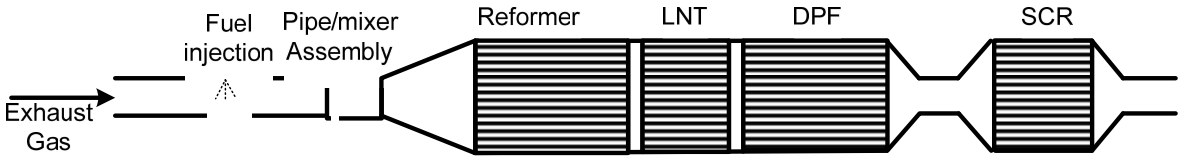

(b) Reformer, LNT, DPF and SCR

Figure 1-2. Aftertreatment system layout (adapted from [4,5])

The advantages of aftertreatment techniques are that they can be applied to existing engines and there are fewer restrains imposed on the in-cylinder combustion process. Exhaust aftertreatment is now a very important part of automotive emission control.

The exhaust aftertreatment systems of diesel engines are typically composed of different catalytic converters. These converters usually have a honeycomb like structure. The base form is called the substrate and is shown in Figure 1-3. There are numerous small channels in the substrate which can provide a large surface area for the chemical reactions. A wash coat layer is added onto the walls of the substrate channels and the catalysts are supported by the wash coat layer. The catalysts are commonly precious metals such as platinum or palladium [6,7]. With the presence of the catalysts, the activation energy of chemical reactions is reduced so that the desired reaction is dominant and the conversion efficiency is improved.

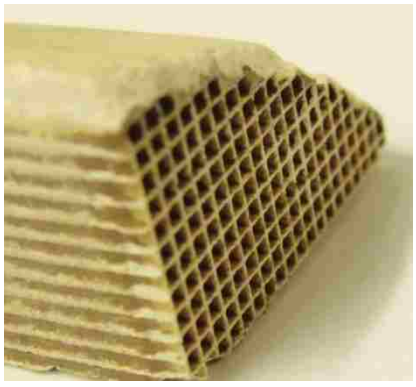

Figure 1-3. Ceramic aftertreatment substrate

Catalytic converters in diesel engines can be classified into two categories – oxidation catalysts and reduction catalysts. Oxidation catalysts such as the diesel oxidation catalyst (DOC) and diesel particulate filter (DPF) function by oxidation of the HC and PM respectively. As there is usually sufficient oxygen left in the exhaust gas, the reaction is straight forward as long as the temperature is above an appropriate threshold and the resident time for reaction is sufficient. Reduction catalysts, on the other hand, require a reducing agent to be supplied in order to operate at lean conditions, because most of the potential reducing agents (CO and HC) would likely be consumed by the oxygen prior to serving as the reducing agents. Reduction catalysts such as the lean NOx trap (LNT) and the selective catalytic reduction (SCR) are often used in diesel engine aftertreatment systems to reduce NOx emissions [4,8–10]. The DPF, LNT, and SCR systems usually require an injection of a liquid agent such as diesel or urea solution in order to function properly. Since this research focuses on the effect of the exhaust pressure wave on such an injection, these three systems have been described in detail in the following sub-sections.

1.1.1 Diesel particulate filter (DPF)

A diesel particulate filter (Figure 1-4) is used to remove the PM emissions. By blocking one end of the substrate channels, the exhaust flow is forced to flow through the channel walls. In this way, only gas can flow through and solid particles are trapped.

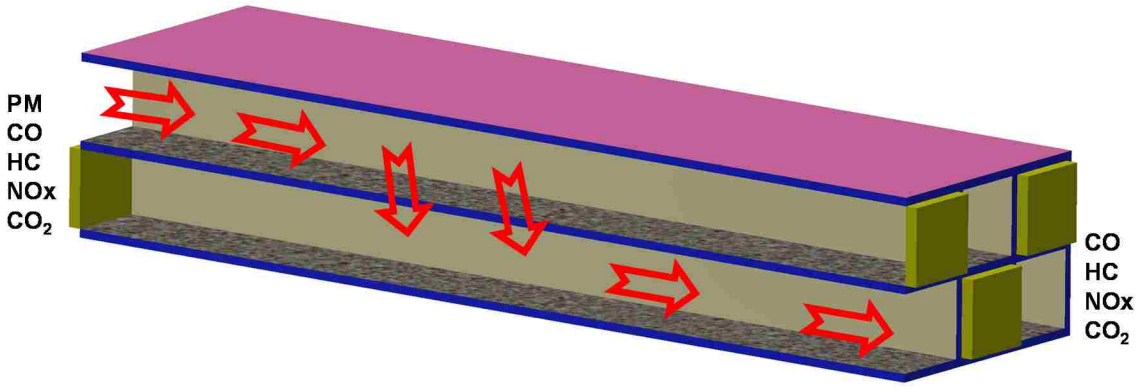

Figure 1-4. Diesel particulate filter (adapted from [11])

The efficiency of DPF can be more than 95%. However, eventually the backpressure in the exhaust system can increase considerably when more particles are accumulated on the channel walls. In order to reduce the backpressure, the DPF should be periodically

cleaned up through the so called “regeneration” mode. The regeneration mode can be activated by increasing the exhaust temperature. For the lean burn conditions in a diesel engine, the exhaust temperature during low or medium load conditions may not be high enough to burn the trapped particles. To increase the exhaust temperature, the usual approach is to add more fuel into the exhaust gas to create a richer condition which can burn and produce heat. The fuel can be added by either in-cylinder as post injection or by injecting fuel into the exhaust system as shown in Figure 1-2. For post injection, the thermal loss along the exhaust pipe is significant. This may increase the fuel penalty because more fuel has to be added in order to reach the desired temperature.

1.1.2 Selective catalytic reduction (SCR)

The selective catalytic reduction (SCR) has been reported to be very effective in reducing NOx emissions [8]. A urea water solution is usually applied as a reducing agent. The urea solution is injected into the exhaust gas stream some distance upstream of the converter. The water content evaporates in the hot exhaust gas, leaving pure urea dispersed effectively. The pure urea is heated up and decomposed to generate isocyanic acid (HNCO) and ammonia (NH_3). Through hydrolysis, isocyanic acid further reacts with water vapor to produce more ammonia. Ammonia acts as a reducing agent and converts NOx into N_2. The main SCR reactions are as follows [12]:

$$NH_2\text{–}CO\text{–}NH_2(\text{aqueous}) \rightarrow NH_2\text{–}CO\text{–}NH_2(\text{solid}) + H_2O(\text{gas}) \quad (1)$$

$$NH_2\text{–}CO\text{–}NH_2(\text{solid}) \xrightarrow{catalyst} NH_3(\text{gas}) + HNCO(\text{gas}) \quad (2)$$

$$HNCO(\text{gas}) + H_2O(\text{gas}) \rightarrow NH_3(\text{gas}) + CO_2(\text{gas}) \quad (3)$$

$$4NH_3 + 4NO + O_2 \xrightarrow{catalyst} 4N_2 + 6H_2O \quad (4)$$

$$4NH_3 + 3NO_2 \xrightarrow{catalyst} 7/2N_2 + 6H_2O \quad (5)$$

$$2NH_3 + NO + NO_2 \xrightarrow{catalyst} 2N_2 + 3H_2O \quad (6)$$

1.1.3 Lean NOx trap (LNT)

The lean NOx trap (LNT) catalyst is another system to reduce NOx emissions. Its operation varies according to the exhaust gas condition. During diesel fuel lean conditions, NO is oxidized to NO_2 and NO_2 is absorbed by reacting with an alkaline oxide such as BaO to generate $Ba(NO_3)_2$. The reactions are shown in (7) and (8) [9].

$$2NO + O_2 \xrightarrow{catalyst} 2NO_2 \quad (7)$$

$$3NO_2 + BaO \rightarrow Ba(NO_3)_2 + NO \quad (8)$$

As more NO_2 molecules are trapped, the available BaO sites reduce and the storage efficiency declines. Then, the regeneration mode is activated by providing a fuel-rich exhaust stream to release the nitrates from the storage sites and convert them into N_2. Taking propane (C_3H_6) as an example fuel, the main reactions in the process are shown in (9)-(12) [9]. The fuel for the reaction can either be provided by in-cylinder post injection or by injecting fuel directly into the exhaust stream.

$$C_3H_6 + 3H_2O \rightarrow 3CO + 6H_2 \quad (9)$$

$$9Ba(NO_3)_2 + 5C_3H_6 \rightarrow 9N_2 + 15CO_2 + 15H_2O + 9BaO \quad (10)$$

$$Ba(NO_3)_2 + 5CO \rightarrow N_2 + 5CO_2 + BaO \quad (11)$$

$$Ba(NO_3)_2 + 5H_2 \rightarrow N_2 + 5H_2O + BaO \quad (12)$$

1.2 Aftertreatment injection

In both SCR and LNT converters, the reducing agent has to be added to react with NOx in the exhaust gas. The reducing agent can be either urea solution in SCR or fuel in LNT. For LNT, the fuel can be injected through the in-cylinder post injection or from the direct injection into the exhaust gas. For SCR, presently the aftertreatment injection is a common practical option. Sometimes, in order to increase the exhaust temperature for DPF regeneration, diesel fuel can also be added through the aftertreatment injection.

The advantage of aftertreatment injection is that the in-cylinder process is marginally affected. The heat loss due to the long transportation path when the in-cylinder injection is used can be avoided as well. Moreover, as the fuel or reducing agent is directly injected into the exhaust gas stream, it is easier to control the time and the quantity of injection to promote the performance of the aftertreatment system. To better understand and thus control the aftertreatment injection effectively, significant research has already been performed [13–18].

In the case of aftertreatment injection, the droplet size and spray distribution in the exhaust gas stream are critical. Uniformly distributed plumes with fine droplets are beneficial for efficient mixing and reaction. Improved uniformity can ensure that most of the substrate channels are utilized, while small droplets can promote the evaporation and further help the mixing process. Oh et al. investigated the effect of urea spray distribution

on NOx reduction [17]. Their results showed that the improved urea spray uniformity and atomization led to a higher NOx reduction efficiency in the SCR convertors.

The aftertreatment injectors are often mounted quite close to the catalytic converters. A short path can reduce the transportation loss of the injected fluid (e.g., deposit of urea onto the exhaust pipe wall). However, there is a limited time available for the vaporization and mixing of the droplets with the exhaust gas. Mounting the injectors further away can extend the time of evaporation and mixing, but that is often not possible because of the space constraints on a vehicle.

Since better atomization can be helpful in improving the effectiveness of an aftertreatment system, one direct way of enhancing atomization is by increasing the injection pressure whilst using smaller nozzle holes. The injection pressures of current aftertreatment injection systems are usually low (less than 10 bar) [17–21]. Though there are some high pressure injection systems [22], the incremental cost is substantial. For injection at such a low pressure, the atomization of the spray is usually not optimum. A mixer device is used under some conditions to improve the evaporation and mixing [17,23,24]. Also, there are different injection methods including both airless [19,20], and air assisted [21] injection for various applications.

Research on exhaust injection systems showed that the distribution and atomization of the spray were not only related to the injection pressure and temperature of the liquid, but also affected by the background conditions – the pressure, temperature and velocity of the exhaust gas [13,25]. However, for most of the published research, the exhaust flow stream was assumed to be uniform [13,17,18,22,25], which is hard to achieve in a practical engine exhaust system, especially for the dosing liquid concentration.

The operating conditions in an engine exhaust system are quite complicated with not only a wide range of temperature variations, but also a continuous change of pressure and gas flow. The flow conditions in the intake and exhaust pipes are highly pulsating because of the intermittent nature of internal combustion. The following section describes the research on the pressure wave actions in an engine system.

1.3 Pressure waves in engine intake and exhaust systems

Pressure wave actions are generated by the piston and valve motions as shown in Figure 1-5. When an exhaust valve opens, the in-cylinder pressure is much higher than the

pressure in the exhaust pipe, so that a compression wave is generated in the immediate downstream of the valve flow from this pressure difference.

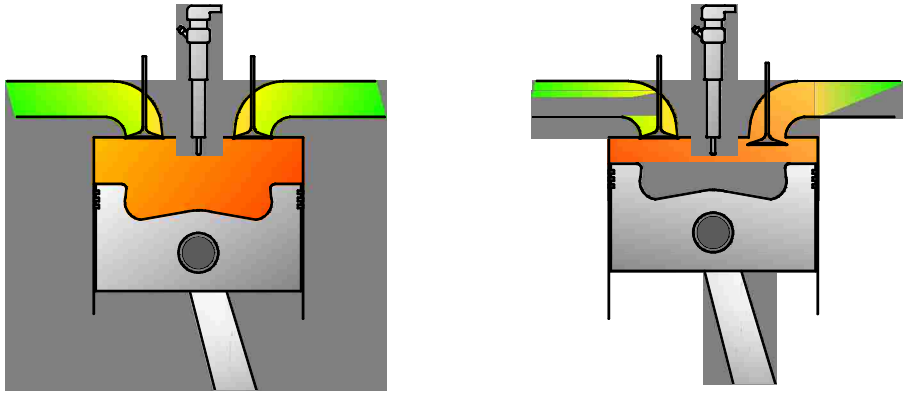

Figure 1-5. Formation of exhaust pressure wave

Pressure waves have been studied extensively for their significant effects on the engine performance by previous researchers [26-51]. Pressure waves in the intake and exhaust manifolds influence the filling and emptying processes of the cylinder charge, and thus impact the engine volumetric efficiency, especially for naturally aspirated engines. Research results on intake pressure waves are often used for tuning the manifolds to improve the volumetric efficiency. As the application of turbochargers becomes more popular, this effect may not be as obvious. The exhaust manifold is traditionally designed in a way that the exhaust gas can be expelled quickly during the exhaust valve open period, so that more fresh air can flow into the cylinder. Alternatively, the exhaust pressure wave can also be used to introduce internal EGR by restricting the exhaust flow when the exhaust valves are open. Another aspect regarding pressure waves is the noise level control in the engine system through the muffler or silencer design [26–29].

Publications on pressure wave actions in the engine intake and exhaust systems include both experimental and simulation results [30–32]. The experimental method is straight forward, usually by measuring the pressure in the intake or exhaust pipes at various engine operating conditions. For the simulation approach, many researchers have worked on model development [31,33–42]. Most of the simulation methods of pressure wave actions use the one dimensional (1-D) approximation. Since the pressure wave action in the gas flow system of an engine has a strong one dimensional character, primarily changing along the axial direction of the pipe, the differences in cross-sectional area have

a minor effect, and it is reasonable to use 1-D approximation. Based on the applicable assumptions, the 1-D simulation methods can be classified into three major categories – non-linear gas dynamic methods, linear acoustic methods, and hybrid methods. The hybrid method is the combination of the previous two. One of the well-known simulation methods is known as the method of characteristics introduced by Benson et al. [33]. Though this method only has a first order precision, it is widely regarded as one of the classical methods, and many of the boundary conditions from their work are used in a number of simulation codes [43]. With the development of the simulation ability, and faster computing, methods with higher precision have been used as well such as finite difference schemes and total variation diminishing methods [29,43–45].

1.3.1 Non-linear gas dynamic method

The non-linear gas dynamic model is applied by directly solving the governing equations, including the continuity equation, the momentum equation, and the energy equation. The one dimensional equations shown here are based on the assumptions that the variables change only along the pipe length while they are constant over the same cross sectional area. Moreover, the viscous effects are assumed to be minor. The one dimension governing equations can be written as [32]:

$$\frac{\partial \varphi}{\partial t} + \frac{\partial F(\varphi)}{\partial x} = B \tag{1-1}$$

Where the vectors φ, F, and B are defined by:

$$\varphi = \begin{bmatrix} \rho A \\ \rho u A \\ \rho\left(e + \frac{1}{2}u^2\right)A \end{bmatrix} \tag{1-2}$$

$$F(\varphi) = \begin{bmatrix} \rho u A \\ (p + \rho u^2)A \\ \rho u\left(e + \frac{1}{2}u^2 + p\rho^{-1}\right)A \end{bmatrix} \tag{1-3}$$

$$B = \begin{bmatrix} 0 \\ p\frac{dA}{dx} - \rho F_R \\ \rho q A \end{bmatrix} \tag{1-4}$$

Here t is time, x is distance, A is area, p is pressure, ρ is density, u is velocity, e is energy, and F_R is a friction term.

It is often difficult to get analytical solutions for these parabolic partial differential equations; thereby, numerical methods are preferable. Different numerical methods have different precisions and fidelity. The characteristic method solves the parabolic partial differential equations by transforming them into linear ordinary equations which provide a first order precision. There are also second order upwind or symmetric methods which have a higher precision.

1.3.2 Linear acoustic method

In the linear acoustic method, the fluid is treated as non-viscous. Only small disturbances of the thermodynamic properties – pressure and density, are considered while the non-linear effects are neglected [32,38]. Also, the mean velocity is assumed to be negligible, and the mean pressure and density are considered as constants with only small fluctuations changing with time and location. The variations in thermodynamic properties can thus be written as follows [46]:

$$p = p_{\mathrm{eq}} + \delta p \tag{1-5}$$

$$\rho = \rho_{\mathrm{eq}} + \delta \rho \tag{1-6}$$

$$u = \delta u \tag{1-7}$$

By applying the continuity and momentum conservation equations, and eliminating the higher order components, the one dimensional conservation equations can be simplified to:

$$\frac{\partial(\delta\rho)}{\partial t} + \rho_{\mathrm{eq}} \cdot \frac{\partial(\delta u)}{\partial x} = 0 \tag{1-8}$$

$$\rho_{eq} \cdot \frac{\partial(\delta u)}{\partial t} + \frac{\partial(\delta p)}{\partial x} = 0 \tag{1-9}$$

$$\frac{\partial(\delta p)}{\partial t} - a_{eq}^2 \frac{\partial(\delta p)}{\partial x} = 0 \tag{1-10}$$

The set of equations above can then be combined to get the acoustic wave equation:

$$\frac{\partial^2(\delta p)}{\partial t^2} - a_{eq}^2 \frac{\partial^2(\delta p)}{\partial x^2} = 0 \tag{1-11}$$

Here δp is a small perturbation of pressure, $\delta \rho$ is a small perturbation of density, δu is a small perturbation of velocity, a is the speed of sound and the subscript ‘eq’ represents the equilibrium state.

Harrison et al. have developed models for various boundary conditions in the intake system based on the linear acoustic theory [42]. As stated above, the linear acoustic theory is based on the assumption that the mean pressure does not change, and the mean velocity is negligible. This method is usually applied for predicting the noise levels from an engine system or the pressure fluctuations in the intake system where the pressure perturbations are not very strong. The advantages of this method are that it is convenient to simulate a complicated system and the results are acceptable when the fluctuations are weak. The exhaust wave actions in engines are accompanied by a highly fluctuating gas flow. When the fluctuation is sufficiently strong, it demonstrates non-linear characteristics, therefore the linear acoustic method is not appropriate to depict the real situation beyond the minor perturbation assumption [27,47].

1.3.3 Hybrid methods

The hybrid methods are developed in ways that use both the linear acoustic theory and the non-linear approach. A hybrid method proposed by Payri used the acoustic description to set the boundary conditions for an unsteady one dimensional nonlinear calculation [31]. The pressure perturbations in the time domain were related to the frequency domain by the Fourier Transform. In each iteration, the pressure in the time domain was transformed into the frequency domain and the value in the frequency domain was updated to the next step and served as the boundary condition. The Fourier and reverse Fourier Transform were conducted in each iteration to transfer the information between the time and the frequency domains. The problem with this method was that the initial value of pressure oscillations was obtained with some approximation. The precision of this guessed initial value affected the speed of convergence. In a complex system, it would be a challenge to find the appropriate initial value.

Sathyanarayana et al. used a hybrid method to calculate the acoustic performance of different mufflers [39]. Unlike Payri, they directly related the variables of the acoustic theory to the variables of the characteristic method and applied the boundary conditions from the frequency domain. Since the characteristic method was used, the precision of this method was only of the first order.

Alternatively Chalet et al. considered the pressure wave action as a damping system, and combined it with the acoustic theory to describe the pressure oscillations [46,48]. This method is more appropriate for applications in which the pressure wave is not very strong.

1.3.4 Properties of pressure wave in an engine system

Depending on the wave propagation direction, a pressure wave can be categorized as either a compression or expansion wave. A compression wave is formed when a high pressure gas is imposed on a low pressure gas momentarily within a limited plenum. When the compression wave propagates, the pressure and the gas flow behind it increase. Conversely, when an expansion wave forms, there is reduced pressure and gas flow behind it. The shock wave is a pressure wave travelling at sonic or supersonic speed, and it is accompanied by an extremely rapid change of pressure and temperature which causes discontinuities. When the pressure profile is compared, the rising edge of this shock wave is much sharper. In an engine system, the pressure wave generated during the gradual opening of the valves is usually not as sharp as a shock wave, yet when the engine speed is very high or the discharged compression wave from the cylinder is strong enough , it can develop into a weak shock wave with a small Mach number (smaller than 1.3)[29,49]. The properties of the pressure wave in engine systems can be summarized from previous publications [38,50,51]:

(1) The flow is highly pulsating. The transient gas flow can be sonic flow under some conditions.
(2) The strong wave action and the fluctuating flow make the wave transmission properties non-linear.
(3) Besides the transient properties of pressure and velocity, temperature in the engine exhaust pipe is also variable.

In the existing literature, the focus is more on general pressure wave properties and/or on model development. Quantitative research on how exhaust pressure waves behave under different engine operation conditions is limited.

1.4 Interactions between pressure wave actions and liquid dosing sprays

As discussed in Section 1.2, researches on engine aftertreatment spray are usually conducted under steady flow conditions. The pressure wave impact is seldom considered.

However, the strong pressure wave and the accompanying high speed gas flow may have substantial impact on the droplet breakup and the spray distribution.

The research of Joseph et al. showed that droplets of various kinds of fluid with diameters of around 2.5 mm broke into a mist within 300 microseconds after a shock wave travelled through [52]. The Mach number in their research was relatively high, up to 3. However, even at a lower Mach number of 1.3, water droplets of 2.7 mm diameter broke up into a mist as described in [53]. Hsiang et al. summarized the regime of droplet breakup and indicated that it was related to the Weber number [54]:

$$We = \frac{\rho_g u_r^2 d}{\sigma} \tag{1-12}$$

and Ohnesorge number[54]:

$$Oh = \frac{\mu_l}{(\rho_l \sigma d)^{0.5}} \tag{1-13}$$

Where ρ_g is the density of gas in the background, u_r is the relative velocity between the gas flow and the liquid droplet, d is the diameter of the droplet, μ_l is the dynamic viscosity of the liquid, ρ_l is the density of the liquid, and σ is the surface tension of the liquid droplet.

The Weber number represents the ratio of the inertial force to the surface tension. The Ohnesorge number relates the viscous forces to the inertia and surface tension. When the Ohnesorge number is small (e.g.. less than 1), it means the effect of viscous force is minor; then the breakup process depends mainly on the Weber number. In most automotive diesel engines, the range of the Ohnesorge number of the in-cylinder diesel spray is less than 1 [55,56]. In the aftertreatment injection with larger droplets, the Ohnesorge number should be even smaller. The main factor for the breakup in this research context is the Weber number, namely the relative gas flow velocity, droplet diameter, and gas density.

In the case of the above mentioned tests, the authors attributed the reason for droplet breakup to the high relative velocity between the gas stream and the droplets when the droplets were exposed to the shock wave. The situation in an engine exhaust system is expected to be quite similar – with the passage of an exhaust pressure wave, the velocity of the exhaust gas could increase significantly and affect the droplet breakup.

1.5 Objective of the thesis

Though there are published results on both aftertreatment injections and pressure wave actions, studies on the interaction of these phenomena are relatively limited. For the complicated gas flow conditions in an engine exhaust system, it is meaningful to investigate the effect of the pressure waves on the performance of the aftertreatment sprays. An improved understanding of these impacts is beneficial for formulating the aftertreatment injection strategies.

Moreover, comprehensive research results on the exhaust pressure wave properties are limited, and a detailed discussion on how pressure waves change under various engine operation conditions can be a valuable reference for the exhaust pressure wave related research.

This study is composed of two main parts. The first part is the measurement of the engine exhaust pressure wave actions under different operating conditions so that a broad understanding of the pressure wave impacts can be developed. Different engine operating parameters will be discussed, such as the effect of load level, backpressure, and EGR on the exhaust pressure wave. The influence of changing the exhaust pipe length and diameter will be discussed as well. However, the pressure wave study is limited to a single cylinder in this work.

The second part presents the preliminary research on the aftertreatment injection in a simulated pulsating gas stream. The major interest here would be investigating the effect of the pressure wave and the associated gas flow on droplet breakup and spray distribution.

1.6 Structure of the thesis

The thesis is organized as follows:

Chapter 1 is an introduction. Information on the research background, along with reviews of relevant literature in this field, is provided in this chapter.

Chapter 2 illustrates the experimental setup as well as the simulation tool used for engine exhaust pressure wave research. The test setup for the aftertreatment spray experiments is also introduced in this chapter. For the pressure wave research, the experimental setup is based on a Ford Puma diesel engine; the simulation tool is the commercial software AVL BOOST (version 2013). Different boundary conditions that one may encounter in the

engine system are also explained in this chapter. The aftertreatment spray research is conducted on a shock tube test setup. The shock tube experimental configurations of this research are described as well.

Chapter 3 describes the test and simulation results of the exhaust pressure wave research. Test results show pressure waves at different operating conditions. The simulation model was first compared to and validated by the test results, and then it was used to simulate the pressure waves at conditions which are beyond the present empirical researches such as the effect of pipe diameter and multi-cylinder manifolds for explanation purposes. The gas flow velocity was also introduced in this chapter and was estimated using the simulation tool. The test and simulation results provided a perspective of how the pressure wave behaves in an engine exhaust system.

Chapter 4 explains the test results of the aftertreatment spray research. Initially, the breakup process of a single droplet along the passage of a shock wave was investigated via optical methods to determine the details of the shock wave-droplet interaction. Then, the effects of the shock wave and gas flow on the spray atomization and distribution were studied preliminarily.

Chapter 5 summarizes the conclusions of this thesis work followed by brief comments on the future work.

CHAPTER 2 EXPERIMENTAL SETUP AND SIMULATION METHOD

The exhaust pressure wave research was conducted on a research diesel engine. Both experimental and simulation methods were used to explore the behavior of the exhaust pressure waves in a practical exhaust system under different engine operating conditions. In parallel, a shock tube device was used to simulate the exhaust pressure wave effect on an aftertreatment spray instead of testing the spray on the engine exhaust pipe directly. Optical tools were used for this part of research.

2.1 Test setup of a Ford Puma engine

A Ford Puma engine was used for the exhaust pressure wave research. The specifications of the engine are provided in Table 2-1.

Table 2-1. Ford Puma engine specifications

Cylinders	4	Exhaust Valve Diameter	28 mm
Type	4-Stroke	Intake Valve Diameter	33.4 mm
Displacement	1.998 Liters	Maximum Exhaust Valve Lift	8.64 mm
Bore	86 mm	Maximum Intake Valve Lift	12.5 mm
Stoke	86 mm	Intake Valve Opening	687 °CA
Connecting rod	160 mm	Exhaust Valve Opening	491 °CA
Compression Ratio	18.2:1	Intake Valve Closing	217 °CA
Valves per Cylinder	4	Exhaust Valve Closing	10 °CA

The original four cylinder engine was modified by isolating the first cylinder from the other three for research purpose. In this way, the interactions between different cylinders on internal combustion could be avoided. The first cylinder was then used for a variety of engine research. The engine was coupled to an eddy current dynamometer used for load and speed control. The engine speed was kept constant at 1500 rpm for all the tests.

The schematic of the Ford Puma engine test setup is shown in Figure 2-1. The research cylinder was fitted with an independent air supply system using an external compressor; thereby the pressure was accurately controlled with multiple pressure regulators. A backpressure valve was fitted in the exhaust system to simulate the turbocharger induced backpressure, and to drive EGR through the EGR valve. A diesel oxidation catalyst (DOC) and an exhaust surge tank were connected in the exhaust system of the single cylinder.

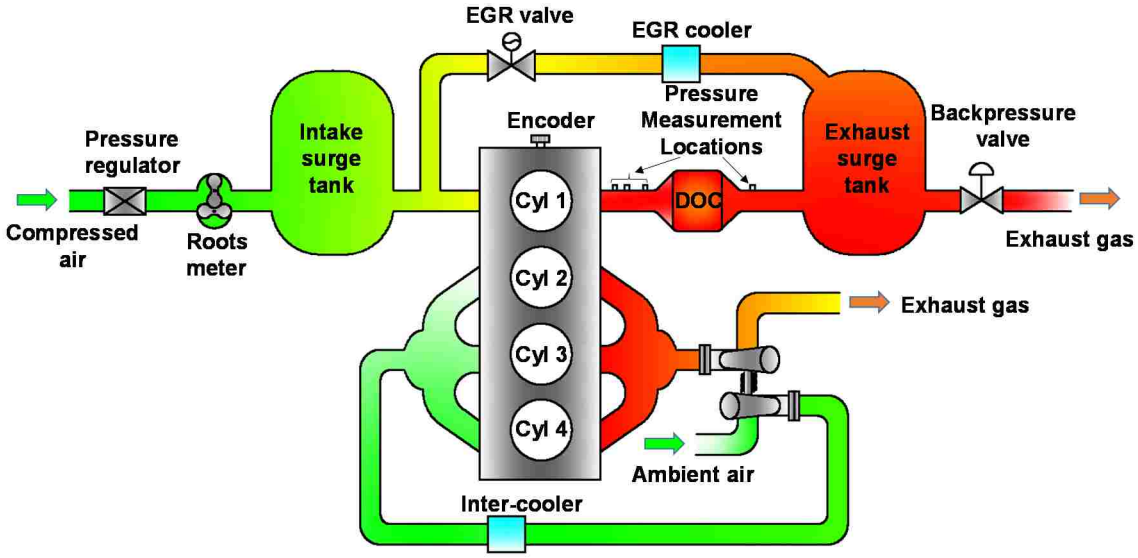

Figure 2-1. Ford Puma engine schematic

Two different exhaust pipe configurations were used in this research (Figure 2-2). The first configuration was fitted with a short runner (0.29 m) which was an original laboratory setup, and the second setup was connected to a longer runner (0.83m) in order to investigate the effect of the runner length. In the short pipe configuration, there were four different adapting ports for the pressure measurement. The first two were on the straight section right after the exhaust flange. Measurement ports 3 and 4 were downstream located before and after the DOC respectively. In the longer pipe configuration, there were only two measurement ports on the straight pipe right after the exhaust flange. Most of the measurements were performed with the short runner configuration. The diameter of exhaust pipes P-1, P-2, P-3, P-4 and P-5 as indicated in the figure was 25.4 mm (1 inch). The diameter of all the other pipes was 38.1 mm (1.5 inches).

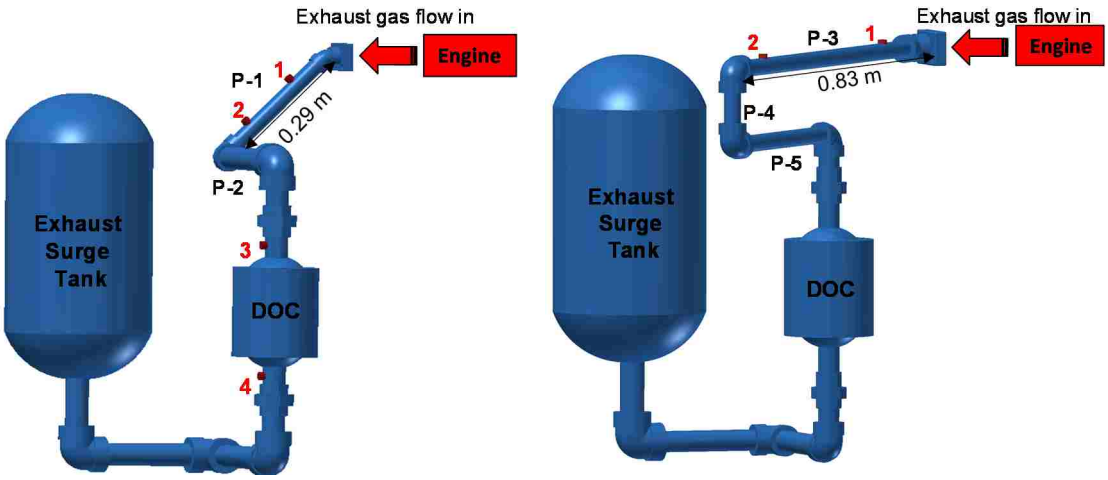

Figure 2-2. Ford Puma engine exhaust pipes

The in-cylinder pressure was acquired using a piezoelectric pressure transducer (model number AVL GU13P, specifications listed in Table 2-2) mounted on the cylinder head. A high precision digital encoder with a resolution of 0.1 °CA was installed on the engine crank shaft. The in-cylinder pressure was recorded for 200 consecutive cycles and averaged to calculate the indicated mean effective pressure (IMEP). A set of real time (RT) controllers with embedded field-programmable gate array (FPGA) were used to control the common-rail pressure, the injection timing, and duration through in-house built control programs based on National Instruments LabVIEW software. The injection pressure was set depending on the specific conditions in each test. The injection timing and duration were also adjusted in each test.

Table 2-2. AVL GU13P pressure transducer specifications

Compensated Operation Temperature	0-400 °C
Measuring Range	0-200 bar
Sensitivity	15 pC/bar
Natural Frequency	130 kHz
Linearity	<0.3%FSO
Cyclic Temperature Drift	<±0.6 bar

The exhaust pressure was measured by Kistler 4075A10 piezoresistive pressure transducers (Figure 2-3) with a sampling frequency of 0.1 °CA. The equivalent sampling

frequency under the testing conditions (1500 RPM) was 90 kHz. The specifications of the pressure transducer are given in Table 2-3.

Figure 2-3. Kistler pressure transducer (4075A10) with the transducer adapter (7507)

Table 2-3. Kistler 4075A10 pressure transducer specifications

Connection	M12X1
Compensated Operation Temperature	20-120 °C
Min/Max Temperature	0-140 °C
Measuring Range	0-10 bar
Overload	25 bar
Sensitivity	50 mV/bar
Natural Frequency	>120 kHz
Linearity	<0.3%
Tightening Torque	12~20 N-m
Weight	28 g
Accuracy	<±0.03 bar

Similar to the in-cylinder pressure, the pressure acquired from the exhaust pipe was the averaged value over 200 consecutive cycles. The measuring range of the pressure transducer was 0-10 bar absolute pressure and the natural response frequency of the sensor was about 120 kHz, which was sufficient for the pressure wave measurements in this research. The total error of the pressure transducer measurement was less than ±0.03 bar within the compensated operation range according to the manufacturer's report [57] [58]. The signal from the transducers was then transmitted to Kistler 4618A0 amplifier (Figure 2-4). The specifications of the amplifier are given in Table 2-4 [59]. The amplified signal was sent to a National Instrument data acquisition card connected to a personal computer.

Figure 2-4. Kistler pressure transducer amplifier (4618A0)

Table 2-4. Kistler 4618A0 amplifier specifications

Power Supply	
Supply voltage	18-30 VDC
Current consumption	<40 mA
Amplifier Input	
Input impedance	1012 Ω
Input voltage range	50-1000 mV
Voltage Output: Pressure	
Range	0-10 V
Output impedance	10 Ω
Current Output: Pressure	
Range	4-20 mA
Operating temperature range	0-60 °C

The compensated operational temperature of the transducer was between 20-120 °C, while at the high load operating conditions, the exhaust temperature could exceed 500 °C. In order to prevent any possible damage to the pressure transducers, a water cooled adaptor was used for this application – Kistler 7507 (As shown in Figure 2-3). A water recirculation circuit for cooling the transducers was developed by the author comprising of a water tank, a pump, a control valve, and assorted supply and return hoses. The power supply of the water pump was 12 V DC. A thermocouple was inserted into the water tank to measure the water temperature. The temperature signal was transferred to the computer

and monitored during the test. The warning temperature was set to 50 °C to avoid damage to the transducers and water pump. A pressure gauge was mounted to display the pressure in the cooling circuit. Overload on the pump or leakage from the circuit could be detected from the pressure reading. The cooling system is shown in Figure 2-5. Ice cubes were usually used to cool down the water before the test. The initial water temperature was around 10 °C and depending on the engine operating conditions, it could reach more than 40 °C after two hours of continuous operation.

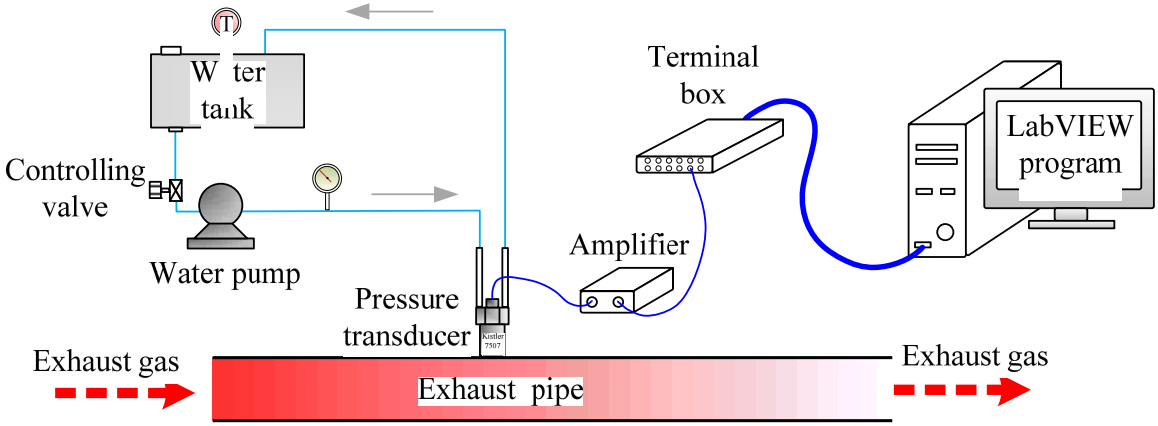

Figure 2-5. Signal recording and cooling system for the pressure transducers.

2.2 Simulation models for exhaust pressure wave research

The models for pressure wave simulation are mostly based on one-dimensional (1-D) assumptions. The 1-D simulation can largely decrease the requirement for computational resources when dealing with complicated engine systems. Unlike the conditions in the intake pipe where the pressure fluctuations are relatively minor, the pressure waves in an exhaust system are quite strong. It is not appropriate to use the acoustic method in the exhaust pipe. The 1-D gas dynamic method in the commercial software AVL-BOOST was used in this study.

2.2.1 AVL BOOST

AVL-BOOST is a one-dimensional simulation tool developed for modelling the engine system. This commercial software contains a spectrum of elements such as pipes, cylinders, plenums, junctions, and coolers. A user can build a system and define relevant parameters such as information on length, volume, temperature, and pressure. The non-linear one dimensional governing equations discussed in Section 1.3.1 are also used in the

BOOST simulation. As it is a one-dimensional tool, the flow loss due to three-dimensional effects is considered in the form of loss coefficients which should be provided by the user.

An essentially non-oscillatory (ENO) shock capturing scheme is used to solve the non-linear governing equations. The scheme is based on a finite volume approach. The value at the end of the time step is calculated using the value at the beginning of the time step and the flux through the cells' borders. The mass, momentum, and energy flux can be calculated through the conservation equations, which provide the relation between the flux through the control volume and the rate of flux in the time domain [60]. The ENO schemes use the idea of adaptive stencils to automatically achieve high order accuracy and non-oscillatory property near the discontinuities. This method enables the calculation of strong pressure waves that one may encounter in an engine exhaust system. In the shock-capturing approach, the partial differential governing equations are cast in conservation form and any shock waves or discontinuities are computed as part of the solution.

Besides the one-dimensional calculation of pressure wave action, the AVL-BOOST simulation package also provides various zero dimensional combustion models such as single Vibe (also referred to by the alternate spelling "Wiebe") function, constant volume, and constant pressure models which also enable the simulation of different combustions conditions. Alternatively, it can use the measured in-cylinder pressure as the boundary condition. The focus of this research is on exhaust pressure wave actions at various engine operation conditions instead of the in-cylinder combustion process. So, in order to avoid any discrepancies caused by the in-cylinder combustion simulation, the measured in-cylinder pressure data was taken as input information for pressure wave simulation in most cases. In the simulations for which the empirical data was not available, the injected fuel amount was defined and the Vibe model was used to describe the heat release shape of the combustion. The in-cylinder pressure and temperature were calculated from the heat release. The details of this process can be found in the BOOST Users Guide and BOOST Theory [60,61].

The heat transfer effect is simulated in AVL-BOOST by heat transfer models such as Woschni (1978 and 1990), Hohenberg (1980), and AVL 2000 [60,61]. The Woschni

(1978) heat transfer model was used in the simulations. Surface areas and the temperature of the walls, as well as the gas temperature were provided as inputs. The exhaust gas temperatures were measured at different locations during the tests and the values were used in the simulations. The cylinder wall temperature was set to the same value as the engine coolant temperature from the measurement, and the exhaust pipe wall temperatures were estimated. The friction effects caused by the pipe roughness and the pipe elbows were represented by the flow coefficients, which were also user-defined.

2.2.2 Modeling of the engine system components

The components in an engine system include cylinders, pipes, plenums, valves, catalysts and so forth. These components are described by models in AVL BOOST, which are used to represent the complete engine system in the software. The detailed equations describing these models are shown in Appendix-A. The models of the major components used in this research are briefly described in this section.

- Cylinder [60]

The thermodynamic status inside the cylinder is calculated from the first law of thermodynamics. The conservation of energy and mass, together with the ideal gas equation are used to calculate the in-cylinder pressure, temperature, mass, and other thermodynamic properties. The transportation of the gas between the cylinder and the valve ports is modelled by the orifice flow equations.

- Pipe [60]

The one dimensional pipe flow is described by the conservation equation of mass, momentum, and energy. The friction loss or the loss due to the diameter change are represented by flow coefficients which should be determined by the user.

- Elbow [60]

Pipe elbows are common components in engine system. In a 1-D gas dynamic simulation, the effect of pipe elbows is treated as a friction loss coefficient. This loss coefficient is a function of the bend angle and the ratio between the bend radius and the pipe diameter.

- Catalyst [60]

The AVL BOOST software can simulate both the gas dynamics and the chemical reactions in the catalysts. In this research the chemical reactions were not taken into consideration. The gas dynamic properties of catalysts are simulated using the same

model as in the pipe system. In addition, the information about the small channels in the honeycomb substrate such as cell density and wall thickness, as well as the volume and the length of the catalyst can be provided by the user. A laminar or turbulent friction coefficient can be defined to calculate the friction loss when flow occurs through the small channels.

2.3 Experimental set up for the research of the aftertreatment spray

Due to the high temperature environment in the engine exhaust system, it is difficult to have any direct optical access on the exhaust pipe. So in this research, a shock tube device was used to simulate the exhaust pressure wave, without applying an actual high temperature condition.

2.3.1 Typical shock tube configuration

A shock tube is a device that can be used to generate a shock wave. A typical configuration is composed of two sections separated by a diaphragm, one with higher pressure called the driver section and the other with lower pressure referred to as the driven section as shown in Figure 2-6. When the diaphragm between the driver and the driven sections bursts, a shock wave is formed and it propagates into the driven section. Meanwhile, a series of expansion waves (expansion fan) travel into the driver section. The contact surface of the gas also moves towards the driven section at a lower speed.

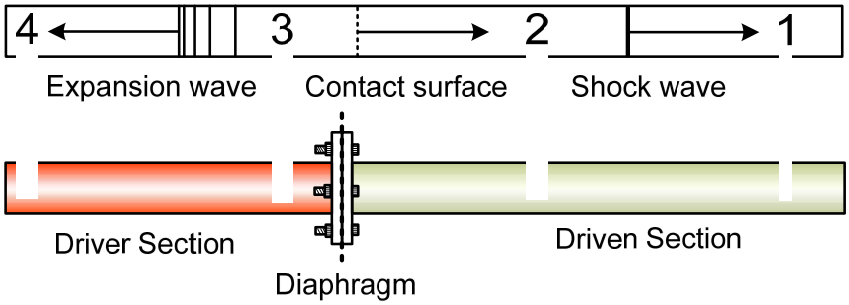

Figure 2-6. Shock tube schematic

As indicated in Figure 2-6, regions 1 and 4 represent the initial condition in the driven and driver sections respectively, region 2 is located between the shock front and the gas contact surface, and region 3 is located between the gas contact surface and the expansion wave. The relations of pressure as well as speed of different regions are described in the equations in Appendix B:

In a shock tube, the flow region can be divided as follows [62]:

(1) Shock moving towards the end of driven section, with a wave speed W;

(2) A region of uniform quasi-steady flow to the driven section (velocity U_p), which is defined as region 2;

(3) A temperature (that is, density) discontinuity moving to the driven section;

(4) A second region of uniform quasi-steady flow to the driven section (velocity U_p), which is defined as region 3;

(5) The head of the reflected rarefaction wave moving to the driver section.

In our case, as the end of the driven section is open, there is no reflected shock wave as stated in literature [62]. When air is used as the medium and the initial temperature is room temperature, the shock wave strength and the gas flow velocity after the shock front can be calculated as shown in Figure 2-7.

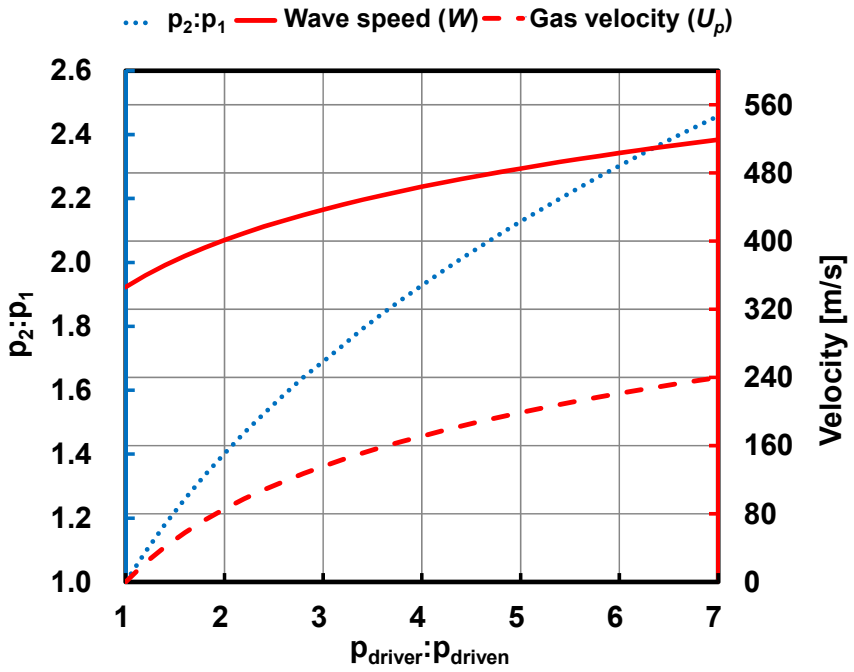

Figure 2-7. Shock wave relations with air as the medium in both sections

2.3.2 Shock tube test set up

A micro shock tube was set up at the Clean Diesel Engine Laboratory. The driver section of the shock tube was 36 cm long with an inner diameter of 23.8 mm and a wall thickness of 12.5mm. The driven section was 100 cm long with a similar inner diameter.

A low speed SSI Technologies pressure transducer (model number: P51-200-S-A-I36-5V-000-000) was mounted on the driver section 15 cm away from the diaphragm. This transducer was used to measure the charging pressure and record the diaphragm burst pressure. The specifications of this pressure transducer are listed in Table 2-5. Two high speed pressure transducers were installed on the driven section to record the shock wave propagation. The pressure transducers were the same Kistler pressure transducers (4075A10) used for engine exhaust pressure wave measurements. Their specifications were described in Table 2-3 and Table 2-4. The first pressure transducer was 10 cm away from the diaphragm and the second one was 90 cm away from the diaphragm. Multiple sensor mounting ports enabled the measurement and calculation of the pressure waves at different locations.

Table 2-5. SSI P51 pressure transducer specifications

Operation Temp	-40-105 °C
Connection	1/4-18 NPT
Measuring Range	0-200 psi gauge
Supply voltage	8-30 volts
Full scale output (FSO)	5 volts
Zero pressure output	1 volts
Response Time	< 1 ms
Accuracy	±0.5% FSO

When the first pressure transducer on the driven section detected an increase in pressure caused by the shock wave, a trigger signal was sent out to trigger the data recording. The signals from the three pressure transducers were transmitted and recorded on a real time controller (RT) simultaneously. A LabVIEW program was used to control the data recording process. The pressure data from 20 ms before until 30 ms after the trigger were recorded. The sampling frequency of the pressure data was 100 kHz.

Different types of diaphragms were used in the shock tube test to create different burst pressures. In this way, shock waves of different strengths could be generated. The main diaphragm materials and their common burst pressures are shown in Table 2-6. In these

tests, the diaphragm burst pressure was not quite consistent but was generally limited within a certain range. The burst diaphragms are shown in Figure 2-8.

Table 2-6. Diaphragm materials and burst pressure

Diaphragms	Burst pressure [bar abs]
1 Aluminum foil layer and 2 paper layers	4-5
1 Aluminum foil layer and 1 paper layer	3.5-4.3
2 Wax paper layers	2.2-2.5
1 Wax paper layer	1.8-2.2
1 Aluminum foil layer	1.6-1.9

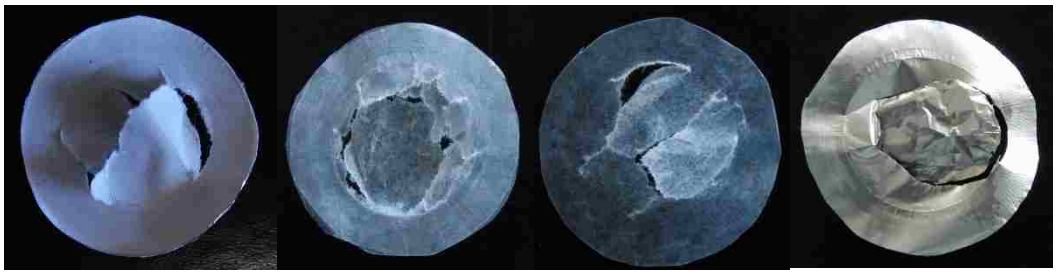

(a)1 Al and 1 paper (b) 2 Wax papers (c) 1 Wax paper (d) 1 Al foil

Figure 2-8. Burst diaphragms

In order to study the effect of the pressure wave and the gas flow on the aftertreatment spray, first, a single droplet was suspended at the open end of the shock tube to see the changes in detail. Thereafter, an injector was placed at the end of the tube to investigate the effect of the pressure wave on the aftertreatment spray.

Since the shock wave speed was considerably high (e.g., it can be more than 300 m/s), in order to catch the droplet breakup process, a Vision Research Phantom v7.3 high speed camera was used. The camera control and image processing were performed using the Phantom Camera Control Version 8.5 software. This camera had the capability to record at maximum resolution of 800 X 600 pixels at a speed of 6688 frames per second (fps), or maximum frame rate of 222222 fps under standard mode with a resolution of 32 X 8 pixels. In this research, in order to capture the single droplet breakup process and yet have a reasonable view area, the camera speed was set to 40000 fps with a resolution of 512x128 pixels and an exposure time of 8 μs. For the injection test, the speed was set to

20000 fps with a resolution of 256 x 512 pixels and an exposure time of 47 μs. All the droplet or spray images were acquired at room temperature.

Figure 2-9 and Figure 2-10 show the test set up for the single droplet test and the injection test respectively. First, shadowgraph images were taken for the tests. This was done in order to determine whether the shock wave itself had any influence on the droplet breakup. Two Edmund Optics parabolic optical mirrors were used in this test. The mirrors were 152.4 mm (6 inches) in diameter and the focal length was 1219.2 mm (48 inches). A Light Emitting Diode (LED) was used to provide the light source for the shadowgraph tests.

Then, direct images were taken to observe the droplet breakup and the distribution of the spray. The camera was triggered by the same pressure transducer trigger used for the pressure data recording. In this way, the reference initial time was the time when the pressure wave arrived at the first pressure transducer which was located 10 cm from the diaphragm.

The compressed air was used to pressurize the driver section of the shock tube. The pressure was controlled by a pressure regulator. For the spray test, compressed nitrogen was used to pressurize the water tank for the injector (Figure 2-10). The water tank could withstand up to 10 bar absolute pressure. For this set of tests, the injection pressure was set to approximately 4 bar absolute. For safety reasons, only water was used for spray tests. The injector used was a Bosch V14 low pressure injector. The specifications of the injector are listed in Table 2-7.

Table 2-7. Bosch V14 injector specifications

System pressure	Max. 8 bar
Weight	≤ 30 g
Installation lengths	60-65 mm
Spray type	E (2-Spray)
Operating temperature	-40-110°C
Permissible fuel temperature	≤ 70 °C
Power supply	6-16.5 V

Prior to actually running the spray test, a set of spray images were taken to show the spray development under conditions without any external interference. This set of photos were taken using the Canon EOS REBEL T5i Digital Single Lens Reflex (DSLR) camera. This camera was a low speed camera, but with an in-house developed high speed LED light, it was able to catch images over a very short exposure time (e.g., 1-2 μs). In this way, by controlling the LED flash timing with respect to the injection command, the spray development over a period of time was captured. The photos taken with this method had a very high resolution and clearly showed the spray pattern which will be discussed in Chapter 4.

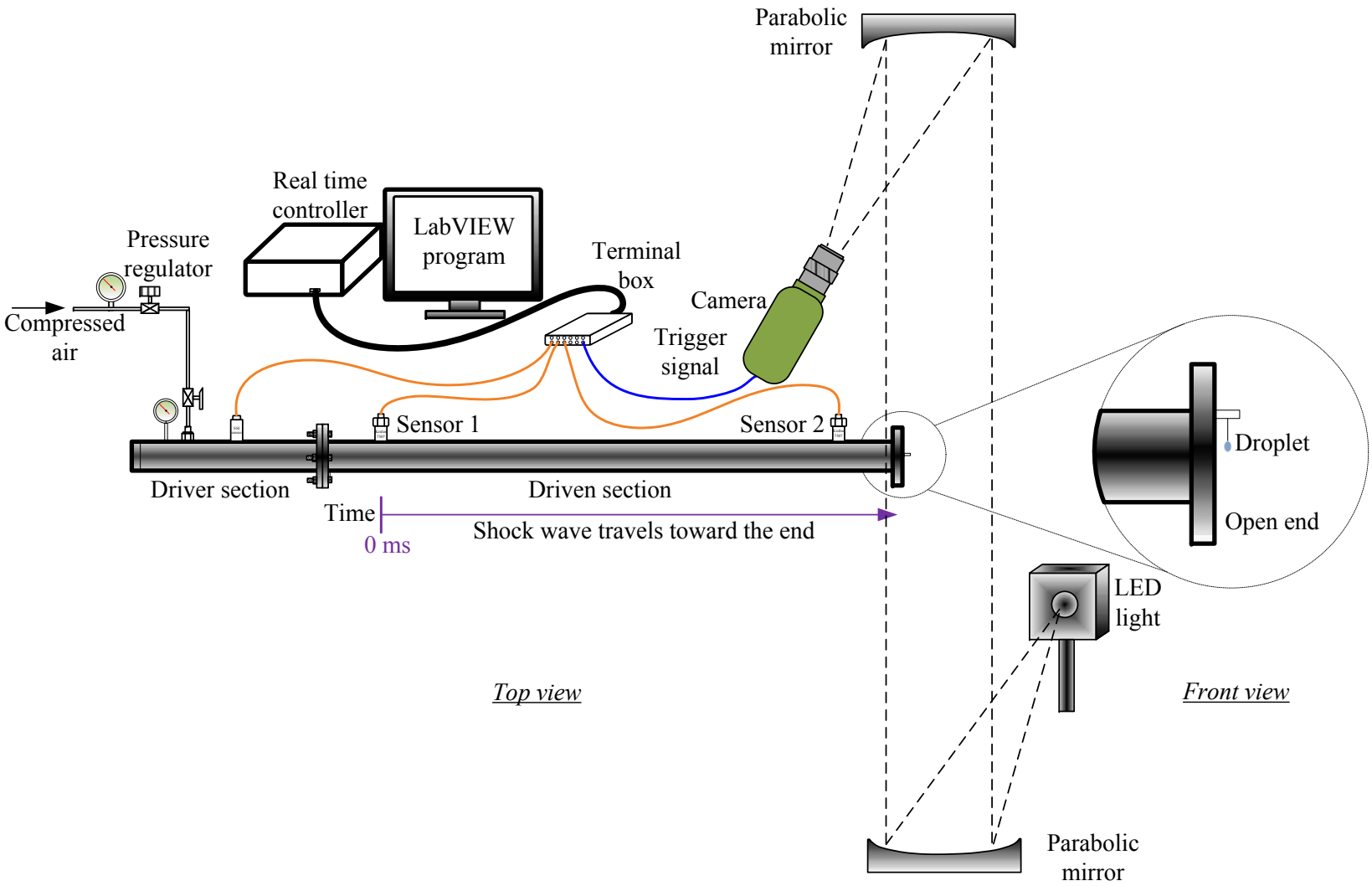

Figure 2-9. Shock tube test set up with a single droplet

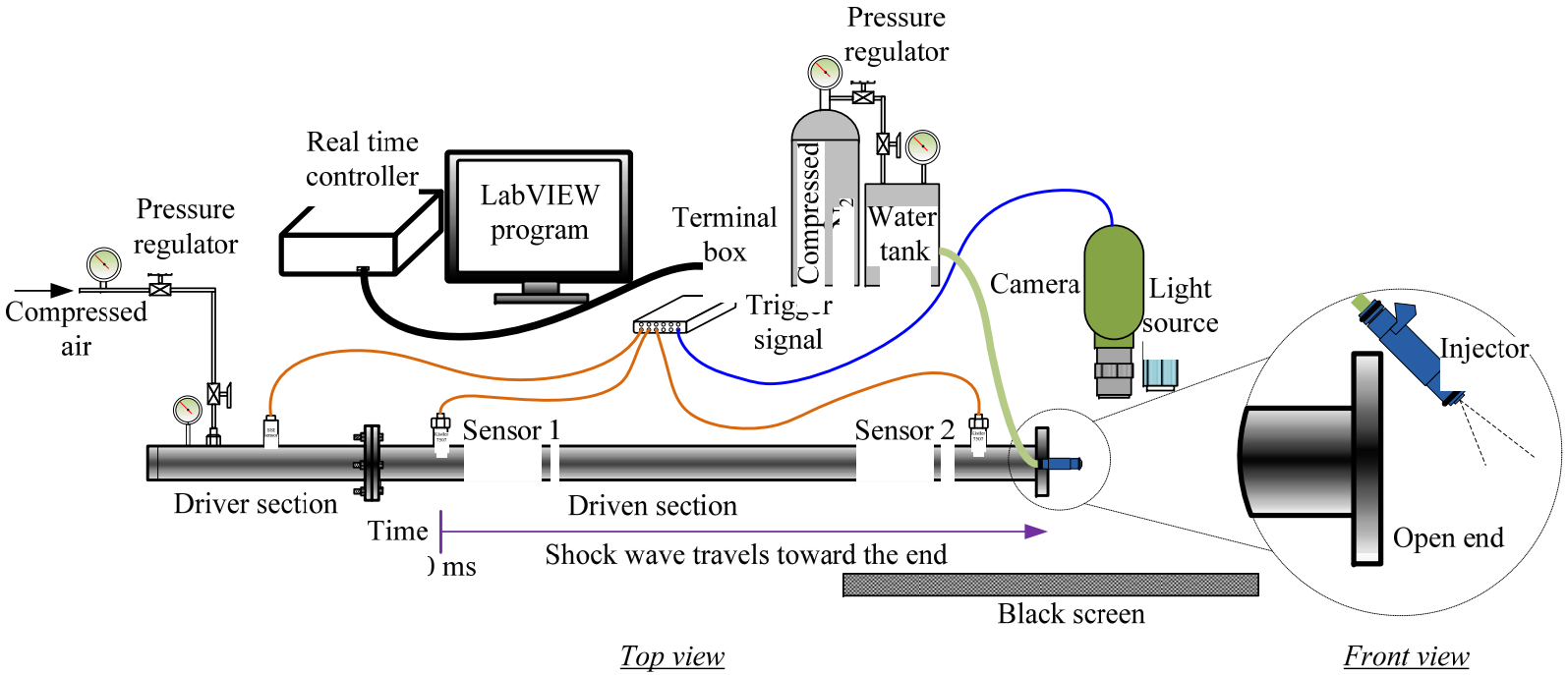

Figure 2-10. Shock tube test set up with aftertreatment spray

CHAPTER 3 EXHAUST PRESSURE WAVE RESULTS

Results obtained from both experiments and simulations with the Ford Puma engine system are discussed in this chapter. These results cover a wide range of engine operation conditions including varied load levels and diverse backpressure settings, and with different engine exhaust configurations such as varied runner length. Different engine running strategies are described as well, such as exhaust gas recirculation (EGR), and post injections. The results provide a general idea on how the exhaust pressure waves and gas flow will change with the engine operating condition variations.

The first section describes the experimental results of pressure waves. The influence of the engine operating parameters on exhaust pressure waves are discussed in this section.

However, the pressure measurement alone does not provide enough information about the gas flow properties in the exhaust pipe. As direct measurements of the exhaust gas flow velocity are difficult due to the high temperature environment in the exhaust system, a simulation tool is used to get more detailed information of the exhaust gas flow. Simulation results complement the experimental measurements. The second section explains the simulation results.

3.1 Empirical results

The development of exhaust pressure waves is discussed with respect to the measured in-cylinder pressure and exhaust pressure traces as shown in Figure 3-1. The development of the exhaust pressure wave is closely related to the piston and valve movement as well as the conditions inside the cylinder and the exhaust pipe. In Figure 3-1, p_{c_EVO} refers to the in-cylinder pressure at exhaust valve open (EVO); p_e represents the pressure in the exhaust pipe at EVO which is similar to the value of the mean backpressure in the exhaust system. p_{e_max} is the highest value of the exhaust pressure within the cycle, which is usually the peak of the first compression wave after EVO.

The exhaust pressure wave in a single cylinder system has three distinctive phases within a complete engine cycle. The first phase starts from the time when the exhaust valves open (EVO). When the exhaust valves open after the combustion top dead center (TDC), the in-cylinder pressure drop rapidly. This process is often referred to as the “blow down” process [51]. Meanwhile a compression wave is released from the cylinder, and raises the exhaust pressure to the first peak value which is usually the highest (p_{e_max}). When the

exhaust valves open wider, the upstream pressure decreases. Then, the piston continues to move towards the bottom dead center (BDC at 540 °CA).

The second phase is the displacement phase during the exhaust stroke when the piston pushes the exhaust gas out of the cylinder. This process produces the second peak of exhaust pressure in the cycle.

The third phase is defined as the condition when the exhaust valves are closed. The exhaust valves close shortly after 720 °CA. The wave reflection and transmission continue in the exhaust system. This reveals that the most significant pressure wave action occur during the valve open period, while the fluctuations are minor when the exhaust valves are closed.

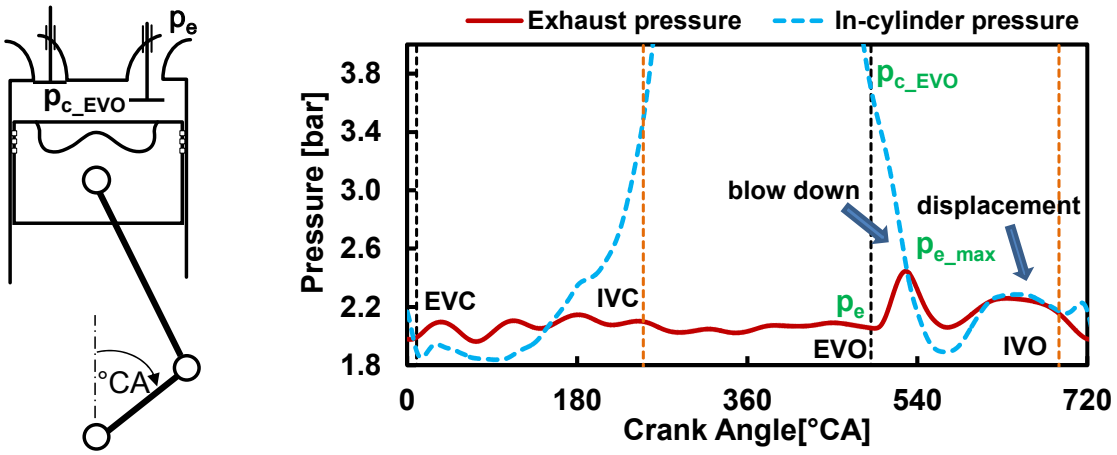

Figure 3-1. Indication of the in-cylinder pressure and the exhaust pressure

The results of over 300 tests were analyzed, and the relations between p_{c_EVO}, p_e and p_{e_max} were derived (Figure 3-2). The pressure ratio between the peak exhaust pressure and the backpressure (p_{e_max}/p_e) was almost linearly related to the ratio of the in-cylinder pressure and the backpressure (p_{c_EVO}/p_e). This suggested that when the backpressure was the same, a higher in-cylinder pressure led to a higher peak exhaust pressure. Again, if the in-cylinder conditions were similar, a larger backpressure suppressed the pressure rise in the exhaust pipe during the blow down process. This relation was valid across a wide range of engine operating conditions with different loads, backpressure, and temperature. During the motoring conditions however, as the exhaust pressure reached the peak value during the displacement process, p_{e_max} was not directly related to p_{c_EVO}. It should be emphasized that all the test data shown in Figure 3-2 were acquired with the same

experimental setup. The relation between the in-cylinder pressure and the exhaust pressure might change when the experimental setup was altered.

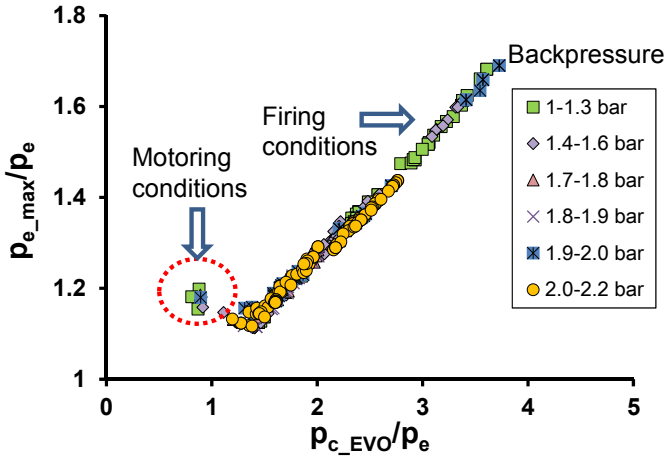

Figure 3-2. Relation between the exhaust pressure and the in-cylinder pressure

The following subsections discuss in detail about how exhaust pressure waves change with different engine operating parameters. For the exhaust pressure wave research, the timing of the exhaust valve opening (EVO) is very important in the cycle. In the following discussion, the time of EVO is often used as the reference time in the cycle. Starting from EVO, the compression wave created right after EVO is referred to as the first peak and the compression wave during the displacement process is referred to as the second peak.

3.1.1 Comparison of pressure wave at motoring and firing conditions

Since a motoring engine is easier to manipulate than a firing engine, many researchers use motoring engines to produce pressure waves for research [50,63–65]. A comparison of the exhaust pressure waves at motoring condition and firing condition is presented in this subsection. The results indicate that during the displacement process, the exhaust pressure waves at both conditions are quite similar. However, the significant compression wave produced in the firing condition during the blow down process is not observed at motoring condition.

3.1.1.1 Pressure waves at motoring condition

The test results of in-cylinder pressure and exhaust pressure of two consecutive cycles at location 1 (Figure 2-2) are shown in Figure 3-3. The engine was running at 1500 rpm, and both the boost pressure and backpressure were set to 1.9 bar.

At motoring condition, the in-cylinder pressure is mostly dependent on boost pressure and the compression ratio. Usually, the in-cylinder pressure at EVO is much lower than that at the firing conditions. Under this test condition, the backpressure is slightly higher than the in-cylinder pressure at EVO. So, the "blow down" process is not observed in this case.

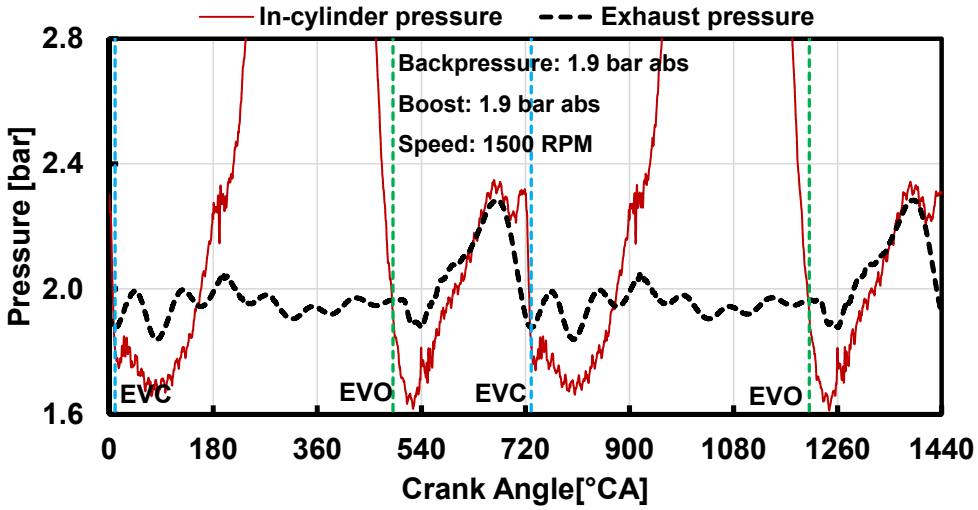

Figure 3-3. In-cylinder pressure and exhaust pressure at motoring condition.

When the exhaust valves opened, the exhaust pressure dropped slightly and the in-cylinder pressure decreased continuously until the piston reached the bottom dead center (BDC@540 °CA). After BDC, the piston moved up to the top dead center (TDC@720 °CA). Both the in-cylinder and the exhaust pressure increased during this displacement process. The exhaust pressure trace followed the in-cylinder pressure during the exhaust valve open period. When the exhaust valves were closed, there were some small fluctuations of the exhaust pressure.

3.1.1.2 Pressure waves at firing condition

In the experiment, the engine speed as well as the backpressure and boost pressure were set to the same values as the motoring condition except that the engine was fired. The results of the in-cylinder pressure and the exhaust pressure at location 1 are shown in Figure 3-4. At firing condition, the in-cylinder pressure was higher than the exhaust pressure at EVO, so there was a compression pressure wave which travelled into the exhaust pipe. Then, the in-cylinder pressure decreased as the piston moved towards BDC and increased again when the piston pushed the exhaust gas out of the cylinder. This

produced another compression wave in the exhaust pipe. When the exhaust valves closed, the pressure fluctuation reduced in a manner similar to the motoring condition.

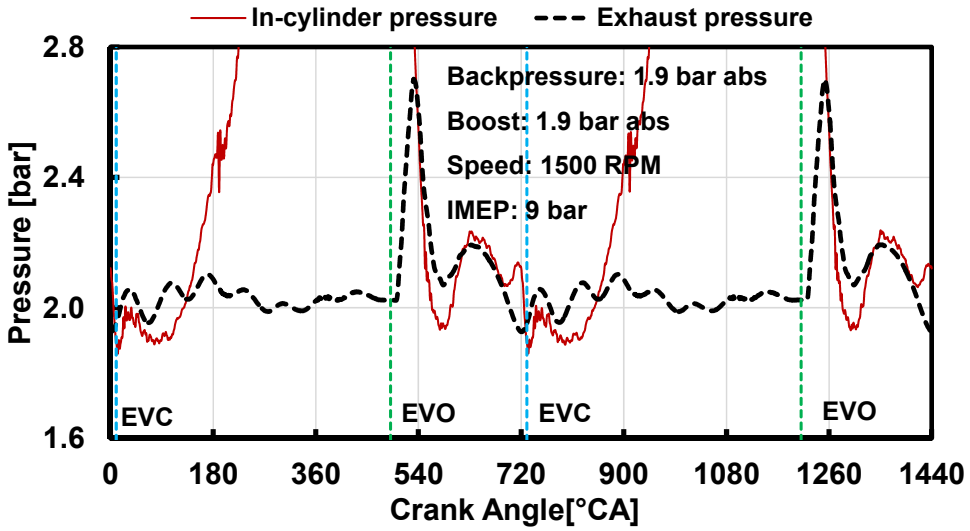

Figure 3-4. In-cylinder pressure and exhaust pressure at firing condition.

The comparison of firing and motoring conditions revealed that the exhaust pressure wave was mainly affected by the conditions inside the cylinder and the exhaust during the exhaust valve open period. When the exhaust valves were closed, the reflected and the transmitted pressure waves were similar in these two cases. Over all, the wave actions were weak when the exhaust valves were closed at both firing and motoring conditions.

3.1.2 Effect of engine load

The exhaust pressure waves under different engine loads are discussed in this section.

The pressure wave got stronger with increasing load level as shown in Figure 3-5. The load level was controlled by the injected fuel amount. The fuel used was diesel fuel. Other engine parameters such as backpressure, boost pressure, and the combustion phasing (CA50) were the same in all the three cases. The fuel timing was adjusted to maintain the combustion phasing.

Load level was represented by the indicated mean effective pressure (IMEP). When the exhaust valves opened, at a higher load, a compression wave with a higher peak pressure value was released into the exhaust pipe. As shown in Figure 3-6, higher IMEP led to higher in-cylinder pressure during the expansion stroke. The increased in-cylinder pressure at EVO caused a stronger exhaust pressure wave. So, the first peak of the exhaust pressure rose with elevated load (Figure 3-5). The second peak of the exhaust

pressure wave was mainly caused by the movement of the piston. It did not show much difference when the engine was running at the same speed. Though the peak value of the first compression wave increased with load, its phase did not change significantly. The peak value was achieved at around 530 °CA for all the three conditions. The phase of this compression wave was controlled by the valve movement. The valve timing was constant for all the test conditions, so the phase of the first compression wave was fixed. The duration of the compression wave, however, was prolonged with increase in load. A phase shift was observed during the time when the exhaust valves were closed. This was caused by the increased temperature at elevated load level. Pressure waves could be expected to travel faster at higher temperature.

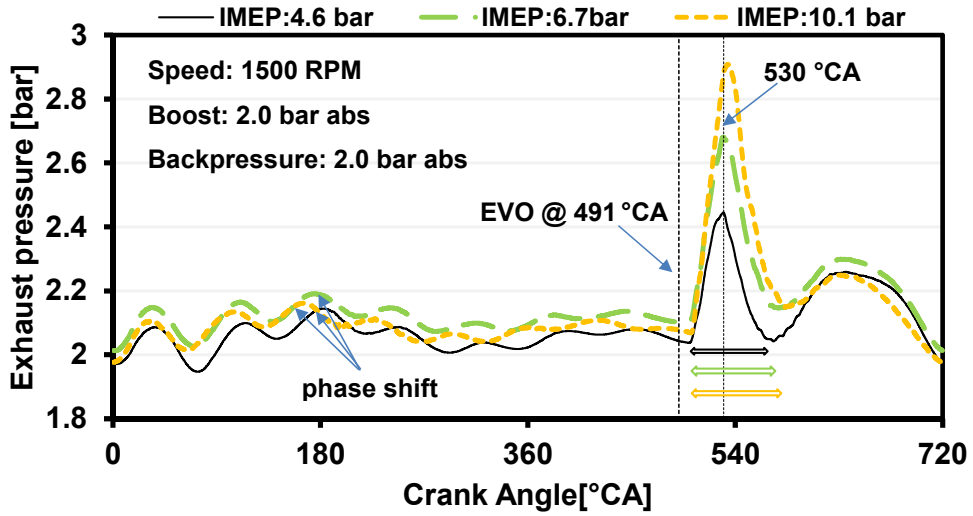

Figure 3-5. Exhaust pressure with changed engine loads

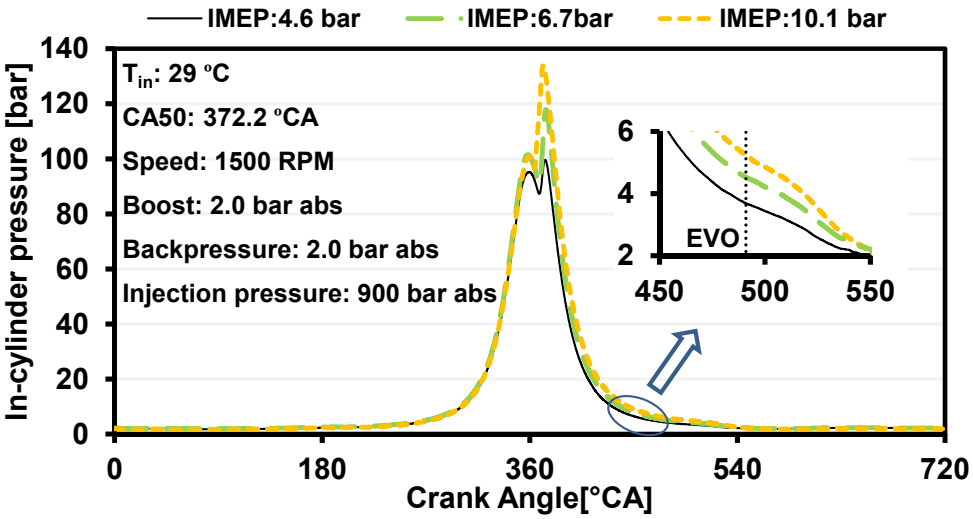

Figure 3-6. In-cylinder pressure with changed engine loads

3.1.3 Effect of post injection

Post injection is a strategy often used in diesel engines for emission control. By injecting fuel during the expansion stroke, the heavy hydrocarbons of diesel fuel cannot be completely burned; instead they are converted into lighter hydrocarbons and hydrogen. These species are beneficial for NOx conversion in the aftertreatment system. Post injection can also effectively increase the exhaust temperature which is desirable for optimum performance of the aftertreatment converters such as the regeneration of the DPF. In this section, the pressure wave actions at different post injection conditions are compared.

3.1.3.1 Comparison between with and without post injection

Figure 3-7 illustrates the heat release rate without post injection, with 1 post injection, and 2 post injections, respectively. The main injection was at 359 °CA with a duration of 450 μs, and the first and the second post injections were commanded at 380 °CA with a duration of 400 μs, and 400 °CA with a duration of 300 μs, respectively. The injection pressure was kept constant at 900 bar. When a post injection was added, the in-cylinder pressure at EVO increased significantly as indicated in Figure 3-8. The exhaust pressure wave was also enhanced as shown in Figure 3-9. The duration of the compression wave tended to be longer when the compression wave got stronger (indicated by the arrows in the figure). A phase shift also occurred when the exhaust valves were closed, which was mainly due to the increased exhaust temperature.

The post injections had a strong effect on the exhaust temperature and the pressure wave. As illustrated in Figure 3-7, the IMEP increase caused by the post injection was less than 4 bar (from 3.8 bar to 7.5 bar), while the exhaust temperature increased by more than 100 °C. The exhaust peak pressure also increased from 2.3 bar to 2.9 bar as shown in Figure 3-9. When compared to the different load level cases in Section 3.1.2, a similar peak exhaust pressure (about 2.9 bar) was achieved when the IMEP level was as high as 10 bar.

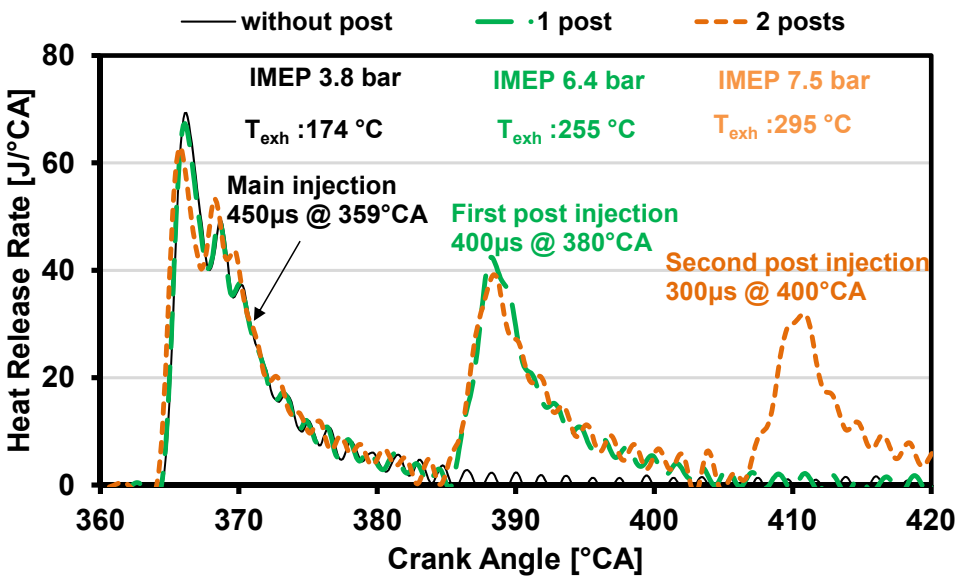

Figure 3-7. Heat release rate with different post injections

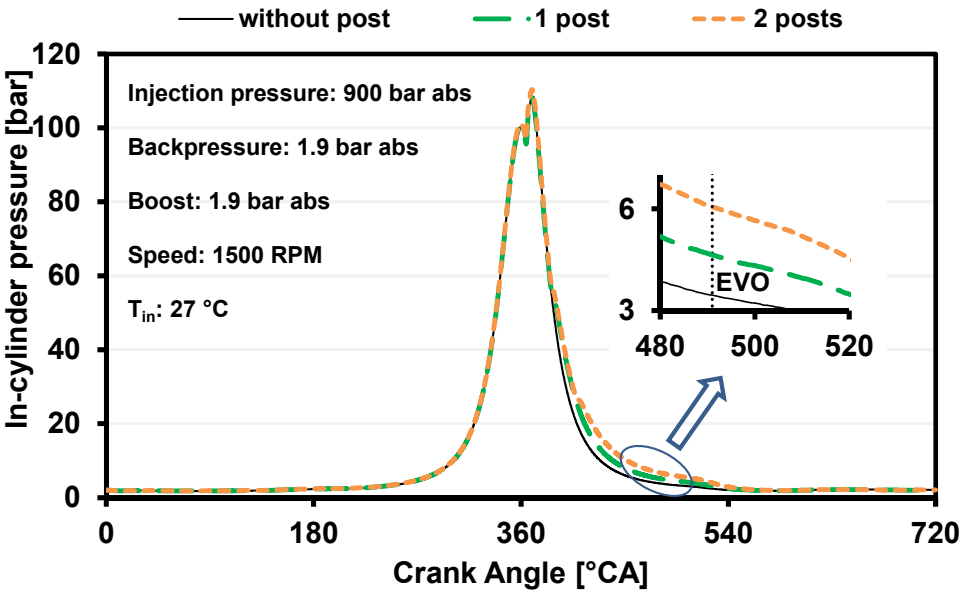

Figure 3-8. In-cylinder pressure with different post injections

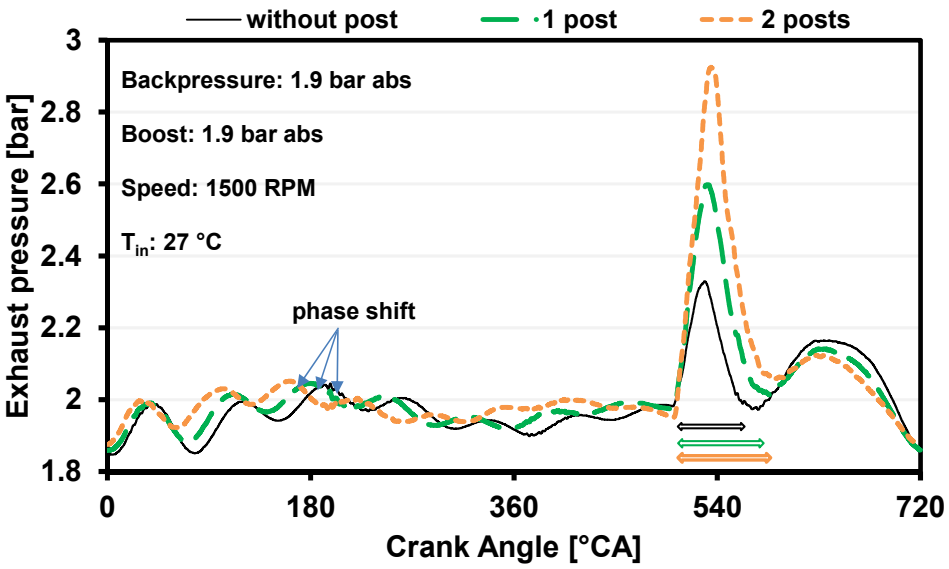

Figure 3-9. Exhaust pressure with different post injections

3.1.3.2 Effect of post injection durations

The effects of the post injection duration are shown in Figure 3-10 to 3-12. In this set of tests, the duration and the timing of the main injection and the first post injection was fixed. The main injection was commanded at 359 °CA and the first post was added at 380 °CA. The durations of the main and the first post injection were 450 μs and 400 μs, respectively. The duration of the second post injection was prolonged from 300 microseconds to 650 microseconds as illustrated in Figure 3-10. With the increased post injection duration, p_{c_EVO} increased from 5 bar to more than 8 bar as indicated by the green dot in Figure 3-11. Since more heat went into the exhaust gas, the exhaust temperature increased by 200 °C. The exhaust pressure wave was also significantly enhanced as shown Figure 3-12.

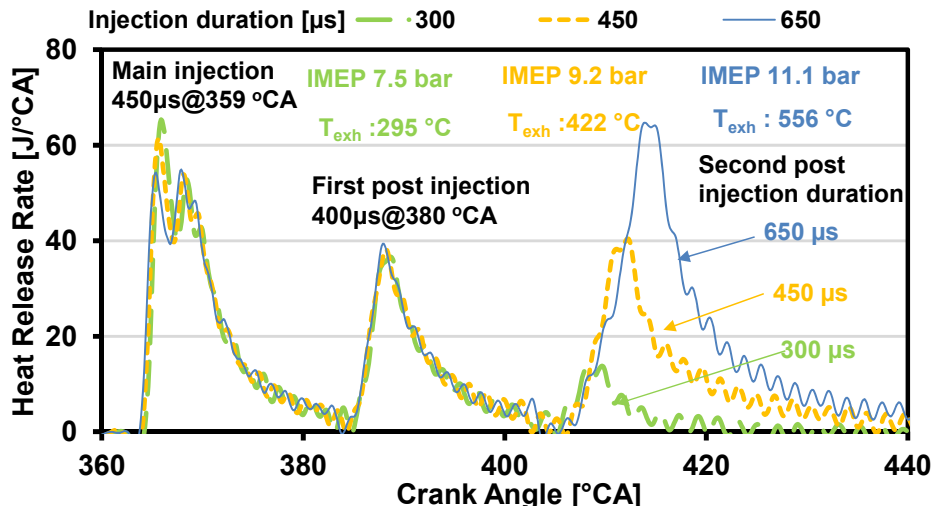

Figure 3-10. Heat release rate with different post injection durations

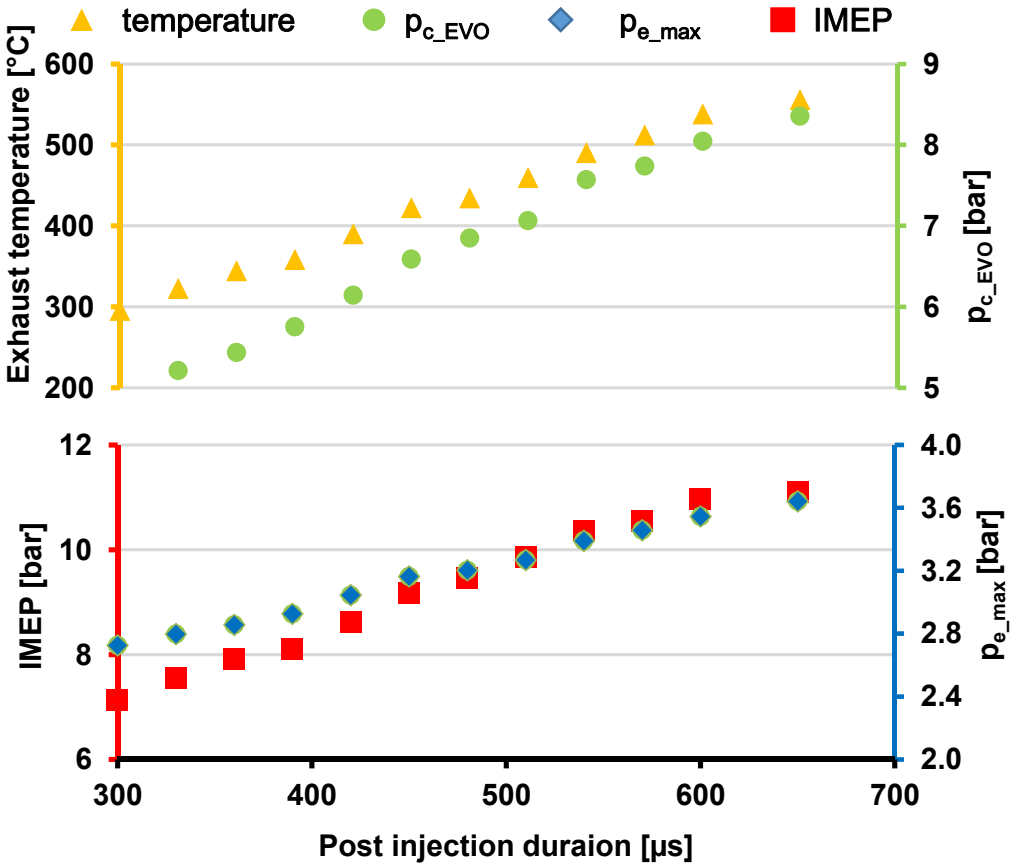

Figure 3-11. Pressure, temperature and IMEP vs different post injection durations

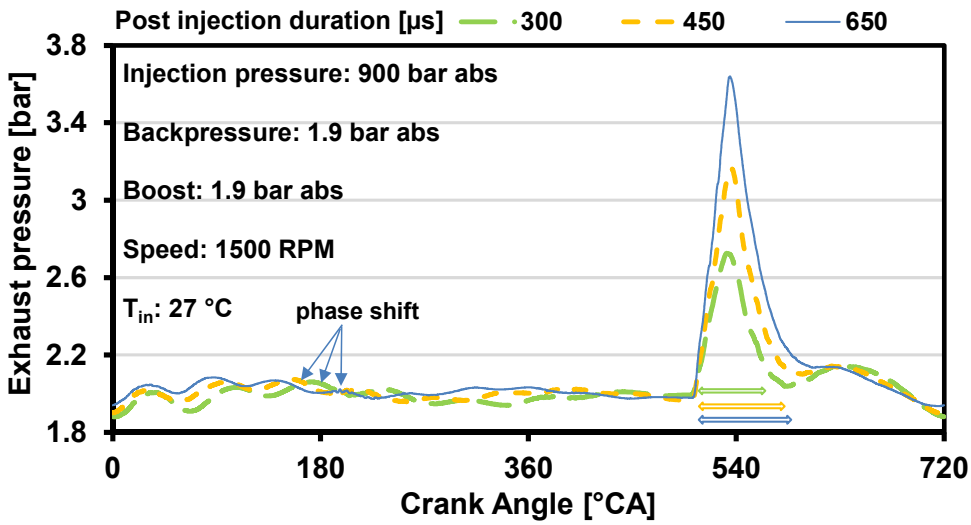

Figure 3-12. Exhaust pressure with different post injection durations

From the test results of different post injection strategies, it can be seen that when the post injection was applied, the exhaust pressure wave was significantly intensified. This can again be attributed to the ultimate consequence that p_{c_EVO} was increased.

3.1.4 Effect of EGR

Exhaust gas recirculation (EGR) is a strategy often used in internal combustion engines to reduce emissions. The application of EGR consists of recirculating part of the exhaust gas into the intake charge. As the CO_2 and H_2O concentrations are higher in the exhaust gas, the recirculated gas can effectively increase the specific heat capacity of the in-cylinder charge. In this way, the combustion temperature can be lowered. Meanwhile, the intake oxygen is diluted by the EGR. Under such circumstances, the propensity of NOx formation can be effectively reduced. As EGR is widely used on production engines, it is worthwhile to look into how the exhaust pressure wave changes at different EGR ratios. Here, EGR ratio is defined as the ratio between intake and exhaust CO_2 concentration:

$$EGR\% = \frac{Intake\ CO_2\ \ concentration\ by\ volume}{Exhaust\ CO_2\ \ concentration\ by\ volume} \qquad 3\text{-}1$$

To compare the effect of different EGR ratios, the parameters such as the IMEP, boost, and backpressure were all kept constant. The EGR ratio was adjusted by changing the EGR valve opening. The in-cylinder pressure and exhaust pressure were measured (Figure 3-13 and 3-14, respectively). With increased EGR ratio, more exhaust gas was

recirculated into the intake. The hotter exhaust gas increased the intake temperature slightly (about 25 °C). Yet, the temperature change was not significant enough to cause any substantial changes in the exhaust pressure. From the in-cylinder pressure profile, though the in-cylinder peak pressure was slightly affected by the recirculated gas, the pressure at EVO was similar. The exhaust pressure profiles at four different EGR levels were predominantly the same. This indicated that EGR did not have any major influence on the pressure wave action under the tested conditions.

It should be mentioned that the combustion phasing, boost pressure, and load level were set to the same in this comparison. EGR did not have any obvious effect on both in-cylinder pressure and exhaust pressure wave under such settings. However, in real world applications, the usage of EGR is often closely related with other engine operating parameters such as boost pressure, combustion phasing, injection pressure, and so forth. The comparison would be very complicated if all the parameters are taken into consideration. So, the purpose here is to show that as long as the in-cylinder pressure is not changed by EGR, it will not have any significant effect on the pressure wave action.

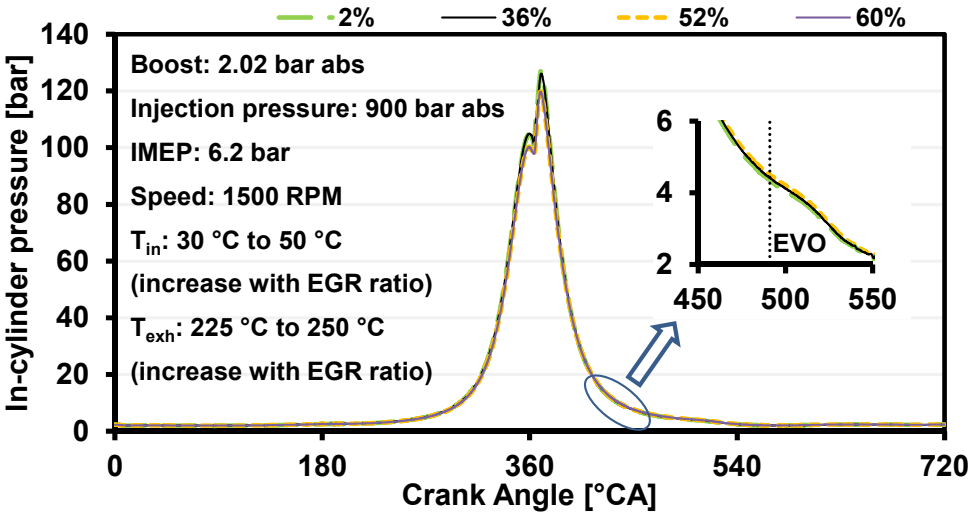

Figure 3-13. In-cylinder pressure with various EGR ratios

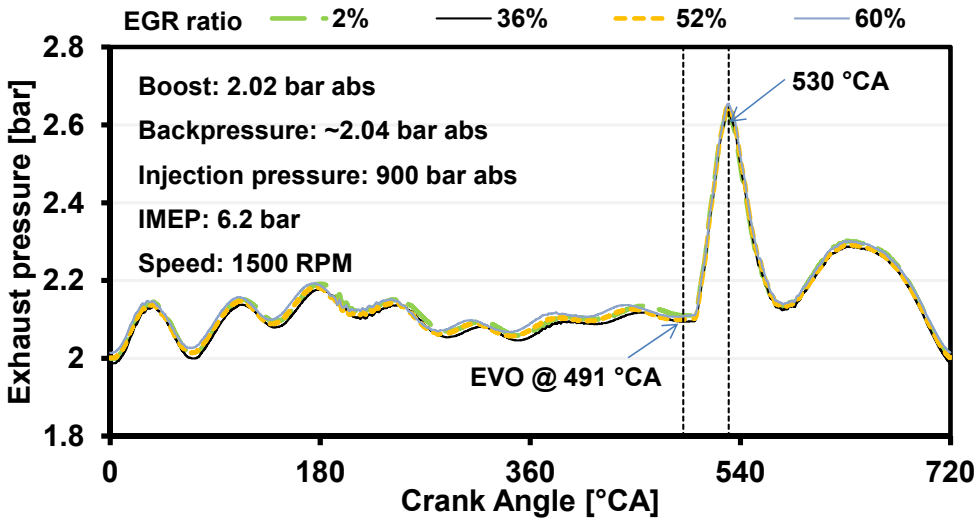

Figure 3-14. Exhaust pressure with various EGR ratios

3.1.5 Effect of backpressure

Backpressure in a production engine is caused by the resistance of the exhaust pipes and other components such as the turbocharger and the aftertreatment catalytic converters. Backpressure may change with engine operating conditions. For example, it will increase with elevated loading of a diesel particulate filter. In a turbocharged engine, backpressure changes with the turbine working conditions.

In this study, backpressure was adjusted by a backpressure valve fitted in the exhaust system. The in-cylinder conditions at EVO were similar while the backpressure was different. When the backpressure was higher, the pressure rise (p_{e_max}-p_e) in the exhaust pipe tended to be lower though the peak value was higher. The peak pressure rise reduced from 71% at 1.3 bar backpressure to 29% at 2.2 bar backpressure as illustrated in Figure 3-15. This meant that a high backpressure would actually suppress the compression wave from the cylinder. This was consistent with the relation between (p_{e_max}/p_e) and (p_{c_EVO}/p_e) shown in Figure 3-2.

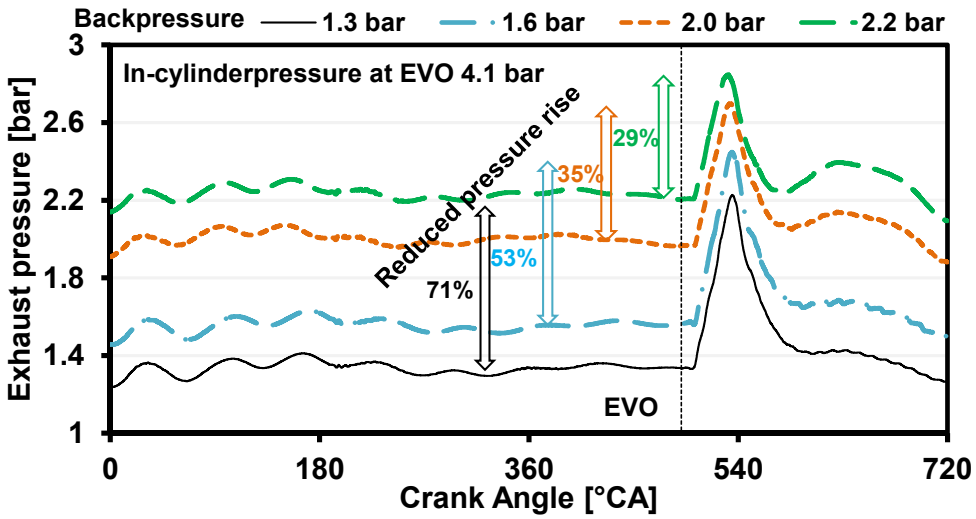

Figure 3-15. Exhaust pressure at various backpressures

3.1.6 Exhaust pressure wave at different measurement locations

The exhaust pressure at different locations is shown in this section (Figure 3-16) to illustrate the transmission and propagation of the pressure wave inside the exhaust system. Pressure measurements were made at 4 different locations as shown in Figure 2-2. Locations 1 and 2 were quite close to the exhaust flange (10 cm and 23 cm, respectively), location 3 was 3 cm before the DOC and location 4 was 2 cm after the DOC. It was found that the shapes of the pressure wave at locations 1 and 2 were quite similar, while the pressure profiles at locations 3 and 4 were significantly different from the first two. The blow down process produced a strong compression wave which was damped out when it travelled from location 1 to location 3. One of the main reasons was the flow restrictions at the two 90° elbows. It could also be affected by the change in the pipe diameter. The pressure curves at locations 3 and 4 were generally the same except with a slight phase shift.

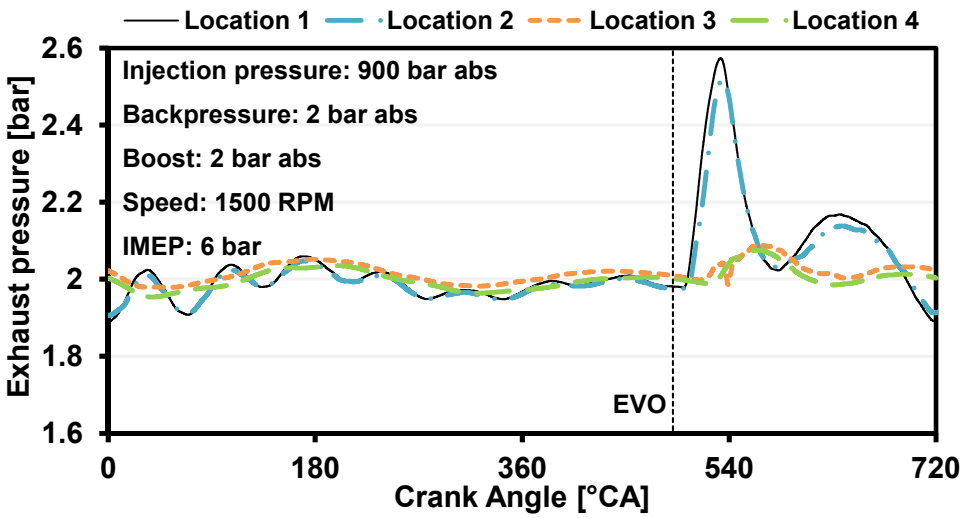

Figure 3-16. Exhaust pressure at different locations

3.1.7 Effect of exhaust runner length

To investigate the effect of the runner length on the pressure wave action, an exhaust pipe with a longer straight section was used to replace the original one. Here, runner length was defined as the length of the straight section of the exhaust pipe connected with the exhaust flange. The runner length of the original set up was 0.29 m and the modified one was 0.83 m as shown in Figure 2-2. The distance between the measuring position and the flange was 0.1 m in both cases. The engine was run at the same conditions in both configurations as indicated in Figure 3-17. The parameters such as IMEP, CA50, boost, and backpressure were all constant. The in-cylinder pressure at EVO was marginally higher (about 0.06 bar) with the longer runner. This difference could be caused by the uncertainty of the in-cylinder pressure measurement at this low pressure range. Moreover, as these two tests were conducted at different days, another possible reason for this difference was that the conditions of the intake air changed, such as air humidity and temperature. It was difficult to create exactly identical test conditions for two tests. During the valve open period (from EVO to EVC), the exhaust pressure had a similar trend for both the cases as shown in Figure 3-18. The phase of the first peak after EVO did not change with runner length. The peak value was marginally higher (0.08 bar) with the longer runner, which was probably because of the slightly higher in-cylinder pressure at EVO. The influence of the runner length on wave phase was observed when the exhaust valves were closed. This was related to the transmission of the pressure wave in

the exhaust pipe. It took more time for the pressure wave to travel through when the exhaust runner was longer. It should be noted that when the exhaust valves were open, though the effect of the runner length on the wave phase was not evident, it should still exist. This was probably due to the much stronger compression wave from the cylinder whose effect was more pronounced than the runner length.

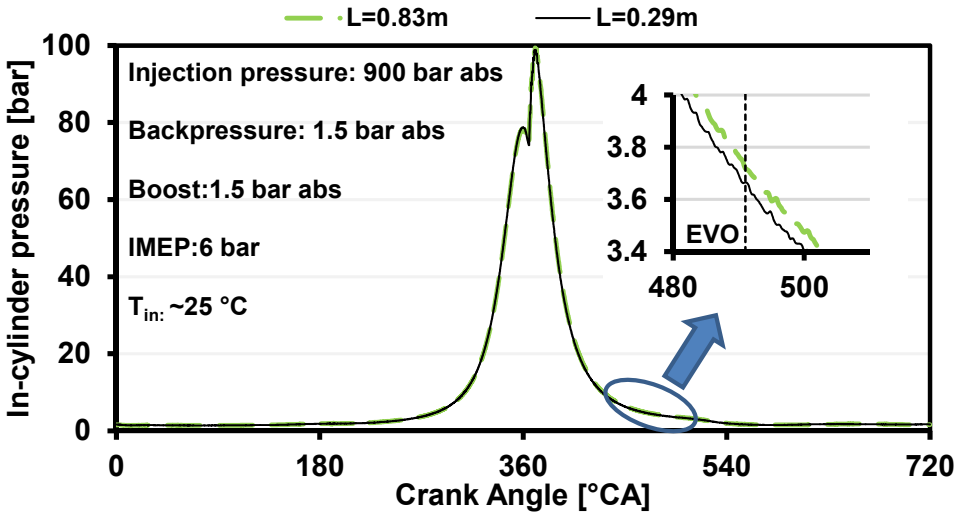

Figure 3-17. In-cylinder pressure with different runner lengths

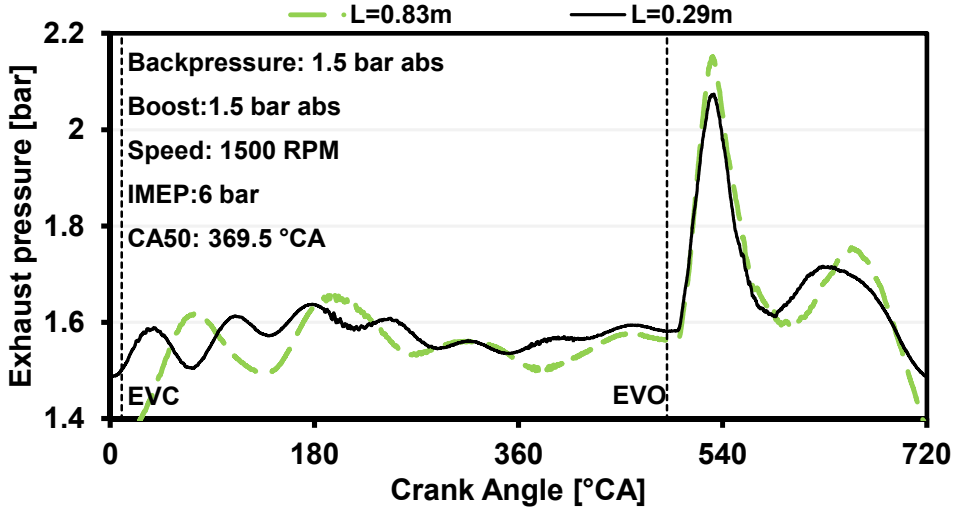

Figure 3-18. Exhaust pressure with different runner lengths

A second measuring point was used on the long runner to see how the pressure wave changed along the pipe. The second transducer was mounted 0.6 m away from the first one. The exhaust pressure was measured at these two positions as shown in Figure 3-19. A phase shift of the pressure wave was obvious; however, the shape was generally the

same. The amplitude of the peak pressure marginally decreased at the second measurement location. In Section 3.1.6 with the short runner setup, the distance between locations 1 and 3 was about 0.65 m, which was quite similar to the distance here, but the shape of the pressure wave was drastically changed. The material of the pipes used in the two cases was the same. So, the shape change of the pressure wave observed at location 3 on the short runner setup was mostly caused by the configuration of pipes rather than the total path length.

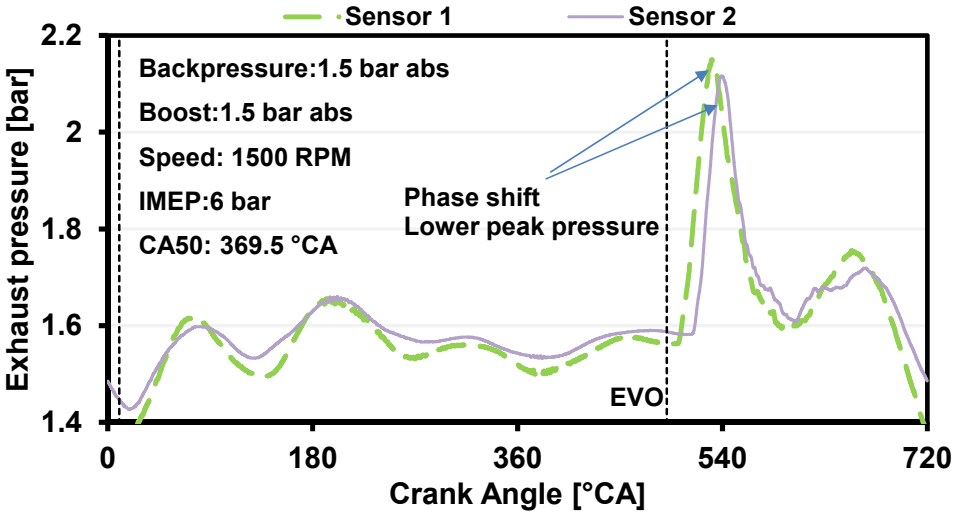

Figure 3-19. Exhaust pressure at different locations on the long runner

3.1.8 Summary of the empirical results

The test results illustrated the pressure wave action at various engine operation conditions such as load, backpressure, EGR, and post injections. A compression wave was generated after the opening of the exhaust valves. This wave was largely dependent on the in-cylinder condition, and the conditions in the exhaust pipe at this moment. A higher in-cylinder pressure tended to produce a stronger compression wave with both higher peak pressure and longer duration. Conversely, a higher backpressure suppressed this effect. The phase of this compression wave was largely independent of the engine running conditions as long as the valve timing was fixed. The peak exhaust pressure was observed at around 530 °CA in all the cases. However when the exhaust valves were closed, the phase of the pressure wave shifted with the change in temperature and runner length. From the results of pressure measurement at different locations, it was seen that the pipe configuration had a strong effect on the pressure wave transmission. Sharp angles in the

exhaust pipe could significantly damp out the pressure fluctuations. The DOC, on the other hand, seemed to have a limited effect on the pressure wave propagation.

The test results provided information on the exhaust pressure wave under different operating conditions. However, the velocity of the exhaust gas was difficult to measure under such conditions, so a simulation tool was employed to determine further details of the flow.

3.2 Simulation results

The 1-D simulation tool AVL BOOST was used for all the simulations. The first step of the simulation was validating the numerical model with experimental data. Then, the model was used to estimate the velocity which was difficult to measure. Furthermore, the model was used to simulate conditions that were not covered by experiments to provide a more comprehensive understanding of the exhaust pressure waves.

3.2.1 Model validation

To validate the simulation model, the engine geometric parameters and working conditions were set to be the same as the experiments. Since the exhaust pressure wave was the major focus of this research, in order to avoid discrepancies caused by simulating the in-cylinder combustion, the in-cylinder pressure data obtained from experiments was directly used in most of the exhaust pressure wave simulations as a boundary condition. For the simulations which did not have corresponding empirical results, the Vibe combustion model was used to simulate the in-cylinder combustion process.

Parameters such as the flow coefficients required in the simulation as input were difficult to measure. These coefficients were determined by trial-and-error. It should be mentioned that once these coefficients were determined, they became part of the model and were kept constant in all the simulations, unless there was a change in the physical setup, such as the runner length. For each simulation, only the boundary conditions and the initial conditions were changed.

First, simulation results of firing conditions with the short runner setup were compared with the experimental data as shown in Figure 3-20. Then, the model was used to simulate the condition when the engine was equipped with the longer runner. The simulation and test results are shown in Figure 3-21.

The simulation tool was able to capture the major features of the exhaust pressure wave, such as the peak pressure amplitude and phase. The maximum absolute difference of pressure within the whole cycle was less than 0.1 bar and the relative difference was less than 5%. Overall, the model was able to simulate the exhaust pressure wave accurately. Various conditions were simulated in the software to give detailed information about gas flow velocity of the exhaust.

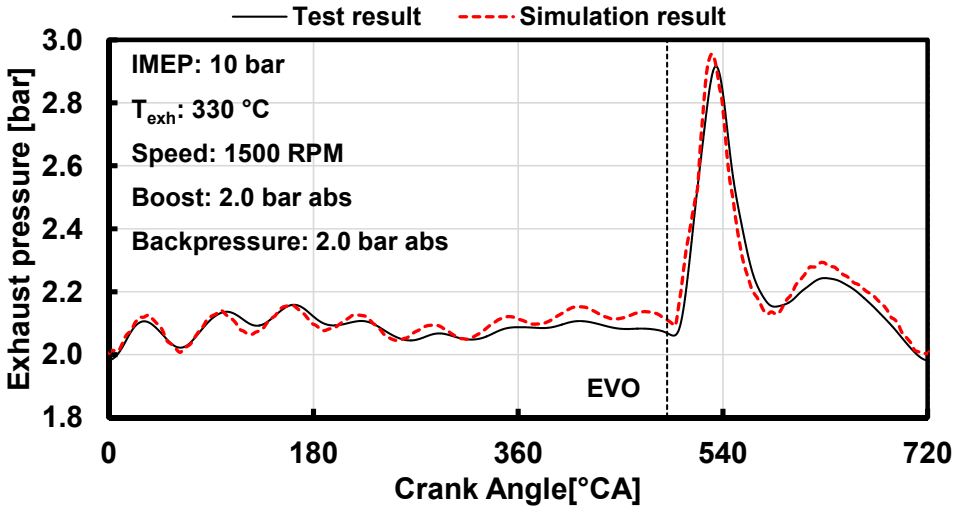

Figure 3-20. Test and simulation results of the exhaust pressure with the short runner

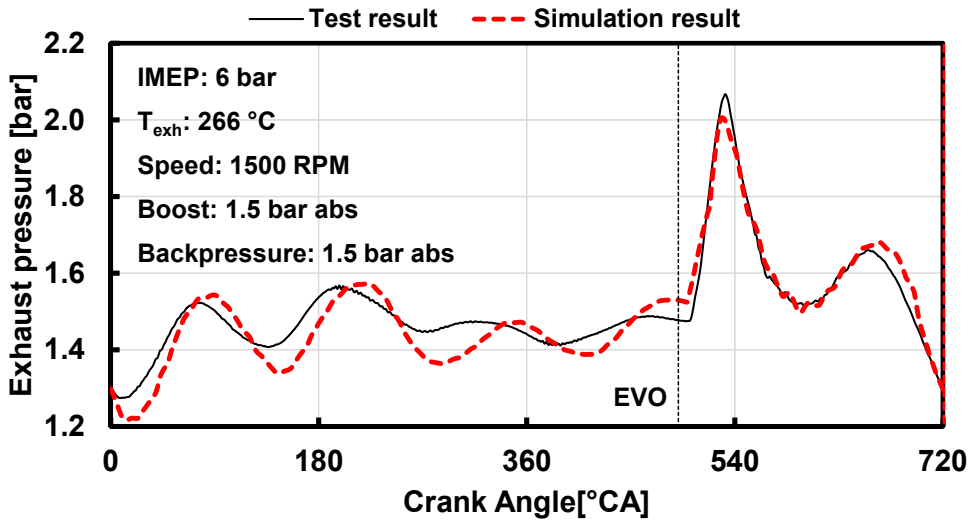

Figure 3-21. Test and simulation results of the exhaust pressure with the long runner

3.2.2 Velocity of exhaust gas flow

As discussed in Chapter 1, gas flow velocity can have a strong effect on the droplet breakup process. Therefore, an important objective of this research was to determine the gas flow velocity. With the AVL BOOST simulation tool, it was possible to calculate the gas flow velocity.

As illustrated in Figure 3-22, the gas flow velocity changes with the pressure wave. According to the orifice flow theory, the flow velocity at the throat of the valve is related to the upstream and downstream pressure ratio. When this ratio is higher than the critical pressure ratio, the flow can be sonic.

The measurement point for the simulation was at location 1 of the short runner as shown in Figure 2-2. When the exhaust valves opened, the gas flow velocity increased to a peak value of about 100 m/s in less than 40 °CA (around 5 ms at 1500 rpm). Then, following the pressure trace, the velocity decreased to less than 20 m/s until it increased back to 80 m/s during the displacement process. The phase of the velocity was approximately the same as the pressure. The peak value of the velocity appeared around the same time as the peak pressure.

From the simulation results, it was evident that the velocity of the gas flow out of the cylinder was not uniform. The flow velocity was high when the exhaust valves were open, especially during the blow down process. When the valves were closed, there were only minor fluctuations.

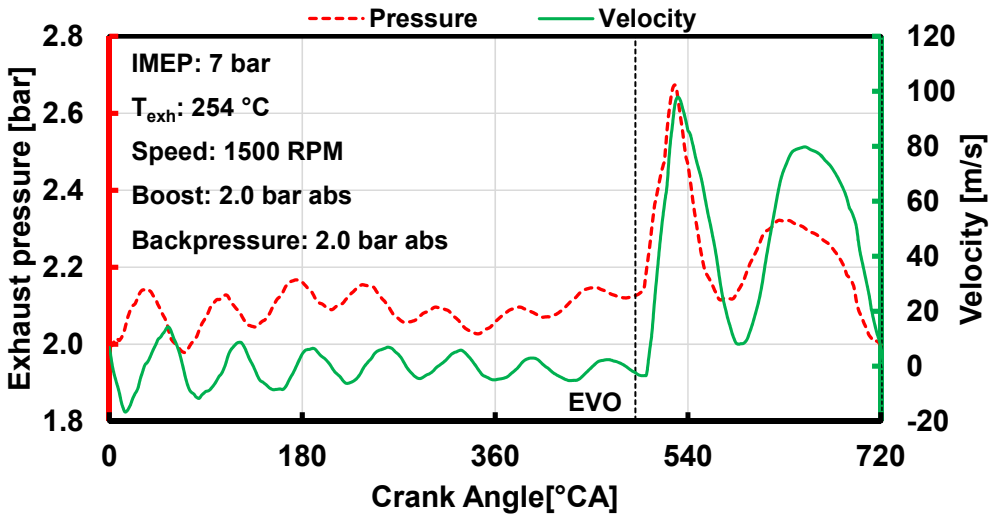

Figure 3-22. Exhaust pressure and gas flow velocity (with the short runner)

3.2.2.1 Exhaust gas flow velocity under different load levels

The simulation tool was then used to investigate the change of the exhaust gas velocity for different exhaust pressure waves. Since empirical velocity data was not available, the pressure data was compared with the experimental results to verify the simulation model. If the simulated exhaust pressure data could match the measurement results, it was expected that the velocity data will be a fairly accurate representation of the real condition. The exhaust pressure data at two different loads were compared as shown in Figure 3-23 and Figure 3-24. In both cases, the physical model was the same. Boundary and initial conditions such as temperature, and boost pressure were set according to the different engine running conditions. The simulated exhaust pressure matched well with the experimental data for all the cases. This again reinforced the validity of the simulation model.

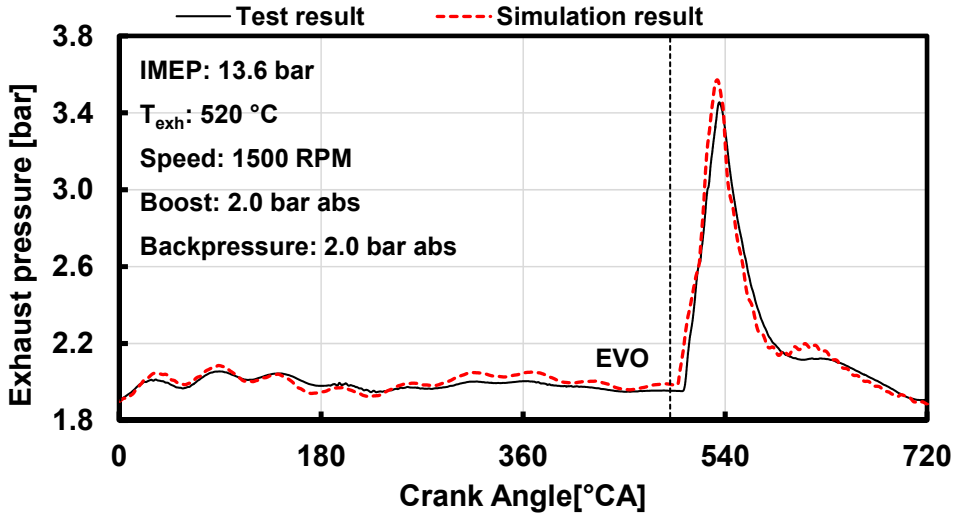

Figure 3-23. Simulated and measured exhaust pressure at 13.6 bar IMEP

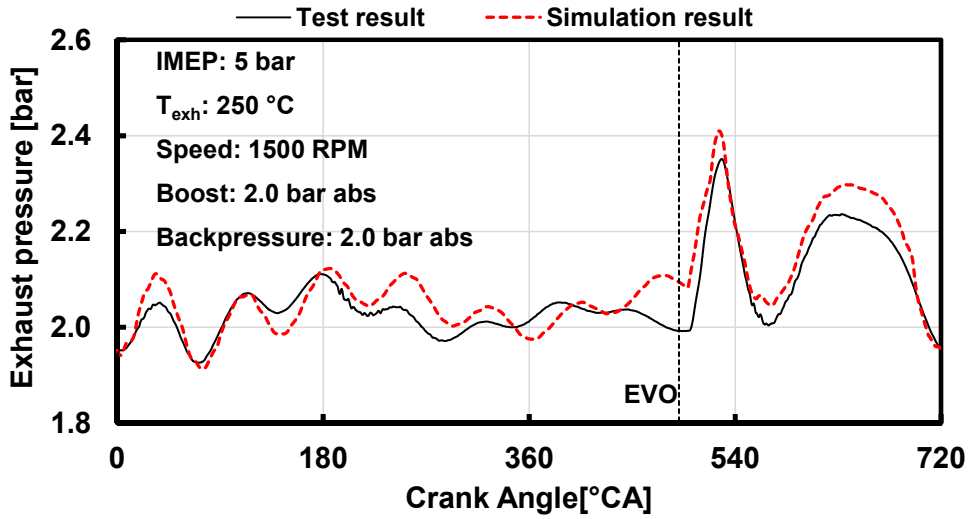

Figure 3-24. Simulated and measured exhaust pressure at 5 bar IMEP

The velocity of the exhaust flow under three different load levels – 10, 13.6, and 5 bar was compared (Figure 3-25). The corresponding exhaust pressure profiles are shown in Figure 3-20, Figure 3-23 and Figure 3-24, respectively.

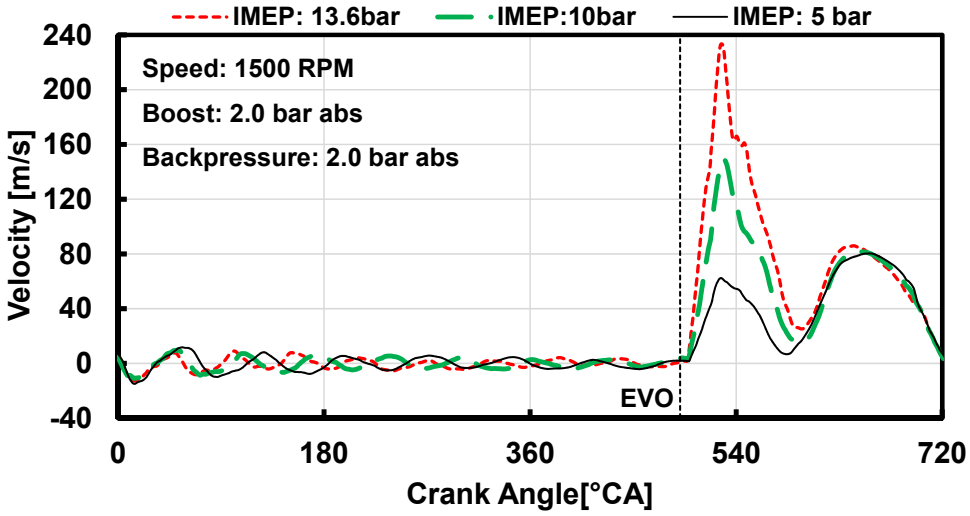

Figure 3-25. Exhaust flow velocity at various load levels

Here, the comparison was made when the boost pressure and the backpressure were the same. As the exhaust pressure wave became stronger with increased load, the exhaust flow velocity also increased. At 13.6 bar IMEP, the instantaneous flow velocity was as high as 220 m/s. It should be noted that during the displacement process, the velocity at three different loads was almost the same (the peak velocity was about 80 m/s). The same trend was also observed in the pressure trace. Since the displacement process was mainly

affected by the piston movement, the gas velocity did not change when the engine speeds were the same.

Based on these simulation results, the gas flow velocity increased with the rising strength of the exhaust pressure wave. In the case of high load or post injection, when the exhaust pressure wave was quite strong, the gas velocity could be expected to be very high.

3.2.2.2 Exhaust gas flow velocity at different locations

The pressure and gas flow velocity at different locations are important in a production engine since the aftertreatment injector may be mounted at different locations. The wave effect may be strong at one location but quite weak at another location. Previous test results have shown that the pressure wave is largely damped out after several elbows. So in this subsection, the velocity information at different locations is discussed.

The test and simulation results of exhaust pressure at four different locations (Figure 2-2) are shown in Figure 3-26 and Figure 3-27, respectively. The simulation results match well with the experimental results at the four different locations.

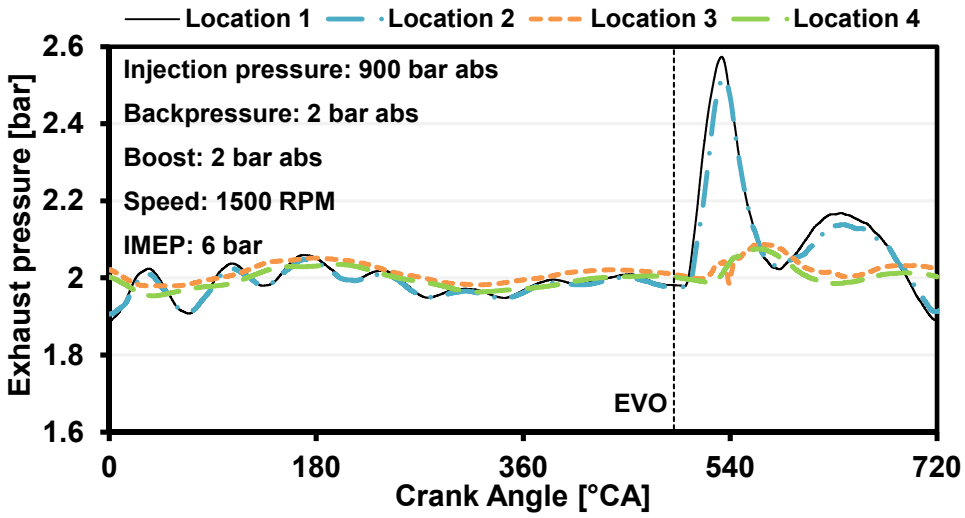

Figure 3-26. Test results of exhaust pressure at different locations

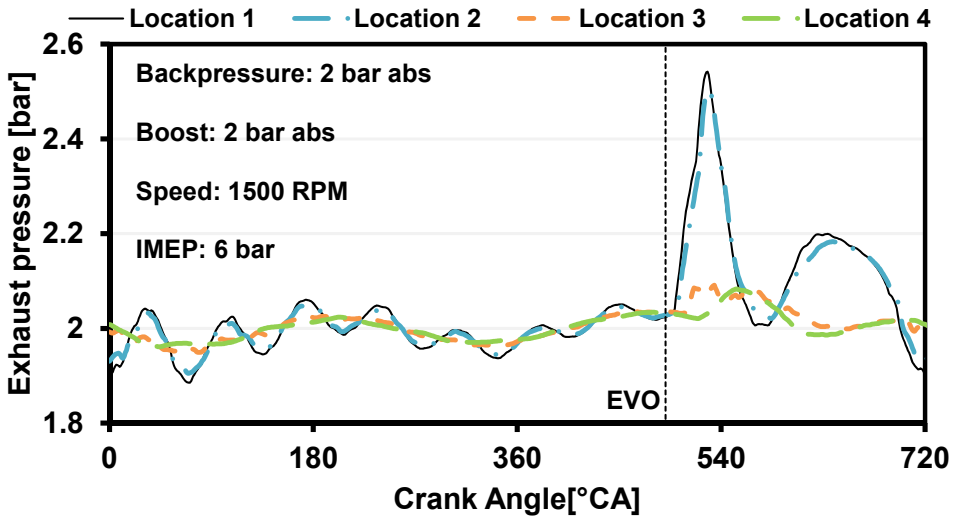

Figure 3-27. Simulation results of exhaust pressure at different locations

The simulated exhaust gas flow velocity is shown in Figure 3-28. It can be seen that at locations 1 and 2, the gas flow velocities were similar, while at location 3, the velocity magnitude decreased during the whole cycle. This was due to the restriction of the pipe elbows. Further downstream at location 4, the gas flow velocity no longer followed the typical feature seen during the blow down and displacement processes. Though the pressure curves at locations 3 and 4 were similar, the flow velocities were significantly different. The velocity at location 4 fluctuated during the cycle. The DOC (represented by an AVL BOOST model) between locations 3 and 4 might have changed the flow pattern in the pipe. From the simulation results, it was predicted that downstream of the exhaust pipe, where the exhaust pressure wave decreased in magnitude, the exhaust gas flow velocity also reduced. Consequently, if the aftertreatment injectors were placed quite far away from the exhaust valves, the effect of the pressure wave could be limited.

It is necessary to emphasize that the pressure wave transmission is also dependent on the pipe configuration in the exhaust system. If a straight section is used, the exhaust pressure wave effect can be stronger. By using a large number of elbows or diverging sections, the effect can be damped out.

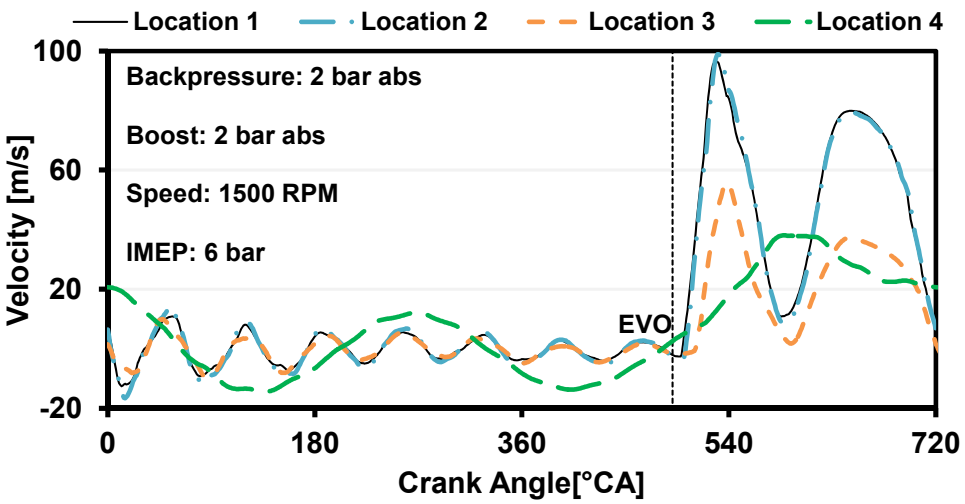

Figure 3-28. Simulation results of exhaust gas flow velocity at different locations

3.2.3 Effect of exhaust runner diameter

The exhaust pipe diameter was another parameter considered in this research. In a production engine system, the design of the exhaust pipe diameter depends on achieving a balance between parameters such as backpressure and gas flow velocity.

For simplifying the analysis, the backpressure was fixed and the simulation tool was used to see how the pressure wave and the gas flow velocity change with the pipe diameter. Here, the exhaust pipe diameter was set to be 25.4 mm (1 inch), 38.1 mm (1.5 inches) and 50.8 mm (2 inches) , respectively. The intake system and the in-cylinder combustion conditions were all the same in the three cases. The load level was kept at 11.2 bar IMEP, the boost and the backpressure were fixed at 2 bar. From the simulation calculation, it was found that as the exhaust pipe diameter increased, the exhaust peak pressure and peak velocity decreased as shown in Figure 3-29 and Figure 3-30, respectively. Overall, the peak exhaust gas flow velocity decreased by more than 50% and the exhaust peak pressure decreased by approximately 10% when the exhaust pipe diameter increased from 25.4 mm (1 inch) to 50.8 mm (2 inches). A phase shift was also observed when the exhaust valves were closed. The gas flow velocity during the displacement process also decreased with the increase in pipe diameter.

Though the in-cylinder conditions and the backpressure in the three simulations were the same, the peak exhaust pressure was quite different. This observation was not consistent with the trend illustrated in Figure 3-2. It was evident from this set of results that the peak

exhaust pressure was not only affected by the in-cylinder pressure at EVO and the exhaust backpressure, but also influenced by the exhaust diameter. Since the intake system and boost pressure were constant in the three simulations, the mass of the exhaust gas was the same. When the diameter of the exhaust pipe increased, the flow sectional area increased. The pressure and the velocity dropped subsequently.

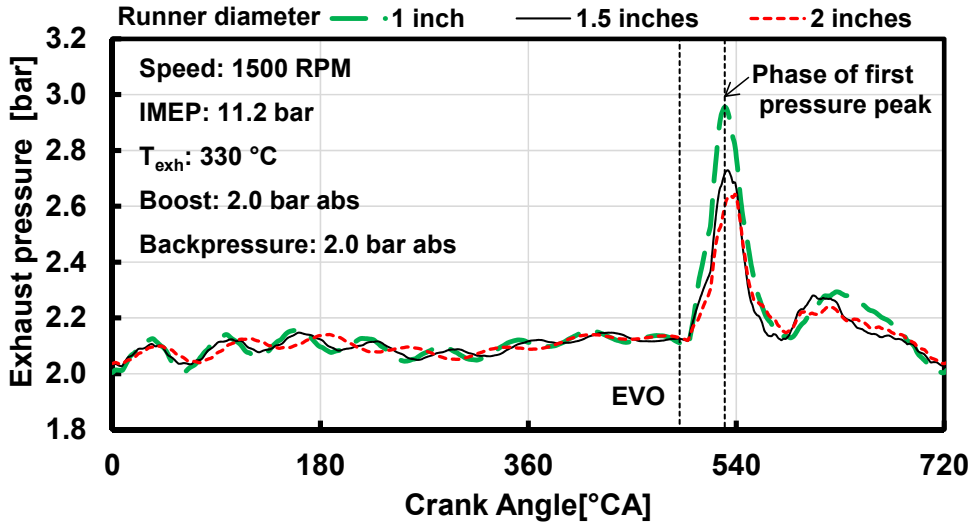

Figure 3-29. Exhaust pressure wave with changed exhaust runner diameters

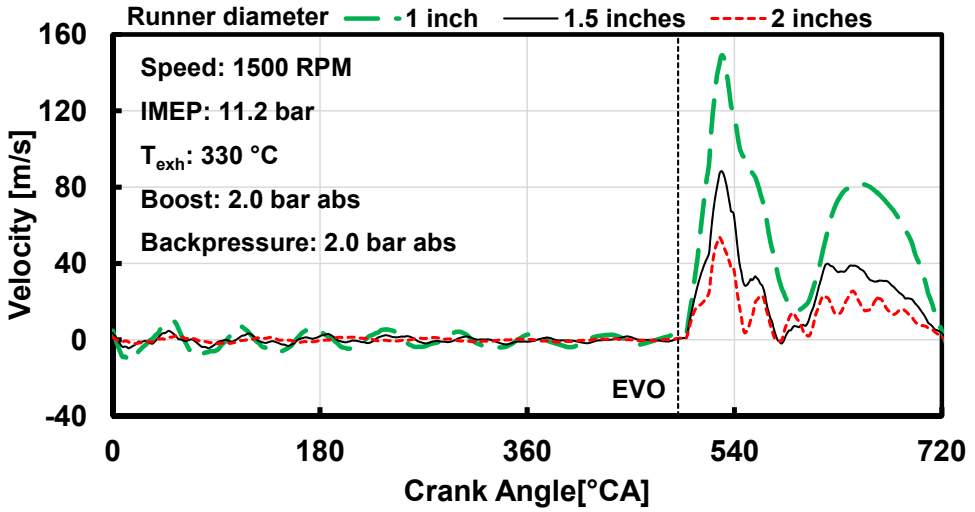

Figure 3-30. Exhaust flow velocity with changed exhaust runner diameters

3.2.4 Exhaust pressure wave in a multi-cylinder system

The previous test and simulation results were all based on the single cylinder research engine. However, most of the modern passenger and commercial vehicles use multi-

cylinder engines. This section shows the simulation results of exhaust pressure wave in a 4-cylinder engine.

The configuration of the engine system is shown in Figure 3-31. The geometry of the simulation model was similar to the previous short runner set up as shown in Figure 2-2 except that the single cylinder was replaced by 4 identical cylinders. The engine load was set to 7.9 bar IMEP. The measurement point in the simulation was chosen on the exhaust pipe just after the four exhaust runners joined together.

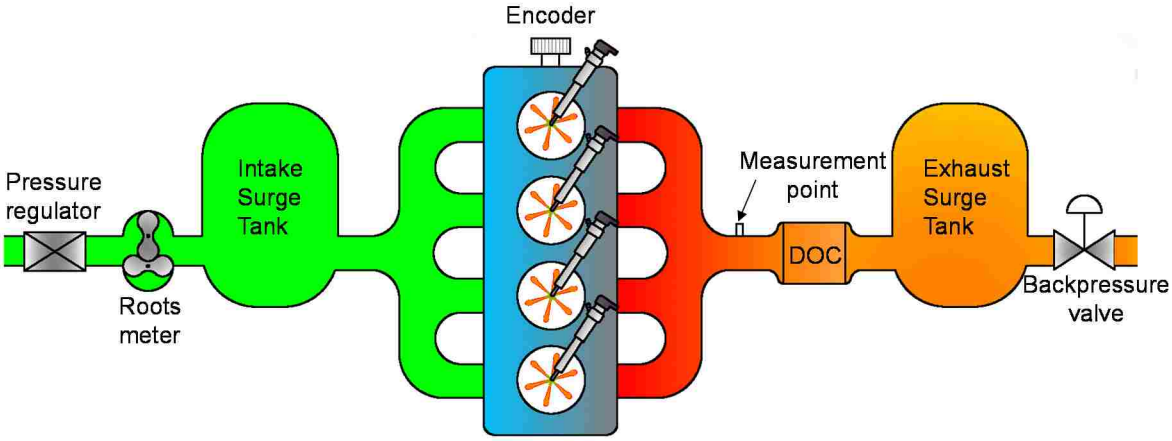

Figure 3-31. Schematic of a multi-cylinder simulation

Unlike the single cylinder case, the exhaust pressure wave with multi cylinders had multiple pulses as shown in Figure 3-32. The combustion in four cylinders produced four significant exhaust compression waves within one cycle. So, in a multi-cylinder engine, the pressure wave action could be more severe compared to a single cylinder case. Since the parameters in the four cylinders were the same and the four runners were symmetrically arranged, the amplitude and the shape of pressure wave from each cylinder were similar.

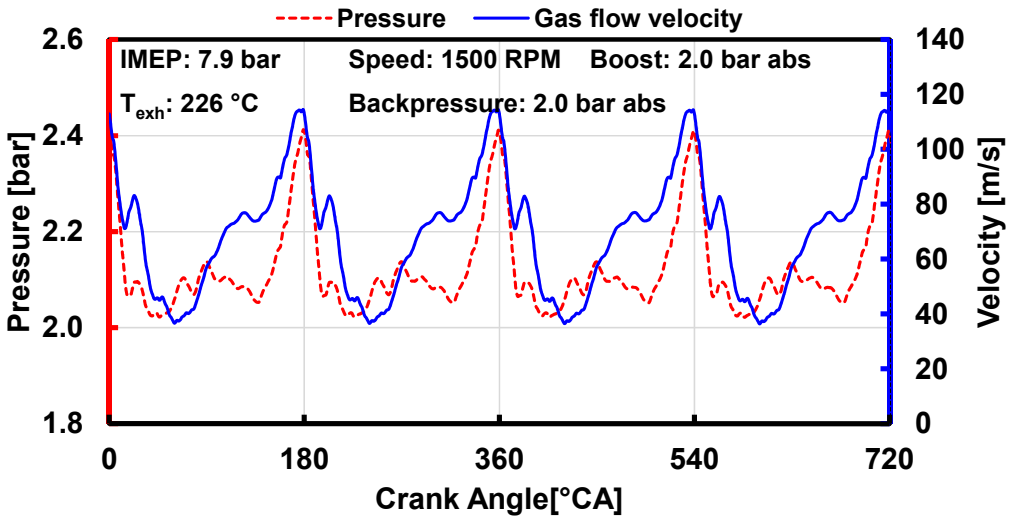

Figure 3-32. Exhaust pressure and gas flow velocity with multi-cylinder set up

3.2.5 Summary of the simulation results

The simulation results showed that the gas flow velocity in the exhaust pipe was not uniform. The fluctuations of the gas velocity followed a trend similar to the pressure wave. During the blow down process, the gas velocity was very high, yet when the exhaust valves were closed, the velocity was quite low and fluctuated continuously. Like the pressure wave action, the exhaust gas flow velocity was also different at different locations. In general, the pressure and the velocity changed drastically when the shape of the pipe was changed. For instance, the amplitude of the pressure wave and the gas flow velocity reduced significantly after pipe elbows, and the pressure profile no longer followed the same shape. Section 3.2.4 showed the pressure wave in a multi-cylinder engine. The pressure waves released from multiple cylinders were predicted to create a more unstable condition in the exhaust pipe with multiple pulses.

CHAPTER 4 SHOCK TUBE TEST RESULTS

This chapter describes the tests undertaken on a shock tube setup. First, the pressure profile of a shock wave is compared with an exhaust pressure wave. The results of the shock wave speed and the gas flow velocity at the open end of the shock tube are also described. Next, the interaction of the shock wave with a single droplet are shown to illustrate the detailed droplet breakup process. The last section is the demonstration of the shock wave effect on the aftertreatment spray.

4.1 Shock wave speed and gas flow velocity at the open end of the shock tube

The change of the exhaust pressure wave is much smoother compared to the shock wave. Unlike a shock wave, an exhaust pressure wave is generated by the process of gradual valve and piston movement. In this way, the exhaust pressure wave is not as sharp as a shock wave. Yet, as the exhaust pressure wave is very strong, its rising edge is quite steep. A comparison of an exhaust pressure wave and a shock wave from an open end shock tube is shown in Figure 4-1. In both cases, there is a strong compression wave followed by weak reflected waves. Moreover, both of them are accompanied by a fast gas flow behind the strong pressure wave. With these similar features, it is reasonable to simulate the exhaust pressure wave effect with a shock tube for this research. Many researchers have treated exhaust pressure wave as a weak shock wave in the past [29,49] and reported reasonable results.

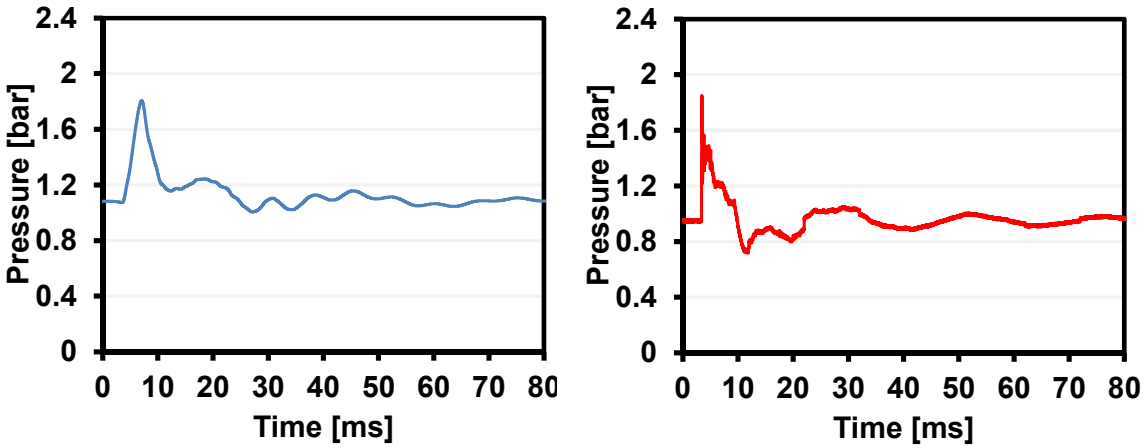

(a) Exhaust pressure wave (b) Shock wave

Figure 4-1. Comparison of exhaust pressure wave and shock wave

The major purpose of the shock tube tests is to create conditions similar to the exhaust pipe. However, the environment in the exhaust pipe is quite complicated. The pressure and temperature at different conditions may have large variations. In this research, it is not feasible to simulate all the possible conditions with the shock tube test set up. The focus here is to create some typical comparable conditions. As the study of temperature was outside the scope of this research, the other major parameters are pressure and velocity which are investigated by the author.

The burst pressure of the shock tube tests rangd from 1.8 bar to 4.5 bar, and created shock waves with peak pressures between 1.3 bar to 2.2 bar. The gas flow velocity changed from 70 m/s to 170 m/s with increasing burst pressure. Burst pressure beyond this range was not attempted due to safety concerns.

First, the shock wave speed from the shock tube test was compared with the theoretical results. The theoretical results were calculated from the equations described in Appendix B. The shadowgraph images were used to estimate the wave speed and the gas flow velocity in the shock tube tests. As shown in Figure 4-2, the shock front emerged from the shock tube first, followed by the gas flow. A ring type structure was observed at this moment. This phenomenon had been reported by several researchers [66–68]. The ring was mainly caused by the velocity difference between the gas flow out of the tube and the nearly quiescent ambient air. By analyzing the images that were taken at different time intervals, both the instantaneous wave speed and gas flow velocity were estimated. The measurements were taken along the central line of the shock tube as shown in Figure 4-2.

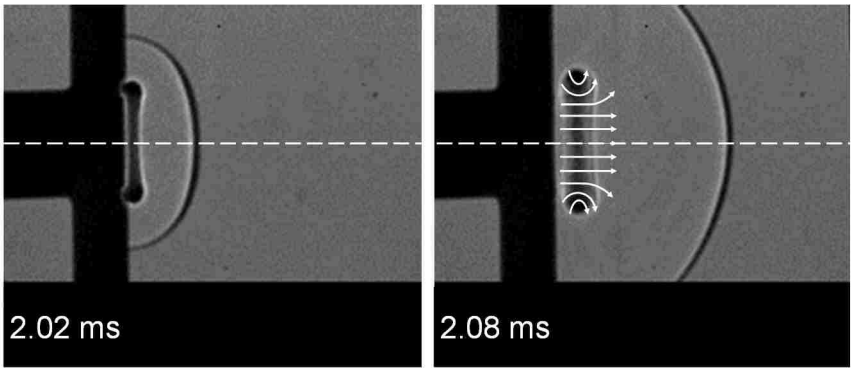

Figure 4-2. Shadowgraph images of the shock wave and the gas flow

Arakeri et al. used the PIV method to investigate the velocity of the vortex ring and the jet flow after the ring [68]. Their research results showed that the gas flow remained parallel

to the tube axis in the central portion of the vortex ring, whereas it curved at the edges as shown by the arrows in Figure 4-2. The velocity of the jet flow behind the vortex ring was nearly uniform from their PIV results.

If the vortex ring effect was taken into consideration, it did not make the current setup a perfect simulation of the exhaust gas flow. However, the vortex regions were limited to a small part of the gas flow, while the center region as well as the jet flow after the vortex ring were mostly uniform axial flow. Moreover, such sudden expansion configurations could also be encountered in an engine exhaust system, like the connection between the exhaust pipe and a catalytic convertor. So, it was still reasonable to use this configuration in this research. It should be emphasized that the main focus was on the effect of the pressure wave as well as the overall gas flow velocity instead of the detailed flow structure.

The instantaneous wave speed and gas flow velocity acquired from the shadowgraph photos under different burst pressures are shown in Figure 4-3 and Figure 4-4, respectively. The dashed lines in the figures were the theoretical wave speed and gas flow velocity from calculation according to the shock tube theory (Appendix B). From Figure 4-3, it was seen that the shock wave speed was quite close to the calculated speed when it just left the open end of the tube, and this value was verified by the pressure measurement from the two pressure sensors. Then the speed decreased, and subsequently stabilized at a lower value. The time in the figures was the elapsed time after the pressure trigger signal. At a higher pressure ratio, with a faster wave speed, the shock front was detected earlier. The time was gradually postponed with decreasing pressure ratio. Eventually, the wave front travelled out of the view of the camera frame and the wave speed could not be determined thereafter.

The values of gas flow velocity shown in Figure 4-4 gave a general idea about the velocity magnitude behind the shock wave. The initial gas flow velocity at the open end of the shock tube was lower than the theoretical value, but this value increased with time. The trend of the velocity change was similar to the results obtained by Arakeri et al. in [68]. Their results showed that when the gas flowed out of the shock tube, the velocity increased initially and then decreased after a certain period of time. The results in Figure 4-4 only showed the increasing trend because of the limited recording time.

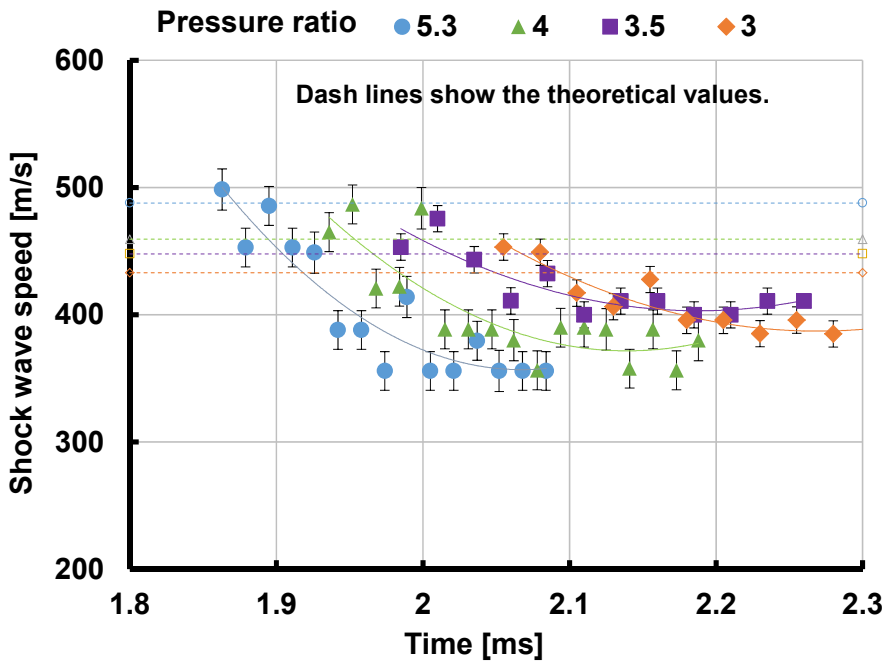

Figure 4-3. Shock wave speed at the open end of the shock tube

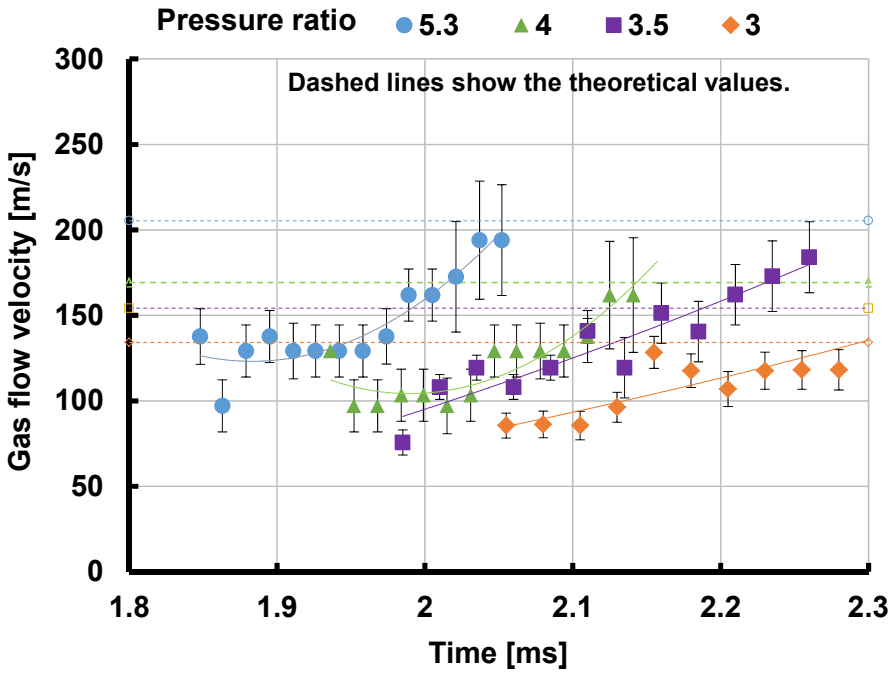

Figure 4-4. Gas flow velocity at the open end of the shock tube

The error bars in the figure indicated the uncertainty of the velocity measurement. The velocity was calculated from the movement of the shock front and the vortex ring in consecutive images captured by the high speed camera. A reference scale (such as the

tube diameter) was used to calibrate the image dimensions. Then, by counting the pixels, the distance between shock waves in different images was measured and the shock wave speed was estimated. The uncertainty of this calculation mainly came from the detection of the tracing point. Ideally the velocity should be calculated by measuring the movement of the same object. Here, the shock front had a relatively sharp edge with only one to two pixel variations. So the uncertainty was generally lower in the shock wave speed estimation. The gas flow velocity measurement was determined by tracing the edge of the vortex ring which was initially sharp but it blurred after a while, and the uncertainty increased significantly. Moreover, the burst pressure of the diaphragms used in these tests was not very consistent, and it was difficult to repeat the tests under exactly the same condition. The poor repeatability also increased the uncertainty. However, this part of the uncertainty was difficult to quantify. The purpose for showing the two velocity diagrams here was to give a general idea about the trend and the overall amplitude of the velocity.

4.2 Results of a single droplet breakup

A single droplet was used to investigate the effect of the pressure wave on the breakup process. The droplet was suspended at the end of the shock tube with a stainless steel capillary needle. The outer diameter of the needle was 0.6 mm. The diameter of the droplet was approximately 1.5 mm. With the shadowgraph image, it was possible to see whether the shock wave itself had any influence on the droplet breakup process. In order to differentiate the effect of the shock wave from the effect of the gas flow, the needle was put about 80 mm away from the tube end. In this way, the time for the wave arrival and the time for the gas arrival were easily distinguishable. The pressure ratio for these tests was 3.8. The initial pressure in the driven section was 1 bar absolute and the measured peak pressure value of the shock wave was about 1.8 bar. This value decreased to about 1.7 bar when it travelled to the end of the tube. As shown in Figure 4-5, the droplet was unchanged after the shock front passed by at 2.2 ms, then at 2.8 ms, the gas flow arrived at the droplet location and it broke up the droplet immediately. From this test result, the shock wave itself seemed to have minimal influence on the droplet, while the following gas flow had a significant impact on the droplet breakup.

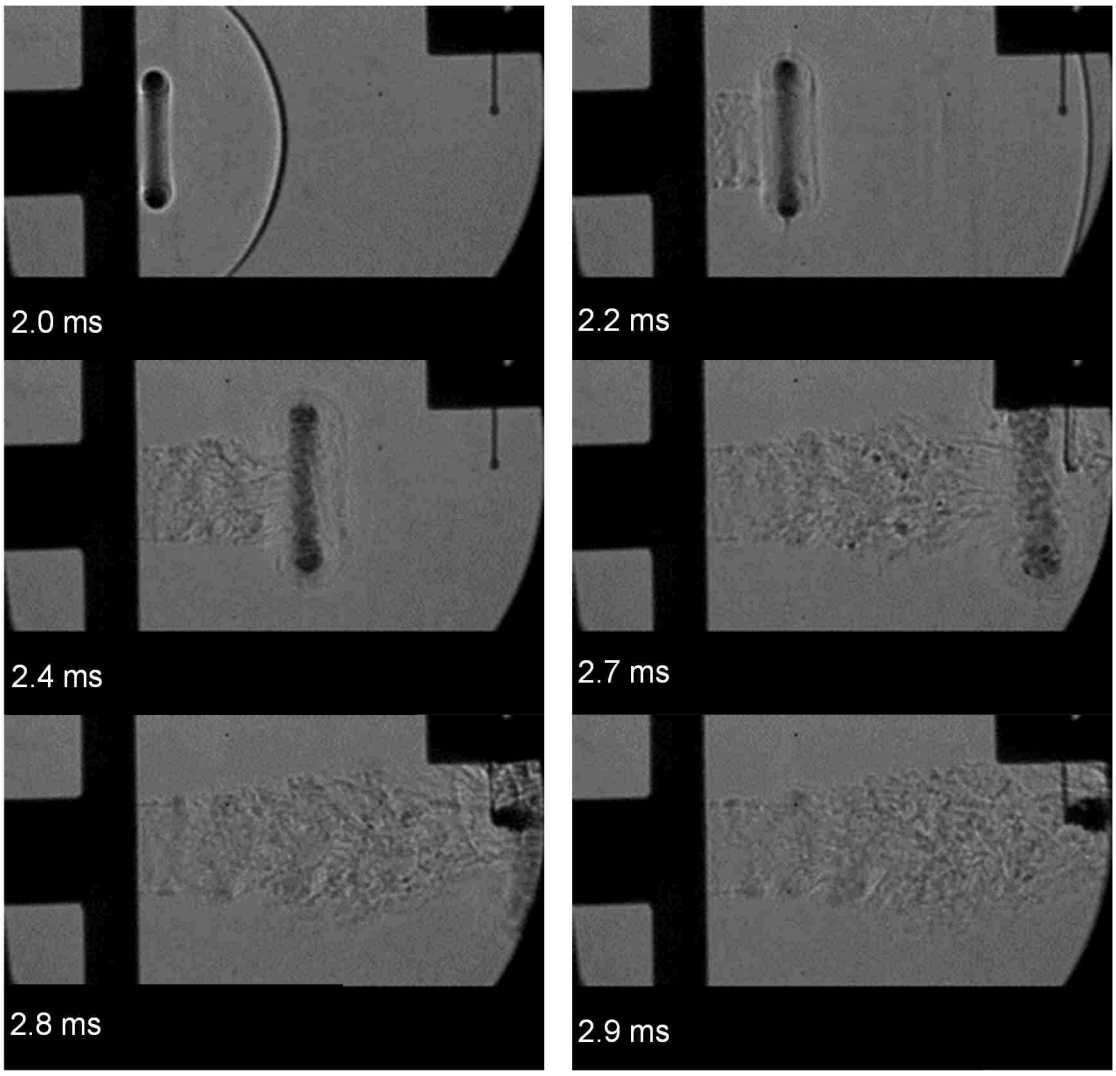

Figure 4-5. Effect of shock front and gas flow on the droplet breakup

Then different kinds of fluids were tested to see if the fluid properties had any relation to the breakup process. Three different kinds of droplets (water, diesel and 99% ethanol, respectively) were tried out under a similar pressure ratio (about 3.8). The shock wave pressure was about 1.7 bar and the gas flow velocity peaked at about 150 m/s under this condition. This condition was chosen because the maximum transient gas flow velocity at medium IMEP was approximately in this range (refer to Figure 3-25). The properties of the different fluids are listed in Table 4-1.

Table 4-1. Property of different fluids (at room temperature and ambient pressure)

Property	Diesel	Ethanol	Water
Viscosity [N·s/m^2]	0.002	0.00108	0.0009
Surface tension [N/s]	23.8	22.39	72.8
Density [kg/m^3]	820	789	997

Figure 4-6 to Figure 4-8 show the breakup process of the three fluids. The droplet was suspended at about 3 cm away from the open end of the tube. The shock wave front exited the tube at about 2 ms after the trigger signal, and passed through the droplet. The droplet structure remained unchanged until the gas flow arrived. With the high speed gas flow, the droplet broke up and drifted away. It was found that the high speed jet flow after the vortex ring continuously accelerated the breakup process. There were no significant differences in the breakup process between the three kinds of fluids under the given test conditions. The whole breakup process was completed within 2 ms after the start of the breakup. According to the breakup theory introduced in Chapter 1, the Ohnesorge number under this condition was quite low, smaller than 0.1 in all the three cases, which meant that the viscosity was not an important factor. So, the breakup process was mainly dependent on the Weber number, which was very high (larger than 500) in all the three cases because of the high flow velocity.

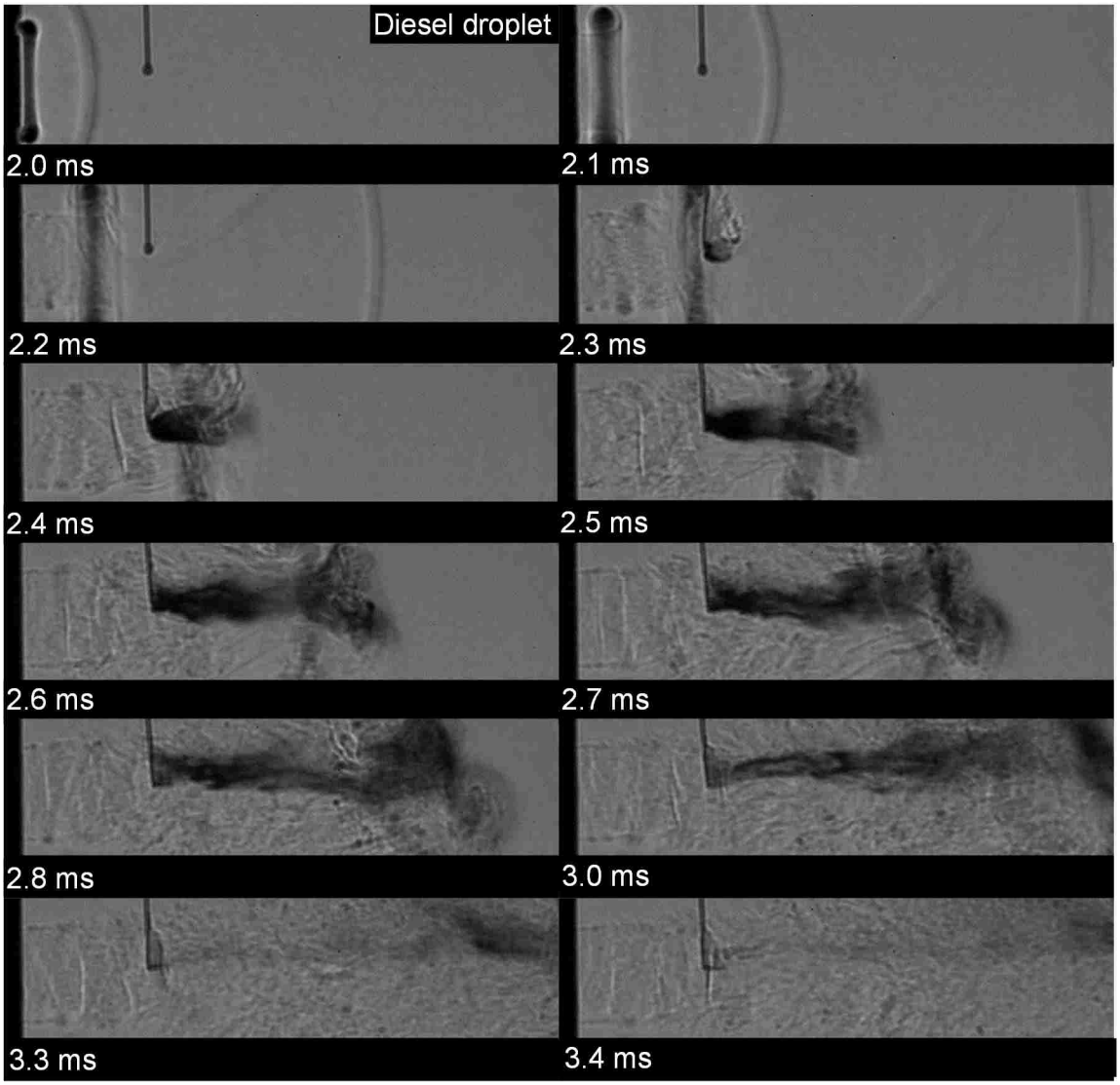

Figure 4-6. Breakup process of diesel droplet in the shock tube test

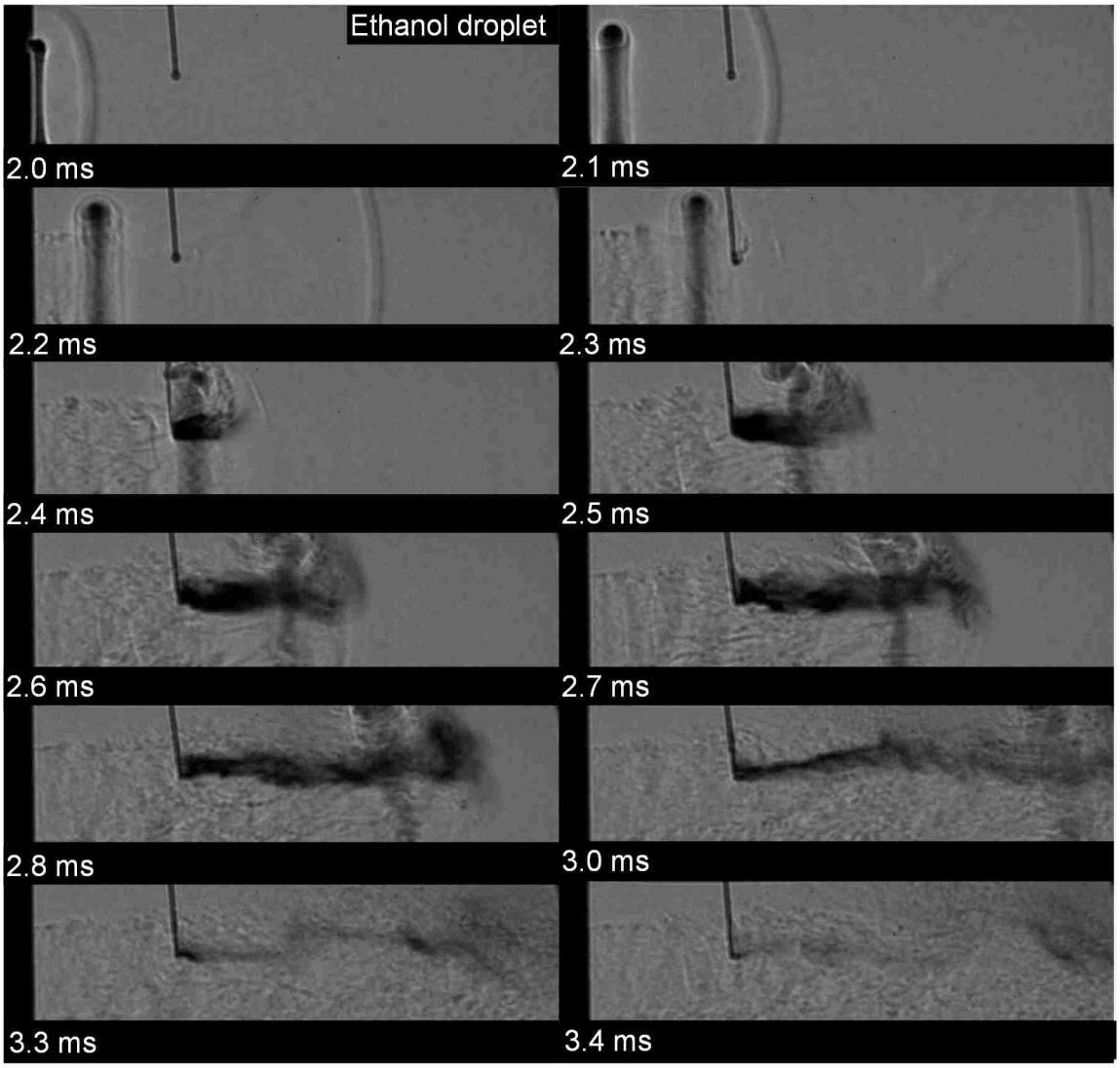

Figure 4-7. Breakup process of ethanol droplet in the shock tube test

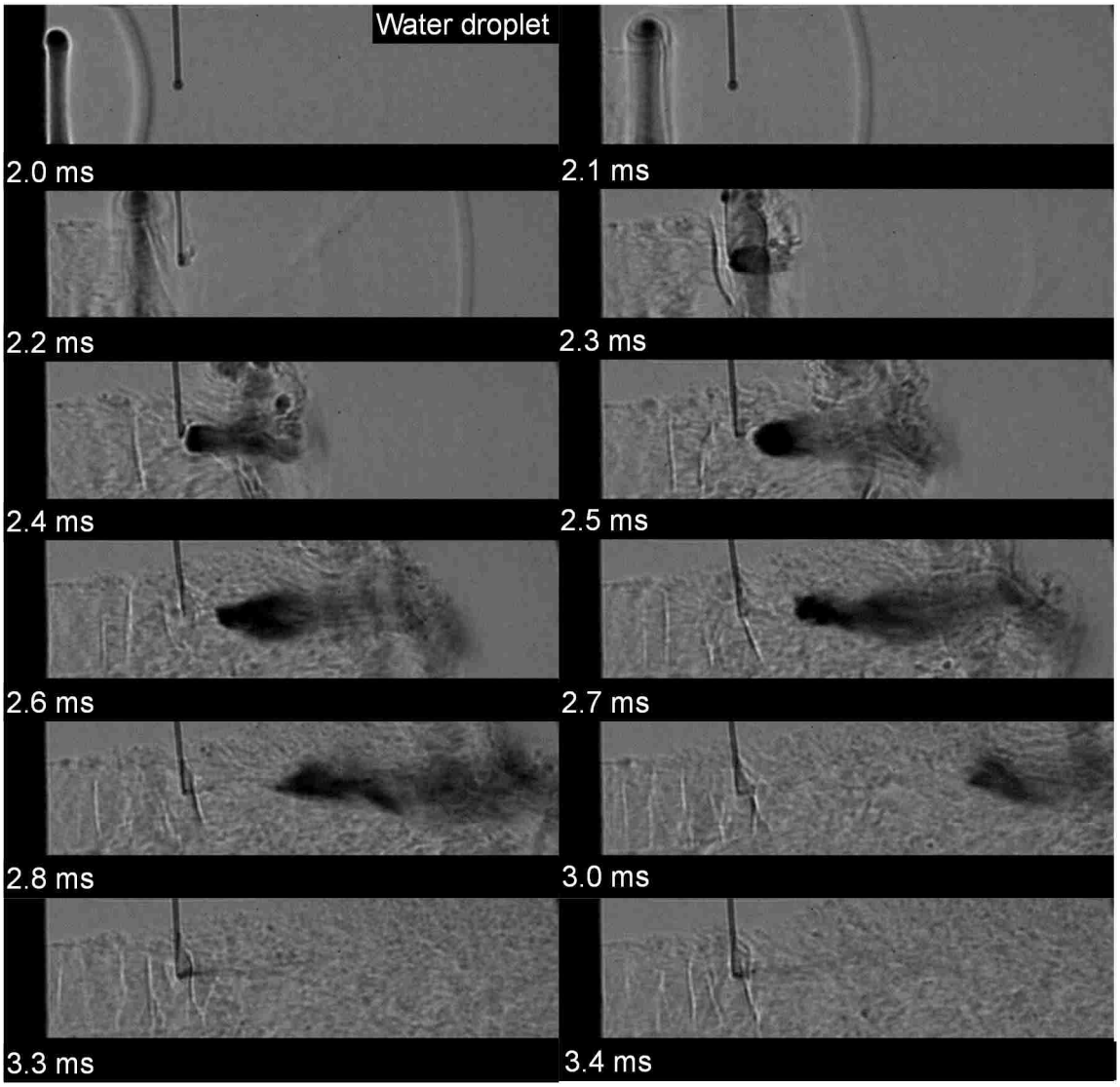

Figure 4-8. Breakup process of water droplet in the shock tube test

4.3 Results of spray breakup

For the spray tests, deionized water was used as the injected fluid. Diesel fuel and urea solution were not used due to safety concerns. The results in the previous section showed that diesel fuel had a breakup process similar to water under the given test conditions. For a typical aftertreatment urea solution, the volume concentration of water was higher than 65%. So water was a reasonable substitute fluid in the spray test.

Before running the spray test, the injector was tested under static conditions to identify the injector opening delay and to see the original spray pattern. The images of the spray at static conditions were taken by a Canon EOS REBEL T5i DSLR camera with a high

speed LED illumination system. As shown in Figure 4-9, the first liquid droplets were detected at about 1.3ms after the injection command, which meant that the injector opening delay was about 1.3ms.

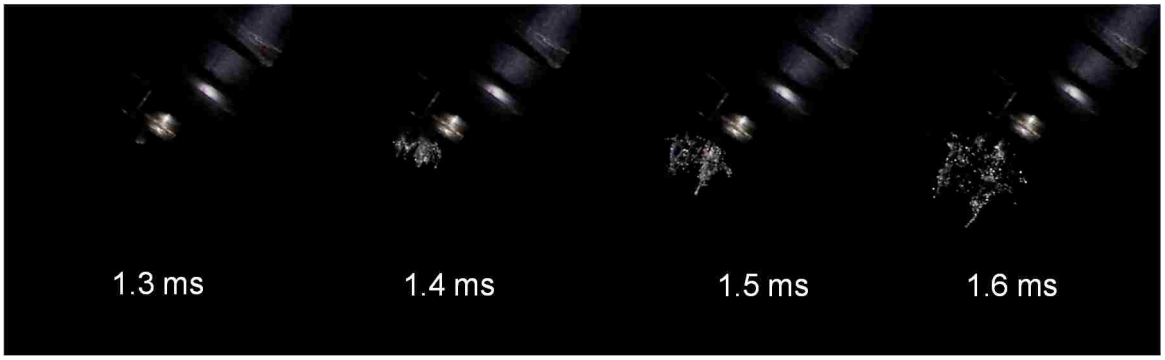

Figure 4-9. Determination of the injector opening delay

The time for the shock front moving from transducer 1 to the end of the tube was about 2 ms. In this case, the spray would not have been fully developed if the same trigger signal from transducer 1 would have been used to control the injection. In order to allow the spray to be fully developed when the shock front arrived, the injector was opened approximately 5 ms before the trigger signal.

The spray development at quiescent condition is shown in Figure 4-10. 4 ms after the injection command, the spray was fully developed and stabilized. Two liquid streams came out of the injector nozzle. The angle between the two streams was about 26°. It can be seen from the images that the water spray was not fully atomized under the low injection pressure (4 bar). The atomization was reasonable near the tip of the spray, however, there were many large droplets and unbroken water streams, especially near the nozzle.

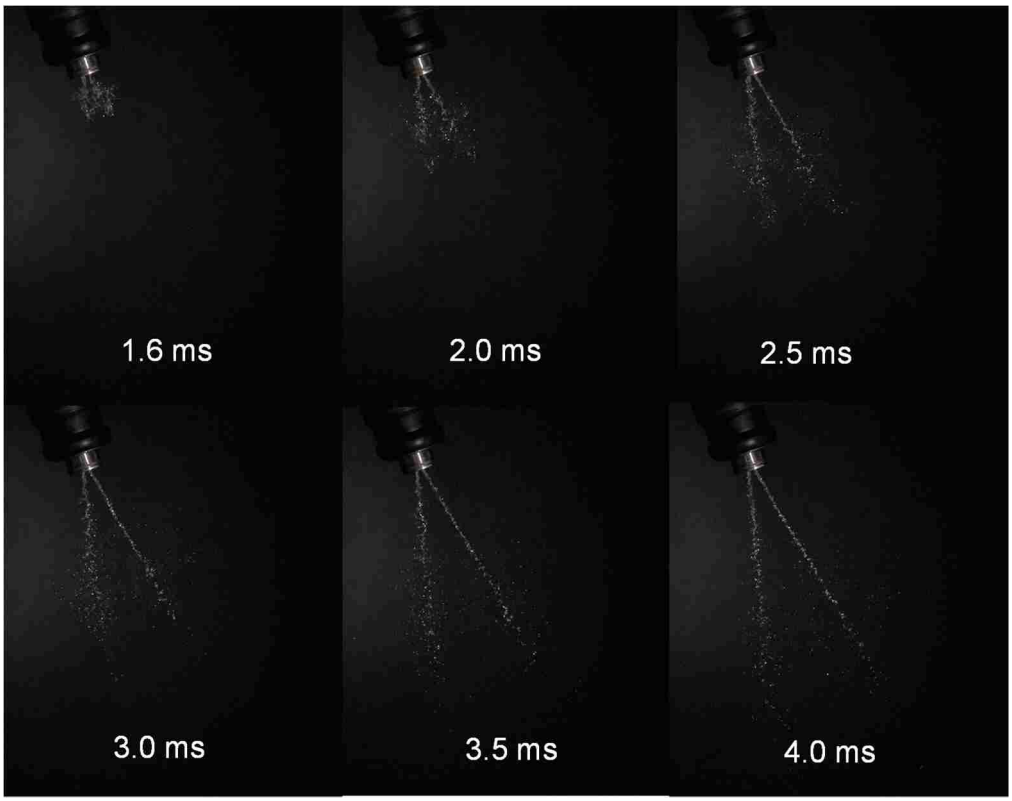

Figure 4-10. Spray development under quiescent condition

The process of spray breakup under high speed gas flow is shown in Figure 4-11. The pressure ratio of the driver and the driven sections in this test was about 4.1 which could equivalently create a gas velocity as high as 160 m/s. The time zero here was from the trigger signal of the first pressure transducer. At 2 ms, the spray was unchanged. At 2.1 ms, the first water stream was hit by the gas flow. The droplet broke up into a mist as shown by the large white area. The mist continued to expand in the next frame, where the second water stream started to change. Then, in the following 2 ms, the gas flow continuously broke the water stream and blew away the mist. Due to the high speed cross flow, the spray could not penetrate the complete length. So, very little liquid was observed in the lower part of the photos. When the air flow velocity gradually decreased, the spray went back to the original condition at approximately 12 ms after the trigger.

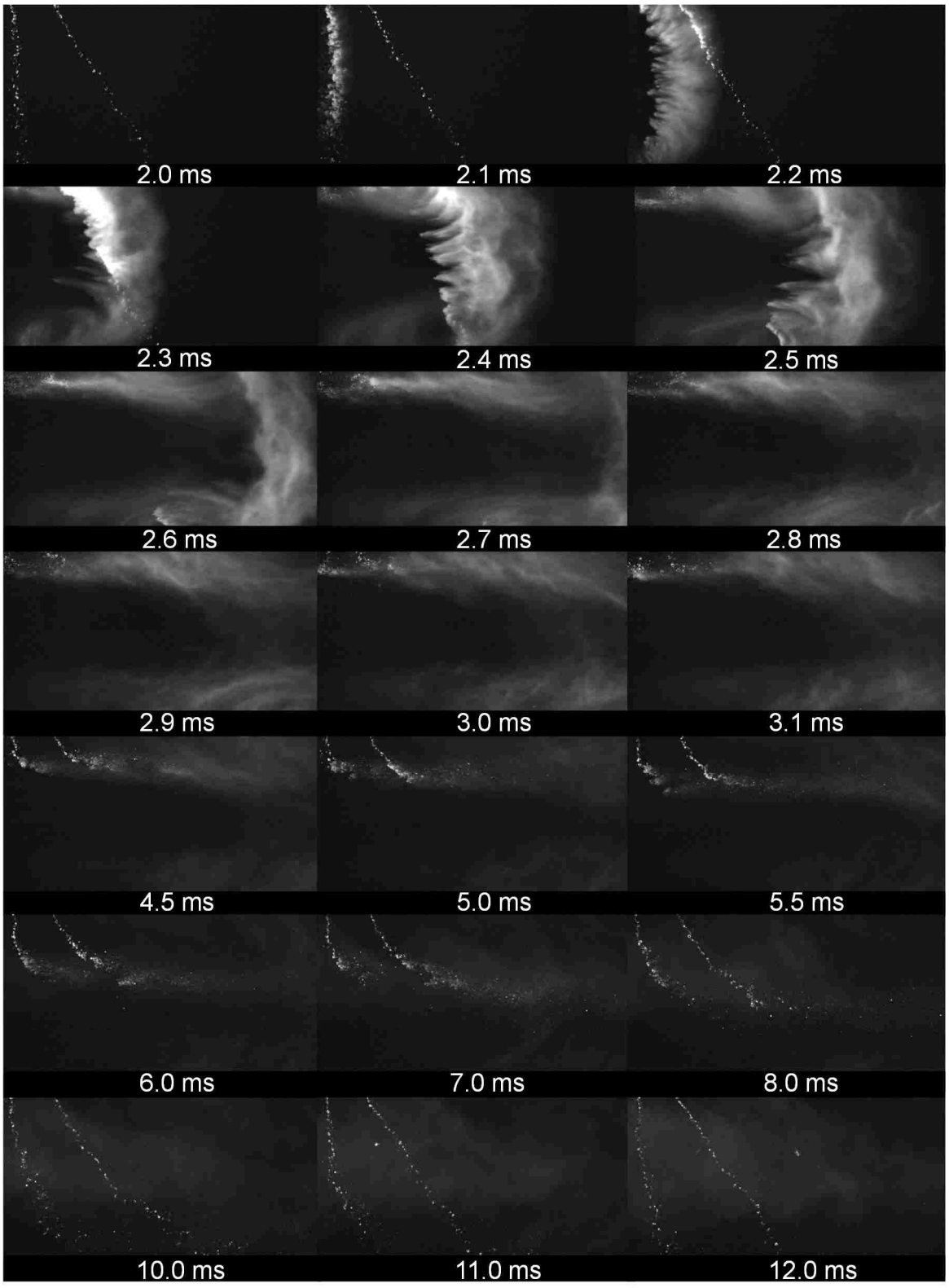

Figure 4-11. Spray distribution and atomization in the shock tube test

From the photos it was also seen that the spray distribution was not uniform under the test conditions. When the gas flow passed by, it continuously blew away the injected droplets. So, there was more water in the upper half of the photo and less in the lower half. An arrangement of the injector in this way on a production exhaust manifold may have a negative effect on catalytic converter since the lower channels may not be utilized evenly. However, the research for optimum injector arrangement was outside the scope of this research.

To quantify the effect of the shock strength on the spray droplet breakup, the gray scale spray images were converted into binary images as shown in Figure 4-12. The area of the water mist was calculated from the binary image.

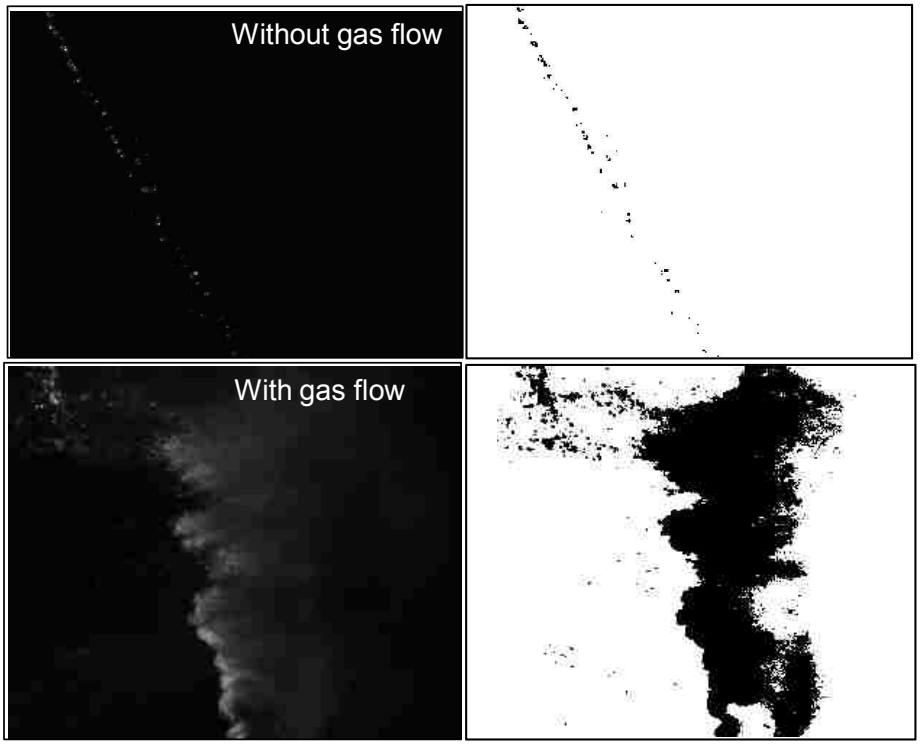

Figure 4-12. Gray scale image and corresponding binary image

Figure 4-13 shows the water mist area under different pressure ratios ranging from 1.8 to 3.7. As shown in the figure, the time of significant area increase was earlier at higher pressure ratios. This was due to the higher gas flow velocity at the higher pressure ratios. Furthermore at higher pressure ratios the area was larger and the duration of the breakup process was longer.

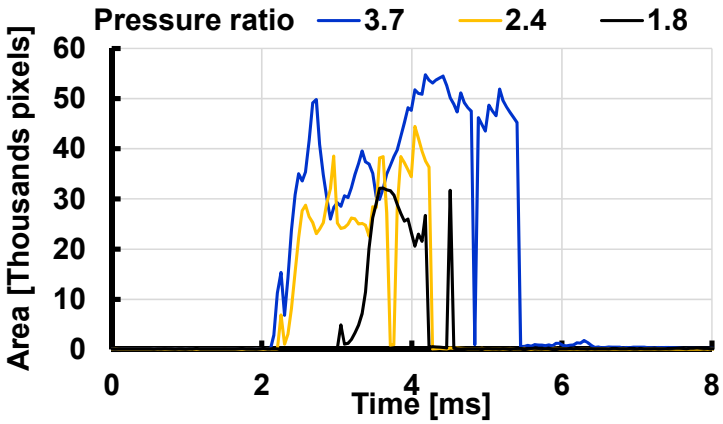

Figure 4-13. Area of water mist under different shock strength

4.4 Summary of the test results

An open end shock tube device was utilized to simulate the exhaust pressure wave effect. The burst pressure in the shock tube tests ranged from 1.8 bar to 4.5 bar, which created shock waves with peak pressures from 1.3 bar to 2.2 bar. The gas flow velocity ranged from 70 m/s to 170 m/s under the given test conditions. The velocity magnitude was similar to the exhaust flow under low to medium load conditions.

The interaction of the shock wave and droplets showed that under the test conditions, the shock front had minimum effect on the droplet breakup while the high velocity gas flow had a significant influence on the breakup process. The gas flow accelerated the breakup process. When three different kinds of fluid – diesel, ethanol, and water, were tested under simulated medium load conditions, they showed a similar trend in the breakup process. From these test results, it was predicted that the high speed gas flow was beneficial for spray atomization, which was verified by the following spray tests.

The spray images under quiescent conditions showed the presence of long, poorly atomized water columns and large droplets due to the low injection pressure. When the shock wave was initiated, the spray broke up into a mist in a very short time. This proved that under pressure wave conditions, the high speed gas flow was beneficial for aftertreatment spray atomization. From the high speed photos, it was seen that the spray was not uniformly distributed under test conditions. The injected spray did not penetrate through the whole pipe section as the cross flow continuously blew away the injected fluid.

CHAPTER 5 CONCLUSIONS AND FUTURE PERSPECTIVE

5.1 Conclusions

The pressure wave in a diesel engine exhaust system was investigated using experimental and simulation methods. The characteristics of the exhaust pressure waves, along with the velocity of the exhaust gas flow under different engine operating conditions, were evaluated.

The exhaust pressure wave and the high velocity exhaust gas flow were physically simulated with a shock tube setup. The results from the shock tube tests showed that the high velocity gas flow accompanied with the pressure wave significantly enhanced the atomization of the aftertreatment spray.

The major findings of the research are summarized as the follows:

5.1.1 Empirical results of the exhaust pressure wave

(1). Due to the increase in the in-cylinder pressure at EVO, the compression wave during the blow down process was stronger at a higher engine load. Yet, the phase of this compression wave was not affected by the load.

(2). The post injection had significant impact on the exhaust pressure wave. With the post injection, more energy was put into the expansion stroke, which substantially increased the in-cylinder pressure at EVO. The increased in-cylinder pressure greatly increased the peak exhaust pressure.

(3). EGR had minimal effect on the exhaust pressure wave under the given test conditions.

(4). Under the same in-cylinder conditions, the increase in backpressure suppressed the compression wave released from the cylinder.

(5). The exhaust pressure data measured at different locations revealed that the shape of the exhaust pressure profile was similar in a straight pipe section. However, the shape of the exhaust pressure wave was significantly changed by elbows in the piping.

(6). The phase of the pressure wave was affected by the length of the exhaust runner. However, this effect only manifested when the exhaust valves were closed. The

amplitude and the phase of the exhaust pressure wave during the valve open period were more influenced by the in-cylinder pressure than the pipe length.

5.1.2 Simulation results of the exhaust pressure wave

(1). The AVL BOOST simulation model was able to accurately simulate the exhaust pressure wave under different engine operating conditions.

(2). The velocity of the exhaust gas flow was not uniform. The fluctuation of the exhaust gas flow velocity had a trend similar to the exhaust pressure. The velocity was high during the valve open period, but was low when the exhaust valves were closed.

(3). The exhaust pressure wave and the gas flow velocity during the valve open period decreased with increase in the exhaust pipe diameter.

(4). Multiple strong compression waves were observed in the exhaust pipe of a multi-cylinder engine.

5.1.3 Empirical results of the shock tube tests

(1). The shock wave velocity and the gas flow velocity were calculated from the high speed shadowgraph images. The results showed that the wave speed and the gas flow velocity at the open end of the shock tube were not constant. A ring type flow structure was observed in the initial gas flow. The flow in the central part of the ring and the jet flow after the vortex ring were parallel to the tube axis.

(2). The high speed shadowgraph images recorded the breakup process of a single droplet placed in the path of a shock wave. The shock front had minimal impact on the droplet while the high velocity gas flow behind it significantly accelerated the droplet breakup process. Droplets of diesel, water, and ethanol were tested under similar shock wave conditions (peak shock pressure around 1.8 bar and gas flow velocity around 150 m/s). Under the given test conditions, no substantial differences in the breakup process of the three liquids were observed.

(3). The interaction of the shock wave and a low pressure spray was recorded by a high speed camera. Results showed that the high speed gas flow following the shock wave had a profound influence on the atomization and distribution of the spray. The high velocity gas flow significantly enhanced the spray atomization. However, the spray distribution was not uniform under the test conditions.

The velocity of the gas flow in the shock tube tests ranged from 70 m/s to 170 m/s which was similar to the velocity of gas flow in an engine exhaust pipe during the valve open period. The shock tube test results showed that such high speed gas flow was beneficial for the spray atomization. From these results, it was expected that the atomization of an aftertreatment spray could be improved if the fluid was injected into the exhaust pipe during the exhaust valve open period. However, since the exhaust velocity in working exhaust system would be significantly reduced by the pipe elbows and the catalytic converters, an aftertreatment injector mounted downstream on a pipe system, which had a lot of curved or diverged sections, would be less affected by the exhaust gas flow. This research also pointed out that the high speed gas flow might cause uneven distribution of the spray, which should be considered in the design of the injection system.

5.2 Future perspective

With the present research as the base, it is important to run the injection test on a real engine exhaust system with diesel fuel or urea solution. Moreover, the exhaust temperature is an important parameter which needs to be taken into consideration together with the exhaust pressure and the exhaust gas flow velocity.

REFERENCES

[1]. "Heavy-Duty Highway Compression-Ignition Engines And Urban Buses -- Exhaust Emission Standards," United States Environmental Protection Agency, [Online]. Available: http://www.epa.gov/oms/standards/heavy-duty/hdci-exhaust.htm [Accessed: 23-Aug-2015].

[2]. Twigg M. V., "Progress and Future Challenges in Controlling Automotive Exhaust Gas Emissions," Applied Catalysis B: Environmental, 70(1-4), pp. 2–15, 2007.

[3]. Zheng M., Reader G. T., Hawley J. G., "Diesel Engine Exhaust Gas Recirculation—A Review on Advanced and Novel Concepts," Energy Conversion and Management, 70(6), pp. 883–900, 2004.

[4]. Johnson T. V., "Review of Diesel Emissions and Control," International Journal of Engine Research, 10: 275–285, 2009.

[5]. Johnson T. V., "Future Perspectives on Diesel Emission Control," 2007. [Online]. Available: https://www.erc.wisc.edu/documents/symp07-Johnson.pdf. [Accessed: 22-Aug-2015]

[6]. Herreros J. M., Gill S. S., Lefort I., Tsolakis A., Millington P., Moss E., "Enhancing the Low Temperature Oxidation Performance Over a Pt and a Pt–Pd Diesel Oxidation Catalyst," Applied Catalysis B: Environmental, vol 147, pp. 835–841, 2014.

[7]. Abu-Jrai A., Tsolakis A., "The Effect of H_2 and CO on the Selective Catalytic Reduction of NOx Under Real Diesel Engine Exhaust Conditions Over Pt/Al_2O_3," International Journal of Hydrogen Energy, 32(12): 2073–2080, 2007.

[8]. Koebel M., Elsener M., Kleemann M., "Urea-SCR: a Promising Technique to Reduce NOx Emissions from Automotive Diesel Engines," Catalysis Today, 59(3-4), pp. 335–345, 2000.

[9]. Jeftic M., Zheng M., "Lean NOx Trap Supplemental Energy Savings with a Long Breathing Strategy," Proceedings of the Institution of Mechanical Engineers Part D Journal of Automotive Engineering, 227(3):400–408, 2013.

[10]. Johnson T. V., "Diesel Engine Emissions and Their Control: An Overview," Platinum Metals Review, 52, (1), pp. 23–37, 2008.

[11]. MECA, "Diesel Retrofit". [Online]. Available: http://www.meca.org/diesel-retrofit/what-is-retrofit. [Accessed: 10-Aug-2015].

[12]. Guan B., Zhan R., Lin H., Huang Z., "Review of State Of The Art Technologies of Selective Catalytic Reduction of NOx from Diesel Engine Exhaust," Applied Thermal Engineering, 66(1-2), pp. 395–414, 2014.

[13]. Dev S., "An Investigation of a Diesel Liquid Injector in a Simulated Exhaust Flow," Master's Thesis, University of Windsor, Windsor, Canada, 2013.

[14]. Needham D., Spadafora P., Schiffgens H. J., "Delphi SCR Dosing System-An Alternative Approach for Close-Coupled SCR Catalyst Systems," SIA Diesel International Conference, Rouen, 2012.

[15]. Birkhold F., Meingast U., Wassermann P., Deutschmann O., "Modeling and Simulation of the Injection of Urea-Water-Solution for Automotive SCR DeNOx-Systems," Applied Catalysis B: Environmental, 70(1-4), pp. 119–127, 2007.

[16]. Ahmed Z., "Modeling and Simulation of Urea Dosing System," Master's Thesis, ING/School of Engineering, Karlskrona, Sweden, 2013.

[17]. Oh J., Lee K., "Spray Characteristics of a Urea Solution Injector and Optimal Mixer Location to Improve Droplet Uniformity and NOx Conversion Efficiency for Selective Catalytic Reduction," Fuel, vol. 119, pp. 90–97, 2014.

[18]. Oh J., Kim K., Lee K., "Spray Characteristics of Four-Hole Injectors Used for a Hydrocarbon Lean Nitrogen Oxide Catalyst System in a Diesel Engine," Proceedings of the Institution of Mechanical Engineers Part D Journal of Automotive Engineering, 226(8), pp. 1073–1087, 2012.

[19]. BOSCH, "Denoxtronic 6-5 – Urea Dosing System for SCR systems," [Online]. Available:http://products.bosch-mobilitysolutions.com/specials/de/abgasnachbehandlung/upload_files/DS-Datenbl_DENOX_6-5-OHW_EN_2013_low.pdf. [Accessed: 22-Aug-2015]

[20]. Cummins Emission Solutions, "UL2 Liquid-Only Urea Dosing System," [Online]. Available:http://cumminsemissionsolutions.com/CES/CESContent/SiteContent/en/Binary_Asset/PDF/UL2brochure.pdf. [Accessed: 22-Aug-2015]

[21]. Commins Emission Solutions, "Urea Dosing System,"[Online]. Available: http://cumminsemissionsolutions.com/CES/CESContent/SiteContent/en/Binary_Asset/PDF/EcoFit_Urea_Dosing_System_Spec_Sheet_FINAL.pdf. [Accessed: 22-Aug-2015]

[22]. McCarthy J., Bamber D., Ambrose S., "Exhaust Tailpipe Fuel Spray Optimization and Fuel Usage Rates for Operating an Exhaust Aftertreatment System on a Heavy-Duty Diesel Engine Powered Vehicle," ILASS-Americas, 22nd Annual Conference on Liquid Atomization and Spray Systems, Cincinnati, OH, 2010.

[23]. Oh J., Kim K., Lee K., "Effects of Various Mixer Types on the Spatial Distribution of a De-NOx Reductant," Fuel, vol. 94, pp. 93–101, 2012.

[24]. Park K., Hong C.-H., Oh S., Moon S., "Numerical Prediction on the Influence of Mixer on the Performance of Urea-SCR System," International Journal of Mechanical, Aerospace, Industrial and Mechatronics Engineering, 8(5): 972–978, 2014.

[25]. Grout S., Blaisot J.-B., Pajot K., Osbat G., "Experimental Investigation on the Injection of An Urea–Water Solution in Hot Air Stream for the SCR Application: Evaporation and Spray/Wall Interaction," Fuel, vol. 106, pp. 166–177, 2013.

[26]. Montenegro G., Onorati A., Torre Della A., "The Prediction of Silencer Acoustical Performances by 1D, 1D–3D and Quasi-3D Non-Linear Approaches," Computers & Fluids, vol. 71, pp. 208–223, 2013.

[27]. Payri F., Torregrosa A. J., Payri R., “Evaluation Through Pressure and Mass Velocity Distributions of the Linear Acoustical Description of IC Engine Exhaust Systems,” Applied Acoustics, 60(4), pp. 489–504, 2000.

[28]. Bartlett H., Whalley R., “Modelling and Analysis of Variable Geometry Exhaust Gas Systems,” Applied Mathematical Modelling, 22(8), pp. 545–567, 1998.

[29]. Kim H.-D., Kweon Y.-H., Setoguchi T., “A Study of the Weak Shock Wave Propagating Through an Engine Exhaust Silencer System,” Journal of Sound and Vibration, 275(3-5), pp. 893–915, 2004.

[30]. Davies P., Harrison M. F., Collins H. J., “Acoustic Modelling of Multiple Path Silencers with Experimental Validations,” Journal of Sound and Vibration, 200(2), pp. 195–225, 1997.

[31]. Payri F., Desantes J. M., Torregrosa A. J., “Acoustic Boundary Condition for Unsteady One-Dimensional Flow Calculations,” Journal of Sound and Vibration, 188(1), pp. 85–110, 1995.

[32]. Chalet D., Mahe A., Migaud J., Hetet, J.-F., “A Frequency Modelling of the Pressure Waves in the Inlet Manifold of Internal Combustion Engine,” Applied Energy, 88(9), pp. 2988–2994, 2011.

[33]. Benson R. S., Horlock J. H., Winterbone D. E., "The Thermodynamics and Gas Dynamics of Internal Combustion Engines," Oxford University Press, 1982.

[34]. Harrison M. F., Arenas R. P., “A Hybrid Boundary for the Prediction of Intake Wave Dynamics in IC Engines,” Journal of Sound and Vibration, 270(1), pp. 111–136, 2004.

[35]. Payri F., Reyes E., Galindo J., “Analysis and Modeling of the Fluid-Dynamic Effects in Branched Exhaust Junctions of ICE,” Journal of Engeering for Gas Turbines and Power, 123(1), pp. 197–203, 2001.

[36]. Piscaglia F., Ferrari G., “A Novel 1D Approach for the Simulation of Unsteady Reacting Flows in Diesel Exhaust After-Treatment Systems,” Energy, 34(12), pp. 2051–2062, 2009.

[37]. Chalet D., Chesse P., Hetet J. F., “Boundary Conditions Modelling of One-Dimensional Gas Flows in An Internal Combustion Engine,” International Journal of Engine Research, 9(4), pp. 267–282, 2008.

[38]. Harrison M. F., Stanev P. T., “A Linear Acoustic Model for Intake Wave Dynamics in IC Engines,” Journal of Sound and Vibration, 269(1-2), pp. 361–387, 2004.

[39]. Sathyanarayana Y., Munjal M.L., “A Hybrid Approach for Aeroacoustic Analysis of the Engine Exhaust System,” Applied Acoustics, vol. 60, pp. 425–450, 2000.

[40]. Gasser I., Rybicki M., “Modelling and Simulation of Gas Dynamics in An Exhaust Pipe,” Applied Mathematical Modelling, 37(5), pp. 2747–2764, 2013.

[41]. Bodin O., “Numerical Computations of Internal Combustion Engine related Transonic and Unsteady Flows,” Licentiate thesis, KTH Mechanics, Stockholm, Sweden, 2009.

[42]. Harrison M. F., De Soto I., Rubio Unzueta P. L., "A Linear Acoustic Model for Multi-Cylinder IC Engine Intake Manifolds Including the Effects of the Intake Throttle," Journal of Sound and Vibration, 278(4-5), pp. 975–1011, 2004.

[43]. Serrano J. R., Arnau F. J., Piqueras P., Onorati A., Montenegro G., "1D Gas Dynamic Modelling of Mass Conservation in Engine Duct Systems with Thermal Contact Discontinuities," Mathematical and Computer Modelling, 49(5-6), pp. 1078–1088, 2009.

[44]. You G., Xu C., Xu J., Zhu M., Wang Z., "Application of Space-Time Conservation Element and Solution Element Method in Intake and Exhaust Flows of High Power Density Diesel Engine," Defense Technology, 9(3), pp. 171–175, 2013.

[45]. Stockar S., Canova M., Guezennec Y., Torre A. D., Montenegro G., Onorati, A., "Modeling Wave Action Effects in Internal Combustion Engine Air Path Systems: Comparison of Numerical and System Dynamics Approaches," International Journal of Engine Research., 14(4), pp. 391–408, 2013.

[46]. Chalet D., Mahé A., Hétet J.-F., Migaud J., "A New Modeling Approach of Pressure Waves at the Inlet of Internal Combustion Engines," Journal of Thermal Science, 20(2), pp. 181–188, 2011.

[47]. Harrison M.F., Stanev P.T., "A Linear Acoustic Model for Intake Wave Dynamics in IC Engines," Journal of Sound and Vibration, 269(1-2), pp. 361–387, 2004.

[48]. Mezher H., Chalet D., Migaud J., Chesse P., "Frequency Based Approach for Simulating Pressure Waves at the Inlet of Internal Combustion Engines Using a Parameterized Model," Applied Energy, vol. 106, pp. 275–286, 2013.

[49]. Sekine N., Matsumura S., Aoki K., Takayama K., "Generation and Propagation of Shock Waves in the Exhaust Pipe of a 4 Cycle Automobile Engine," AIP Conference Proceedings., vol. 208, pp. 671–677, 1990.

[50]. Harrison M. F., Stanev P. T., "Measuring Wave Dynamics in IC Engine Intake Systems," Journal of Sound and Vibration, 269(1), pp. 389–408, 2004.

[51]. Liu Z., "Pulsating Flow Misdistribution in Automotive Exhaust Catalysts - Numerical Modelling and Experimental Correlation," Ph.D. Thesis, Coventry University, Coventry, United Kingdom, 2003.

[52]. Joseph D. D., Belanger J., Beavers G. S., "Breakup of a Liquid Drop Suddenly Exposed to a High-Speed Airstream," International Journal of Multiphase Flow, 25(6), pp. 1263–1303, 1999.

[53]. Engel O. G., "Fragmentation of Waterdrops in the Zone Behind an Air Shock," Journal of Research of National Bureau of Standards, 60(3), pp. 245–280, 1958.

[54]. Hsiang L.-P., Faeth G.M., "Drop Deformation and Breakup Due To Shock Wave and Steady Disturbances," International Journal of Multiphase Flow, 21(4), pp. 545–560, 1995.

[55]. Kyriakides N., Chryssakis C., Kaiktsis L., "Influence of Heavy Fuel Properties on Spray Atomization for Marine Diesel Engine Applications," SAE Technical Paper, 2008-01-1858, 2008.

[56]. Chryssakis C., Assanis D. N., “A Unified Fuel Spray Breakup Model for Internal Combustion Engine Applications,” Atomation and Sprays, 18(5), pp. 1–52, 2008.

[57]. Kistler Group, 2013, “Piezoresistive Absolute Pressure Sensors,” [Online]. Available: www.kistler.com/?type=669&fid=18001&model=document.[Accessed:23-Aug-2015].

[58]. Kistler Group, 2013, “New Opportunities for Gas Exchange Analysis Using Piezoresistive High-Temperature Absolute Pressure Sensors, ” [Online]. Available: https://www.kistler.com/fileadmin/files/divisions/automotive-research-test/engines-research-and-development/pruefstand-indizieren/920-366e-10.08.pdf.[Accessed: 23-Aug-2015]

[59]. Kitler Group, 2013, “Amplifier for Measuring of Pressure and Temperature,” [Online]. Available: www.kistler.com/?type=669&fid=3475.[Accessed: 23-Aug-2015]

[60]. AVL, “BOOST Theory,” 2013.

[61]. AVL, “BOOST Users Guide,” 2013.

[62]. Henshall B. D., “On some aspects of the use of shock tubes in aerodynamic research,” London: Her Majesty's Stationary Office, 1957.

[63]. Galindo J., Tiseira A., Fajardo P., Navarro R., “Analysis of the Influence of Different Real Flow Effects on Computational Fluid Dynamics Boundary Conditions Based on the Method of Characteristics,” Mathematical and Computer Modelling, 57(7-8), pp. 1957–1964, 2013.

[64]. Liang S.-M., Tsai S.-J., Wang S.-F., “An Effective Approach for Calculation of Exhaust Pipe Flows,” Journal of Mechanics, 25(02), pp. 177–188, 2009.

[65]. Chehroudi B., Schuh D., “Intake-Port Flow Behavior in a Motored and Fired Two-Stroke Research Engine,” Experimental Thermal and Fluid Science, 10(1), pp. 86–100, 1995.

[66]. Sato N., Iwamoto J., “Visualization of Flow Field of High Speed Pulsating Jet by Mach-Zehnder Interferometry,” 10th International Conference on Fluid Control, Measurements, and Visualization, Moscow, Russia, 2009.

[67]. Estruch D., Lawson N. J., MacManus D. G., Garry K. P., Stollery J. L., “Measurement of Shock Wave Unsteadiness Using a High-Speed Schlieren System and Digital Image Processing,” Review of Science Instruments, 2008.

[68]. Arakeri J. H., Das D., Krothapalli A., Lourenco L., “Vortex Ring Formation at the Open End of a Shock Tube: A Particle Image Velocimetry Study,” Physics of Fluids, 16(4), pp. 1008–1019, 2004.

[69]. Wüthrich B., Lee Y. J., “Simulation and Validation of Compressible Flow in Nozzle Geometries and Validation of OpenFOAM for This Application,” Master's Thesis, Institute of Fluid Dynamics, ETH Zürich, Zürich, Switzerland, 2007.

APPENDIX A: SIMULATION MODELS OF ENGINE SYSTEM COMPONENTS

(1) Cylinder [60]

$$\frac{d(m_c \cdot U)}{d\alpha} = -p_c \cdot \frac{dV_c}{d\alpha} + \frac{dQ_F}{d\alpha} - \sum \frac{dQ_w}{d\alpha} - h_{BB} \cdot \frac{dm_{BB}}{d\alpha} + \sum \frac{dm_i}{d\alpha} \cdot h_i - \sum \frac{dm_{out}}{d\alpha} \cdot h_{out} - q_{ev} \cdot f \cdot \frac{dm_{ev}}{dt} \quad \text{A-1}$$

The variation of the mass in the cylinder can be calculated from the sum of the in-flowing and out-flowing masses:

$$\frac{dm_c}{d\alpha} = \sum \frac{dm_i}{d\alpha} - \sum \frac{dm_{out}}{d\alpha} - \frac{dm_{BB}}{d\alpha} + \frac{dm_{ev}}{dt} \quad \text{A-2}$$

The equations are closed by:

$$p_c = \frac{1}{V_c} \cdot m_c \cdot R_o \cdot T_c \quad \text{A-3}$$

m_c	mass in the cylinder	U	specific internal energy
α	crank angle	p_c	in-cylinder pressure
V_c	in-cylinder volume	Q_F	fuel energy input
Q_w	wall heat transfer	h_{BB}	enthalpy of blow-by
m_{BB}	blow-by mass	m_i	mass flowing into the cylinder
f	fraction of evaporation heat from the cylinder charge	h_{out}	enthalpy of the mass leaving the cylinder
m_{out}	mass leaving the cylinder	q_{ev}	evaporation heat of the fuel
h_i	enthalpy of the in-flowing mass	m_{ev}	evaporating fuel
T_c	in-cylinder temperature	R_o	gas constant

(2) Flow through intake and exhaust valves [60]

The mass flow rates at the intake and exhaust ports are calculated from the equations for isentropic orifice flow:

$$\frac{dm}{dt} = A_{eff} \cdot p_{o1} \cdot \sqrt{\frac{2}{R_o \cdot T_{o1}}} \cdot \varphi \quad \text{A-4}$$

for subsonic flow:

$$\varphi = \sqrt{\frac{k}{k-1} \cdot \left[\left(\frac{p_{o2}}{p_{o1}}\right)^{\frac{2}{k}} - \left(\frac{p_{o2}}{p_{o1}}\right)^{\frac{k+1}{k}} \right]}$$

and for sonic flow:

$$\varphi = \varphi_{max} = \left(\frac{2}{k+1}\right)^{\frac{1}{k-1}} \cdot \sqrt{\frac{k}{k+1}}$$

The flow area can be calculated from:

$$A_{eff} = \mu\sigma \cdot \frac{d_{vi}^2 \cdot \pi}{4}$$

m	mass of gas	A_{eff}	effective flow area
p_{o1}	upstream stagnation pressure	T_{o1}	upstream stagnation temperature
R_o	gas constant	p_{o2}	downstream static pressure
k	ratio of specific heats	d_{vi}	inner valve seat diameter
$\mu\sigma$	flow coefficient of the port	t	time

Here p_{o1} and p_{o2} represent upstream and downstream conditions respectively. For the intake valve, p_{o1} represents the condition in the intake port while in the exhaust system where gas flows from cylinder to the exhaust pipe, p_{o1} represents the condition inside the cylinder. Depending on the ratio between p_{o1} and p_{o2}, the flow at the throat area can be subsonic or sonic. The sonic flow is also called chocked flow. The flow is under choked condition when the pressure ratio:

$$\frac{p_{o1}}{p_{o2}} \geq \left(\frac{2}{k+1}\right)^{\frac{-k}{k-1}}$$

The flow coefficient $\mu\sigma$ represents the ratio between the actual measured mass flow rate at a certain pressure difference, and the theoretical isentropic mass flow rate for the same boundary conditions. The flow coefficient is related to the cross section area of the attached pipe. It varies with valve lift and is usually determined on a steady-state flow test rig. Since it was not possible to conduct on the existing setup, the coefficient was tuned

by trial and error. The coefficient was determined by matching the simulation results to the empirical results.

(3) Pipe [60]

The conservation equation of one dimensional pipe flow is given by:

$$\frac{\partial \varphi}{\partial t} + \frac{\partial F(\varphi)}{\partial x} = B(\varphi) \tag{A-5}$$

Where:

$$\varphi = \begin{pmatrix} \rho \\ \rho \cdot u \\ \rho \cdot c_v \cdot T + \frac{1}{2} \cdot \rho \cdot u^2 \\ \rho \cdot w_j \end{pmatrix} \tag{A-6}$$

$$F = \begin{pmatrix} \rho \cdot u \\ \rho \cdot u^2 + p \\ u \cdot (E + p) \\ \rho \cdot u \cdot w_j \end{pmatrix} \tag{A-7}$$

and

$$E = \rho \cdot c_v \cdot T + \frac{1}{2} \cdot \rho \cdot u^2$$

The source term on the right hand side comprises of two different source terms:

$$B(\varphi) = \frac{1}{A} \cdot \frac{dA}{dx} \cdot F + B_R(\varphi) \tag{A-8}$$

The first term is related the axial changes in the pipe cross section and the second term $B_R(\varphi)$ takes into account homogeneous chemical reactions, heat and mass transfer terms between the gas and solid phase and friction sources, the more detailed information about the source terms can be acquired in [60].

ρ	density	u	velocity
c_v	constant volume heat capacity of the gas mixture	T	temperature
x	distance	A	sectional area
w_j	mass fraction of different gas		

The shock capturing schemes used in BOOST do not provide the information of pressure wave travel as they solve the set of partial differential equations directly. Therefore, the

wave fluctuation from superimposition of forward and backward running waves must be constructed from the solution afterwards. The procedure is similar to the one introduced in the characteristic method [33].

(4) Plenum [60]

The conservation equation of plenum is similar to the process of cylinder, except there is no fuel energy input, no blow by loss and no fuel evaporation. Instead the enthalpy source due to chemical reaction was added in the conservation equations.

$$\frac{d(m_{pl} \cdot U)}{d\alpha} = -p_{pl} \cdot \frac{dV_{pl}}{d\alpha} - \sum \frac{dQ_w}{d\alpha} + \sum \frac{dm_i}{d\alpha} \cdot h_i - \sum \frac{dm_{out}}{d\alpha} \cdot h_{out} - \cdot \frac{dQ_{reac}}{dt} \quad \text{A-9}$$

m_{pl}	mass of gas in the plenum	U	specific internal energy
p_{pl}	plenum pressure	V_{pl}	plenum volume
h_i	enthalpy of the in-flowing mass	α	crank angle
Q_{reac}	energy due to chemical reactions	m_{out}	mass flowing out of the plenum
Q_w	wall heat loss	m_i	mass flowing into the plenum
t	time	h_{out}	enthalpy of the out-flowing mass

(5) Elbows [60]

Pipe elbows are common components in engine system. In a one dimension gas dynamic simulation, the effect of pipe elbows is treated as a friction loss coefficient ζ:

$$\Delta p = \zeta \frac{\rho u^2}{2} \quad \text{A-10}$$

This loss coefficient is a function of the bend angle and the ratio between the bend radiuses and the pipe diameter.

(6) Junctions [33]

For the junction boundary condition, the pressure and the gas density at the pipe joint are considered to be the same. Take the junction with three pipe branches as an example:

$$p_1 = p_2 = p_3 \quad \text{A-11}$$

$$\rho_1 u_1 A_1 = \rho_2 u_2 A_2 = \rho_3 u_3 A_3 \quad \text{A-12}$$

$$\rho_1 = \rho_2 = \rho_3 \quad \text{A-13}$$

Where p is pressure, ρ is density, u is velocity and A is the sectional area of each pipe.

APPENDIX B: SHOCK TUBE THEORY

There are four distinct regions in a shock tube in the case of shock wave as indicated in Figure B-1.

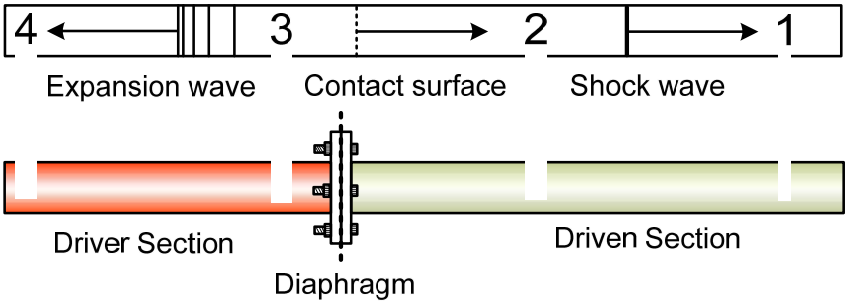

Figure B-1. Shock tube schematic

Firstly, the conservation of mass, momentum, and energy between regions 1 and 2 can be written as [69]:

$$\rho_1 u_1 = \rho_2 u_2 \tag{B-5}$$

$$p_1 + \rho_1 u_1^2 = p_2 + \rho_2 u_2^2 \tag{B-6}$$

$$h_1 + \frac{1}{2}u_1^2 = h_2 + \frac{1}{2}u_2^2 \tag{B-7}$$

where ρ is density, u is velocity, p is pressure and h is the enthalpy. The subscripts indicate different regions as shown in Figure B-1. If the shock wave speed is assumed as W, the contact gas flow velocity is U_p, then with reference to the wave, the gas velocity ahead of the shock wave is W while the gas velocity behind the wave is W-U_p. Thus, after rearrangement, equations (B-1) to (B-3) can be written as:

$$\rho_1 W = \rho_2 (W - U_p) \tag{B-8}$$

$$p_1 + \rho_1 W^2 = p_2 + \rho_2 (W - U_p)^2 \tag{B-9}$$

$$h_1 + \frac{1}{2}W^2 = h_2 + \frac{1}{2}(W - U_p)^2 \tag{B-10}$$

Since $h = e + pv = e + {}^{p}/_{\rho}$, where e is internal energy and v is the specific volume. combined with equations (B-4) and (B-5), equation(B-6) can be rewritten as:

$$e_2 - e_1 = \frac{1}{2}(p_1 + p_2) * (v_1 - v_2) \tag{B-11}$$

Which is the Rankine–Hugoniot equation. With the relation $e = C_v T = R_0 T/(k-1)$ and $v = R_0 T/p$, where C_v is the specific heat capacity at constant volume, T is temperature,

R_0 is the specific gas constant and k is the specific heat capacity ratio. By substituting the terms in equation (B-7), the temperature ratio between regions 1 and 2 can be represented by:

$$\frac{T_2}{T_1} = \frac{p_2}{p_1}\left(\frac{\frac{k+1}{k-1}+\frac{p_2}{p_1}}{1+\frac{k+1}{k-1}*\frac{p_2}{p_1}}\right) \quad \text{B-12}$$

Similarly, the density ratio can also be defined as:

$$\frac{\rho_2}{\rho_1} = \frac{1+\frac{k+1}{k-1}*\frac{p_2}{p_1}}{\frac{k+1}{k-1}+\frac{p_2}{p_1}} \quad \text{B-13}$$

The shock Mach number is defined as:

$$Ma = \frac{W}{a_1} \quad \text{B-14}$$

Where a_1 is the speed of sound in region 1.From equation (B-8) and (B-9), as well as the perfect gas relation, the relationship between pressure ratio and Mach number can be derived as:

$$\frac{p_2}{p_1} = 1+\frac{2k}{k+1}(Ma^2-1) \quad \text{B-15}$$

So,

$$Ma = \sqrt{\frac{k+1}{2k}\left(\frac{p_2}{p_1}-1\right)+1}$$

Then the wave speed can be calculated:

$$W = a_1\sqrt{\frac{k+1}{2k}\left(\frac{p_2}{p_1}-1\right)+1} \quad \text{B-16}$$

Combined with equation (B-4), the gas flow velocity is:

$$U_p = W\left(1-\frac{\rho_1}{\rho_2}\right) = \frac{a_1}{k}\left(\frac{p_2}{p_1}-1\right)\left(\frac{\frac{2k}{k+1}}{\frac{p_2}{p_1}+\frac{k-1}{k+1}}\right)^{\frac{1}{2}} \quad \text{B-17}$$

As for regions 3 and 4, since the direction of the expansion wave is opposite to the gas flow direction, the local velocity is *u-a*. The flow is assumed to be isentropic. The relation derived by the characteristic method regarding the expansion wave is [33]:

$$\frac{da}{du} = \frac{k-1}{2} \tag{B-18}$$

$$Or \quad u - \frac{2a}{k-1} = const \tag{B-19}$$

As in region 4, the gas is initially at rest and the flow velocity $u_4 = 0$, so

$$u_4 - \frac{2a_4}{k-1} = \frac{2a_4}{k-1} = const$$

related to $a = \sqrt{kR_0T}$ and the isentropic equation, the pressure, density and temperature in region 4 can be obtained:

$$\frac{T}{T_4} = \left(1 - \frac{k-1}{2}(u/a_4)\right)^2 \tag{B-20}$$

$$\frac{p}{p_4} = \left(1 - \frac{k-1}{2}(u/a_4)\right)^{\frac{2k}{k-1}} \tag{B-21}$$

$$\frac{\rho}{\rho_4} = \left(1 - \frac{k-1}{2}(u/a_4)\right)^{\frac{2}{k-1}} \tag{B-22}$$

Also the pressure and gas flow velocity in regions 2 and 3 are the same, which is $u_2 = u_3 = u_p$ and $p_2 = p_3$. Combined with the equations derived earlier, the relationship between the pressure change across the shock wave and the initial pressure ratio of the driver and driven sections can be obtained by:

$$\frac{p_4}{p_1} = \left(\frac{p_2}{p_1}\right)\left(1 - \frac{(k_4-1)(a_1/a_4)(p_2/p_1-1)}{\sqrt{2k_1\left(2k_1 + (k_1+1)(p_2/p_1-1)\right)}}\right)^{\frac{-2k_4}{k_4-1}} \tag{B-23}$$

VITA AUCTORIS

NAME:	Zhenyi Yang
PLACE OF BIRTH:	Hubei, China
YEAR OF BIRTH:	1986
EDUCATION:	China Agricultural University Master of Applied Science Beijing, China, 2010
	China Agricultural University Bachelor of Engineering Beijing, China, 2008

LIST OF PUBLICATIONS

Papers in Refereed Conference Proceedings:

1. Divekar, P., **Yang, Z.,** Ting, D., Chen, X., Zheng, M., and Tjong, J., "Efficiency and Emission Trade-Off in Diesel-Ethanol Low Temperature Combustion Cycles," SAE Technical Paper 2015-01-0845, doi:10.4271/2015-01-0845, 2015.

Papers in Non-refereed Conference Proceedings:

1. Yang, Z., Aversa, C., Ives, M., Divekar, P., Ting, D., Zheng, M., "Hydrogen as a by-product of diesel engine low temperature combustion," Natural Gas and Hydrogen Storage 2015 Symposium & Industry Connector Event, Windsor, Ontario, Canada, June 24-25, 2015.

2. Jeftic, M., **Yang, Z.,** Ting, D., Zheng, M., "An investigation of the optimal post injection timing for diesel exhaust after-treatment," The Combustion Institute Canadian Section, 2014 Spring Technical Meeting, Windsor, Ontario, Canada, May 12-15, 2014.

3. Bryden, G., Divekar, P., **Yang, Z.,** Zheng, M., "Ignition delay, heat release profile, and emission correlation in diesel low temperature combustion," The Combustion Institute Canadian Section, 2015 Spring Technical Meeting, Saskatoon, Saskatchewan, Canada, May 11-14, 2015.

Poster Presentations:

1. Divekar, P., Han, X., **Yang, Z**., NSERC CREATE Program in Clean Combustion Engines Graduate Summer School. Theme: Bio-fuels for Advanced Engine Technologies. Toronto, Ontario, Canada, 2014.

2. **Yang, Z**., Tan. Q., Divekar, P., Bryden,G., Auto21 Annual conference. Theme: Integrated HCCI Combustion and Emission Control for Future Vehicles. Ottawa, Ontario, Canada, 2015.

3. Divekar, P., Dev. S., Tan. Q., **Yang, Z**., NSERC CREATE Program in Clean Combustion Engines Graduate Summer School. Theme: Exhaust Gas Recirculation for Ultra-low NOx Emissions. Windsor, Ontario, Canada, 2015.